



**HAL**  
open science

# Attitude estimation of an artillery shell in free-flight from accelerometers and magnetometers

Aurélien Fiot

► **To cite this version:**

Aurélien Fiot. Attitude estimation of an artillery shell in free-flight from accelerometers and magnetometers. Automatic Control Engineering. Université Paris sciences et lettres, 2020. English. NNT : 2020UPSLM039 . tel-03097354

**HAL Id: tel-03097354**

**<https://pastel.hal.science/tel-03097354>**

Submitted on 5 Jan 2021

**HAL** is a multi-disciplinary open access archive for the deposit and dissemination of scientific research documents, whether they are published or not. The documents may come from teaching and research institutions in France or abroad, or from public or private research centers.

L'archive ouverte pluridisciplinaire **HAL**, est destinée au dépôt et à la diffusion de documents scientifiques de niveau recherche, publiés ou non, émanant des établissements d'enseignement et de recherche français ou étrangers, des laboratoires publics ou privés.



**THÈSE DE DOCTORAT**

**DE L'UNIVERSITÉ PSL**

Préparée à MINES ParisTech

**Estimation en vol de l'attitude de projectiles à l'aide  
d'accéléromètres et de magnétomètres**

**Attitude estimation of an artillery shell in free-flight from  
accelerometers and magnetometers**

Soutenue par

**Aurélien FIOT**

Le 30 Octobre 2020

École doctorale n°621

**Ingénierie des Systèmes,  
Matériaux, Mécanique, En-  
ergétique**

Spécialité

**Mathématique et Automa-  
tique**

Composition du jury :

Pascal MORIN

Pr., Sorbonne Université, ISIR

*Rapporteur, prési-  
dent du jury*

Hélène PIET-LAHANIER

Directrice scientifique adjointe, ONERA

*Rapporteur*

Tarek HAMEL

Pr., Université de Nice, I3S

*Examineur*

Sihem TEBBANI

Pr., CentraleSupélec, LSS

*Examineur*

Sébastien CHANGEY

Dr., Institut Saint-Louis

*Examineur*

Nicolas PETIT

Pr., MINES ParisTech

*Directeur de thèse*



# Contents

<b>1</b>	<b>Context and problem statement</b>	<b>13</b>
1.1	Introduction . . . . .	13
1.2	The concept of smart artillery shells . . . . .	16
1.3	Attitude estimation for smart shells applications . . . . .	18
1.4	Outline of the proposed solution . . . . .	19
1.5	Organization of the thesis . . . . .	21
<b>2</b>	<b>Mathematical formulation, notations, flight dynamics and instrumentation</b>	<b>25</b>
2.1	Reference frames and Six-Degrees-of-Freedom description . . . . .	25
2.2	Environment model . . . . .	27
2.3	Projectile model: dimensional parameters and aerodynamic coefficients . . . . .	29
2.4	Flight dynamics . . . . .	30
2.4.1	Translational dynamics . . . . .	33
2.4.2	Rotational dynamics . . . . .	34
2.5	Onboard Sensors . . . . .	36
2.5.1	Description of the embedded system . . . . .	36
2.5.2	Detrimental effects and mitigation means . . . . .	38
	Eddy currents . . . . .	38
	Misalignment . . . . .	39
	Fictitious forces . . . . .	40
2.6	Preliminary estimation of the angular velocity around main axis . . . . .	43

2.7	Shooting range and external instrumentation . . . . .	44
2.8	Testcases considered in the thesis . . . . .	44
<b>3</b>	<b>Frequency analysis of the epicyclic rotational dynamics</b>	<b>51</b>
3.1	Problem statement . . . . .	51
3.2	Frequency content of the embedded inertial measurements . .	52
3.3	Instantaneous frequency detection: measuring varying fre- quencies . . . . .	53
3.3.1	Definition of the frequency of interest . . . . .	53
3.3.2	Envelope filter and FFT . . . . .	56
3.3.3	Detecting peaks in the autocorrelation function . . . .	57
3.3.4	Frequency detection using super-resolution . . . . .	58
3.3.5	Filtering the estimates . . . . .	59
3.4	Design of an observer for the velocity from frequency mea- surements . . . . .	61
3.4.1	System dynamics and output map . . . . .	61
3.4.2	Observer design . . . . .	63
3.4.3	Convergence analysis . . . . .	64
3.5	Illustrative results . . . . .	66
3.5.1	Reference velocity . . . . .	66
3.5.2	Results . . . . .	67
3.6	Conclusion . . . . .	67
<b>4</b>	<b>Slope estimation through an analysis of the velocity dynam- ics</b>	<b>71</b>
4.1	Slope angle observer . . . . .	71
4.1.1	Observer design . . . . .	74
4.1.2	Simulation results . . . . .	75
4.1.3	Experimental results . . . . .	76
4.2	From the slope angle to the pitch angle . . . . .	77
4.3	Conclusion . . . . .	78
<b>5</b>	<b>An attitude observer from 3-axis Magnetometer and pitch angle</b>	<b>83</b>

5.1	A quaternion representation of the problem . . . . .	83
5.2	Single-direction attitude complementary filter . . . . .	84
5.2.1	Recalls on attitude complementary filter . . . . .	84
5.2.2	Partial convergence using a single direction . . . . .	85
5.3	Complementarity of pitch angle information and magnetic vector measurement . . . . .	87
5.3.1	Reduction of the convergence set . . . . .	87
	Attitude solutions . . . . .	87
	Separation of the solutions . . . . .	89
5.3.2	A continuity property . . . . .	90
5.4	Proposed observer . . . . .	91
5.5	Assumptions on the flight . . . . .	91
5.6	Main result . . . . .	94
5.7	Proof of convergence . . . . .	94
5.7.1	Asymptotic behavior . . . . .	94
5.7.2	First case: Assumption 3 holds . . . . .	98
5.7.3	Second case: Assumption 3 does not hold . . . . .	102
5.7.4	Conclusion of the proof . . . . .	102
5.8	Practical use of the main result . . . . .	103
5.8.1	Observed asymptotic behavior . . . . .	103
5.8.2	Interpretation of the solution $q_{\#}$ . . . . .	103
5.8.3	Practical initialization to ensure convergence towards actual attitude . . . . .	104
5.9	Estimation results . . . . .	105
5.9.1	Simulation results . . . . .	106
	On 155 mm shell . . . . .	106
	On Basic Finner . . . . .	107
5.9.2	Experimental results . . . . .	108
<b>6</b>	<b>Experimental results of the proposed attitude observer us- ing only on-board sensors</b>	<b>117</b>
6.1	Multirate Kalman filtering of frequency estimators . . . . .	117

6.2	Debiasing of the frequency estimate . . . . .	118
6.3	Smoothing under convexity constraints . . . . .	119
6.4	Slope and pitch estimation experimental results . . . . .	119
6.5	Attitude observer results . . . . .	120
<b>7</b>	<b>Conclusion and perspectives</b>	<b>129</b>
<b>Appendix A Supplementary material</b>		<b>133</b>
A.1	Transition matrices . . . . .	133
A.2	Alternative angles . . . . .	134
A.3	Approximation on the shell velocity . . . . .	135
A.4	Material for Chapter 3 . . . . .	137
A.5	Calculations leading to $q_{\#}$ expression in Chapter 5 . . . . .	137
A.6	An equivalence property for Chapter 5 . . . . .	139
<b>Appendix B Various useful estimation methods</b>		<b>141</b>
B.1	Complex argument method for single-axis rotation rate estimation . . . . .	141
B.2	Linear constrained estimation . . . . .	142
B.3	Background on MUSIC frequency estimation algorithm . . . . .	144

# Abstract

The thesis addresses the estimation of the attitude of an artillery shell in free flight, during the flight phase called exterior ballistics. Attitude estimation is an essential step for the development of « smart-shells » a.k.a. « guided-ammunition » which are capable of achieving various guidance tasks such as in-flight re-targeting and optimization of range. The method developed here uses strapdown accelerometers and magnetometers only. In particular, it does not use any rate gyro, a pricey component that is too fragile to survive the stress of gunshot when it is not subjected to import restrictions. For attitude determination, we circumvent the intrinsic inability of accelerometers to provide direction information in free flight, by employing them not to measure the direction of gravity but to estimate the velocity w.r.t. the air. This is achieved through a frequency detection method applied to the pitching and yawing rotational dynamics generated by aerodynamics moments. In turn, the variation of the velocity gives us an orientation information that complements the direction given by the 3-axis Magnetometer. The two information are treated by an attitude observer adapted from the well-known complementary filter. This adaptation requires special care and an analysis of the convergence of the resulting observer is provided. The applicability of the method is shown on simulations and real-flight experiments.



# Résumé

Cette thèse présente une méthode pour estimer l'attitude d'un projectile en vol à partir de mesures de directions. L'estimation d'attitude est une étape essentielle pour le développement de « munitions intelligentes », rendant possible le changement de cible en vol et l'optimisation de la portée. La méthode que nous proposons repose exclusivement sur un accéléromètre et un magnétomètre embarqués. En particulier, elle ne requiert pas de gyroscope, capteur coûteux et trop fragile pour survivre aux conditions de tir, quand il n'est pas soumis à des restrictions d'importation. Pour la détermination de l'attitude du projectile, nous contournons l'incapacité des accéléromètres à donner une mesure de direction de la gravité en vol ballistique, en les utilisant pour estimer la vitesse du projectile par rapport à l'air. Ceci est réalisé grâce à une méthode de détection de fréquence appliquée aux oscillations de précession et de nutation du projectile induites par les moments aérodynamiques qu'il subit. Par la suite, les variations de la vitesse du projectile nous donnent une information d'orientation partielle qui complète la direction donnée par le magnétomètre 3-axes. Les deux informations sont traitées par un observateur d'attitude adapté du filtre complémentaire ; cette adaptation n'est pas triviale et on réalise une étude détaillée de la convergence de l'observateur proposé. L'efficacité de la méthode est illustrée par des résultats sur des données de simulation et des données de vol réel.



# Remerciements

A Nicolas, directeur impliqué, prodigue en conseils avisés et bienveillant. Ce fut un plaisir de travailler avec lui, et cette thèse lui doit énormément.

A Sébastien, pour son accompagnement, sa grande disponibilité, et également pour son accueil lors des (brèves) séquences alsaciennes de ce doctorat.

A Christophe, avec qui il était toujours un plaisir de discuter, et à qui je dois de nombreuses pistes de recherche.

A Pascal Morin et Hélène Piet-Lahanier, rapporteurs de ce manuscrit, pour le temps qu'ils y ont consacré et leurs précieux retours. Aux autres membres du jury, avec qui j'ai eu également plaisir à échanger.

A l'école des Mines et au Centre Automatique et Systèmes, pour ces années passées à y travailler, à y enseigner et à y vivre. Professeurs, co-thésards et étudiants ont fait de ce doctorat une expérience bien moins solitaire qu'on ne me l'avait décrit. J'espère que cette ambiance toute particulière y perdurera encore longtemps. Merci aux anciens (Florent, Delphine, Pauline, Jean, Charles-Henri, Pierre, Naveen), et courage aux suivants (Matthieu, Dilshad, Loris, Hubert, Mona, Nils, Pierre-Cyril)

A Marin, Baptiste et Arnaud, à Sabine et à ma mère, pour leur soutien précieux au moment fatidique ; plus généralement à ma famille et mes amis, pour leur présence et leur patience, dans les moments de joie comme dans les moments de doute.



# Chapitre 1 - Résumé

Ce chapitre introductif pose les bases du problème qui nous a intéressé au cours de cette thèse, et donne des éléments de contexte sur les munitions intelligentes d'une part, et l'estimation d'attitude en général d'autre part. On justifie le rôle central de l'attitude pour la navigation, en illustrant sa nécessité pour le guidage terminal et des applications de télémétrie. Enfin, on introduit brièvement la solution proposée, en la décomposant en plusieurs schémas-blocs : estimation fréquentielle de la vitesse d'une munition, estimation de l'angle de pente de la munition à partir d'une mesure de vitesse, estimation d'attitude à l'aide de la connaissance d'un angle, et finalement reconstitution d'une méthode complète reposant exclusivement sur des capteurs embarqués.



# Chapter 1

## Context and problem statement

### 1.1 Introduction

The topic under consideration in this thesis is the estimation of the attitude of an artillery shell in free flight, during the flight phase termed exterior ballistics. As will be described below, attitude estimation is an essential factor for the development of « smart-shells » or « guided-ammunition » which are capable of achieving various guidance tasks such as in-flight re-targeting and optimization of range. Lately, these topics have been of interest as significant performance improvements are expected from smart-shells compared to currently employed ammunition [30, 81, 105].

The attitude estimation problem belongs to the vast class of state estimation problems for Six-Degrees-of-Freedom (6-DOF) rigid bodies subjected to aerodynamics effects using embedded sensors. As is very common now, many rigid bodies can be equipped with low-cost strapdown inertial sensors, see e.g. [84, 4, 98, 26, 104, 21, 43, 27, 95, 9, 67, 68, 48], to reliably solve navigation problems, at the expense of reasonably complex on-board calculations and off-line tasks such as multi-sensor system calibration [40]. Numerous experiments have been reported in the literature for unmanned aerial vehicles [73, 49, 10, 51, 47], unmanned ground vehicles [86], micro-satellites [94, 62, 90], sounding rockets [5], spacecrafts [75, 59, 62, 90, 89, 88], smart objects [54, 18] among others. Commonly considered sensors are the component of an inertial measurement unit (IMU) : 3-axis Accelerometer, 3-axis Magnetometer and rate gyro (and sometimes GPS which is usually discarded as it is easily subjected to spoofing and jamming, especially in military applications).

However, in our application, several constraints rule out this classic ap-

proach. The trajectory of a shell has a short duration due to its high speed<sup>1</sup>, and, most importantly, is often subjected to a very high spin rate [72, 103, 18, 20, 36], usually favored due to its stabilizing effect on the center of mass trajectory. In practice, the spin rate saturates most low-cost rate gyro and even medium-cost ones [3]<sup>2</sup>, if they are not damaged by the high impact caused by the gunshot, of approximately 20000 G.

Attitude estimation of a rigid body is a far-reaching question in numerous fields of engineering and applied science, especially those including motion control. Classically (see e.g. [27]), following the formulation of the famous « Wahba » problem [101], two vectors measurements, usually assumed to be obtained using accelerometers and magnetometers, are sufficient to algebraically (and unambiguously) reconstruct the attitude of a rigid body. The vastly documented methods to solve Wahba’s problem (see [4, 85]) have been improved in many applications with multi-sensor data fusion, adding rate gyro to the set of sensors, most frequently using Kalman filtering (see e.g. [98]) or, more recently, complementary filtering as in [67, 68, 66]. This last solution is appealing because of its simplicity of implementation (relying on a few nonlinear equations that are readily implemented on-board any embedded system) and the simplicity of its straightforward tuning procedure (very few tuning gains being at stake). While they are not strictly necessary, the rate gyro brings robustness to vector measurements failures, and provides dynamic responsiveness to the estimation filter. Various experiments and works [16, 46, 55, 6, 96] [35, 56, 74, 99, 11, 71, 32, 7, 70] offer alternatives and comparisons of the numerous methods implementing such attitude estimation techniques.

In the context of smart-shells, two of the three sensors composing the commonly considered IMU are troublesome: the rate gyro and the accelerometer.

Due to their high cost and low survival rates after gunshot, it has been proposed to remove the rate gyro from the set of on-board components, advocating a gyroless alternative. Instead of directly measuring the angular velocity, some works have developed solutions for the problem of estimating it (see e.g. [97, 8]). In particular, [65, 63, 64] have offered a way of estimating the angular velocity from vector measurements, even when an unknown torque is applied. This step essentially lowers the levels of robustness and performance of the attitude estimation. Several studies have shown that the losses can be mitigated to acceptable levels provided that dynamical models are exploited [17, 24], rather than ignored as is common practice with IMU technologies (e.g. [3]).

---

<sup>1</sup>which discards low update-rate sensors such as GNSS.

<sup>2</sup>typically, rotation rates of 300 Hz can be considered, which is out of the scale of most low to mid-cost rate gyro, having a maximum range of 9000 deg/s, or 25 Hz.

By contrast, accelerometers and the magnetometers are essential ingredients to estimate the attitude. In a nutshell, the two directions usually considered in Wahba's problem are the gravity vector and the Earth magnetic field. This view is unfortunately simplistic for the case of a shell. As will be discussed later-on, the accelerometer measures a variable (« proper acceleration ») that is a sum of the acceleration minus the gravity, or, equivalently, simply the aerodynamic forces (divided by the mass). The aerodynamics forces are unrelated to the gravity. The acceleration is non negligible in front of the gravity. For these two reasons, the commonly acknowledged assumption that the accelerometer gives the direction of the gravity is simply wrong.

Having the preceding description on mind, it seems quite a challenge to estimate the shell attitude. In this thesis, we propose a novel method, outlined below.

A variable plays a central role in our approach: the (norm of the) velocity w.r.t. the air, as already considered in [78, 100, 80]. This variable is usually of interest in aerodynamics as it serves to define the aerodynamic effects applied on the shell, and its dynamics can be monitored to keep track of the shell ballistic trajectory. The method we propose to estimate this variable is based on the analysis of the rotational oscillations the shell is subjected to. As is well documented [72], and clearly observed during experimental flights, a damped 3-dimensional pendulum-like rotation dynamics is created by aerodynamics effects. The oscillations are clearly visible in the accelerometer readings, under the form of additive pseudo-periodic disturbances lying on top of its absolute readings (the latter being of little value for the reason explained above). The idea leveraged in this thesis is to detect the instantaneous frequencies of the oscillations (decomposed into yawing and pitching) from the accelerometers and to interpret them as information on the velocity. Several frequency detection techniques can be employed for the very general first task [34]. Then, the estimates are reconciled with *a priori* knowledge on the pendulum dynamics taking the form of analytic expressions of the theoretical frequencies involving aerodynamic look-up tables of drag, lift and Magnus effects <sup>3</sup>. Eventually, the (norm of the) velocity w.r.t. the air can be analyzed to estimate one angle: the pitch angle.

At this step, one is left with an unusual reformulation of the general Wahba problem: determine the attitude of a rigid body knowing one direction (the direction of the Earth magnetic field) and one angle. As will be explained, this problem can be solved using a specifically tailored version of the complementary filter proposed in [67].

In the following, the various concepts sketched above are given in more

---

<sup>3</sup>these tables are already at our disposal thanks to preexisting experimental identifications in wind-tunnels, and exterior ballistic tests.

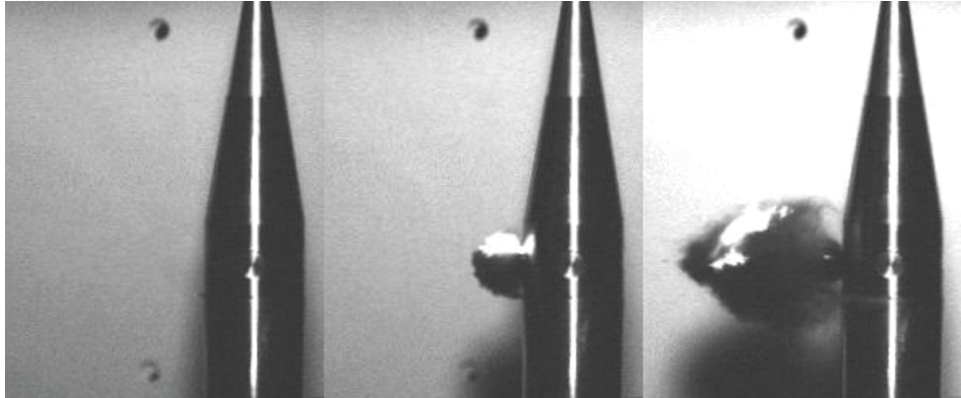


Figure 1.2.1: ISL pyrotechnical thruster.

details.

## 1.2 The concept of smart artillery shells

Gun-fired ammunition are still a prominent part of military arsenals. They are significantly cheaper than missiles, and can easily and promptly be deployed on various battlegrounds. So far, their main limitations is their lack of guidance capabilities, as they cannot be controlled once fired. This major limitation is being pushed back as some recently developed actuation technologies have emerged over the last decades such as single mass ejection (or pyrotechnical thrusters [41] as pictured in Figure 1.2.1 and Figure 1.2.2) or the deployment of canards and have proven to be valuable means to deflect and to optimize the projectile trajectory [12]. A prime example is the folding glide canards found on the M982 Excalibur, a 155 mm extended range guided artillery shell developed during a collaborative effort between the US Army Research Laboratory (ARL) and the United States Army Armament Research, Development and Engineering Center (ARDEC). The fins are utilized to glide from the top of a ballistic arc towards the target. The same concept is being explored in the ISLs guided long range projectile concept pictured in Figure 1.2.3.

The projectiles considered here are rigid bodies with one central symmetry axis. Usually, they have a reference diameter  $D$ , called the caliber. Most of the parameters can be deduced from it for similarly shaped projectiles, through a homothetic transformation.

Most shells have an ogive-shaped nose, a cylindrical central part, and possibly a tapering base (boat-tail). The length  $L$  of gyro-stabilized shells commonly ranges between 4 and 5 calibers, the length of the nose  $h_n$  can



Figure 1.2.2: ISL pyrotechnical thruster in action.

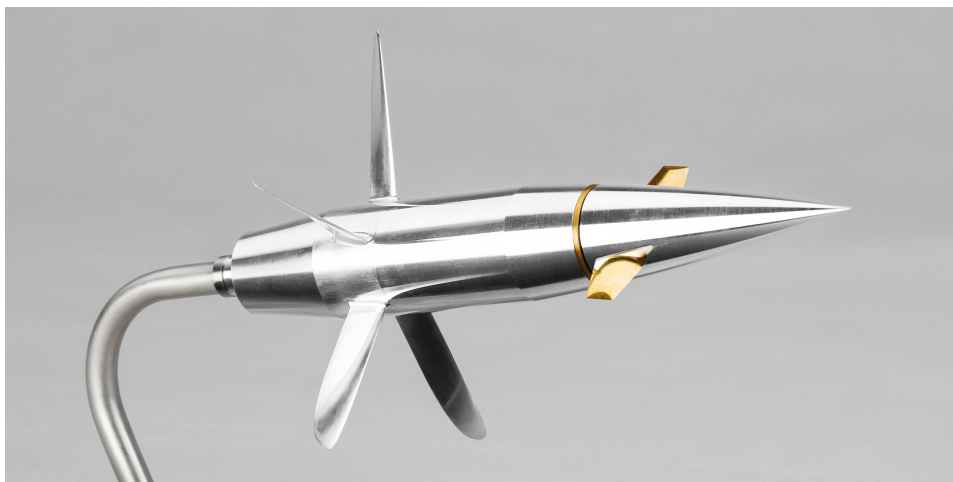


Figure 1.2.3: ISL guided long range projectile.

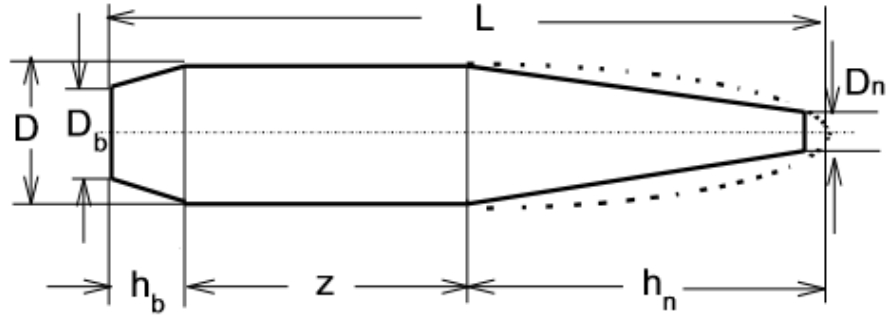


Figure 1.2.4: Definition of studied shells.

vary between 2.5 and 4 calibers and its front can be round-shaped or flat. Finally, the boat-tail typically has a length  $h_b < 0.8 D$  and a diameter  $D_b$  between  $0.8 D$  and  $0.9 D$ . A typical boat-tail shell with a flat nose is pictured in Figure 1.2.4.

Shells are fired by a cannon which provides them with an initial velocity, and most of the time a significant spin rate for stabilization purposes. After gun-fire, they follow a trajectory solely governed by the external forces and moments acting on them during their flight.

Depending on their shape (which in the scope of the thesis is always assumed to be rotationally symmetric), most shells are gyro-stabilized, i.e. submitted to a high spin rate, so that they are stable under normal flight conditions (see the classical gyroscopic stability criterion [72, Chapter 10]). Very often, the value of the spin-rate required for the stability overwhelms the rate gyro range of operation. To circumvent this, decoupled two-section fuse concepts have been developed, having a slowly (almost despun) rotating part containing sensors and possibly actuators. In this thesis, we will not consider these (relatively costly) solutions, and, instead, consider that the rate gyro is not present.

### 1.3 Attitude estimation for smart shells applications

In the context of navigation of smart artillery shells, the knowledge of the attitude is particularly useful as it makes it possible, in addition with 3-axis Accelerometer, to estimate the position of the shell in-flight, i.e. solving a navigation problem<sup>4</sup>. The attitude is also required as an input for control

<sup>4</sup>for short time horizons, the aerodynamic forces measured by the 3-axis Accelerometer can be converted into forces in the inertial frame of reference and added to gravity to

laws (guidance or terminal guidance controllers), and telemetry applications (e.g. antennas orientation to minimize data loss). It is often required in late parts of the flight where trajectory correction have to be made. A typical ballistic flight for smart shell is depicted in Figure 1.3.1. The steered gliding phase taking place after the apogee is a prime example where attitude information is useful.

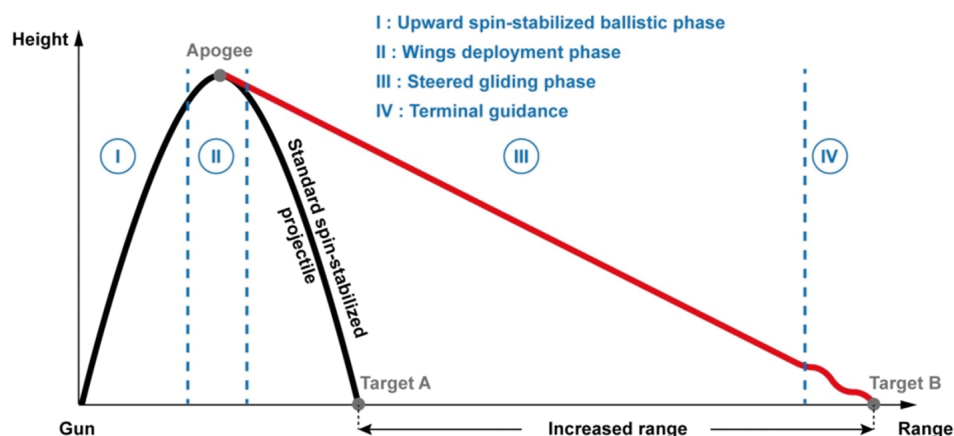


Figure 1.3.1: Typical ballistic flight phases for smart artillery shells. (ISL)

## 1.4 Outline of the proposed solution

As explained earlier, classic attitude estimation methods can not work as-is onboard a smart shell. We will not use any rate gyro, but when needed, an estimate of the angular velocity will be developed (this estimation will be referred to as a « virtual gyro »). The 3-axis Magnetometer will be used as a body-frame measurement of the Earth magnetic field, whose coordinates  $b_0$  in the local frame are known Besides, an additional input will compensate for the missing direction measurement usually given by the 3-axis Accelerometer. The attitude will be represented under the form of a rotation matrix  $\hat{R}$ . A pictorial view of the estimation method is given in Figure 1.4.1.

The « virtual gyro » can be a simple estimation of the dominant roll rate, which will be shown to be easily determined using the large oscillations observed in both transverse accelerometers and transverse magnetometers signals<sup>5</sup>.

---

estimate the true acceleration of the center of mass of the shell, following the classic navigation principles, see e.g. [31].

<sup>5</sup>alternatively, one could use the knowledge of the aerodynamic moments, and the fact that 3-axis Accelerometer provides a good estimation of the angular velocities through that modeling. Of course, using aerodynamic coefficients accordingly requires the knowledge

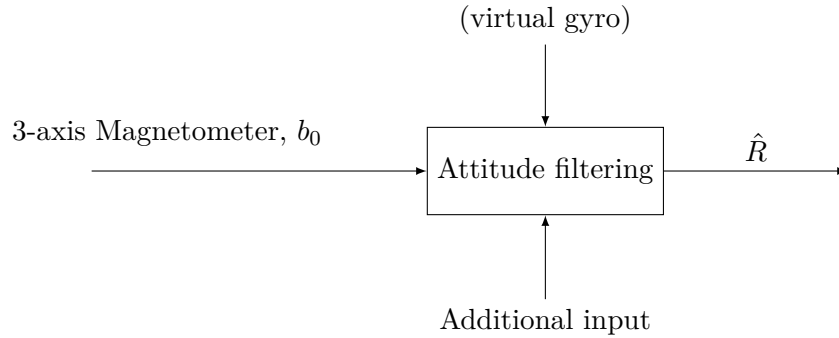


Figure 1.4.1: Attitude Filtering proposed in the thesis.

The norm of the velocity w.r.t. the air can be obtained through a frequency analysis of the pitching and yawing motion induced by the aerodynamic moments. This estimation uses one of the transverse accelerometer as pictured in Figure 1.4.2. It will be detailed in Chapter 3.

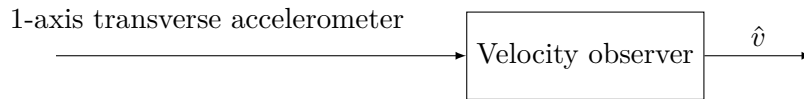


Figure 1.4.2: Velocity Estimation.

To compensate for the missing direction, one attitude angle will be directly estimated. As will be explained, measuring only one direction makes one able to compute the attitude, up to a rotation by an unknown angle around the single known direction. If an additional « well-chosen » attitude angle is available, then the attitude estimation has only two isolated solutions, that can be discriminated easily. The angle under consideration is the pitch angle. It is obtained from the estimate of the velocity w.r.t. the air, as pictured in Figure 1.4.3, which gives an approximation of it under the form of the slope angle. The estimation method will be exposed in Chapter 4. The pitch angle serves as « additional input » for the attitude observer of Figure 1.4.1 as pictured in Figure 1.4.4. This will be treated in Chapter 5.

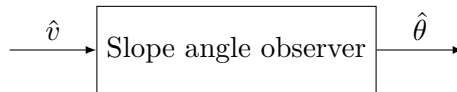


Figure 1.4.3: Slope angle Estimation.

Finally, by connecting all the estimates described above, one obtains the overall attitude estimation methodology proposed in the thesis. It is of the velocity.

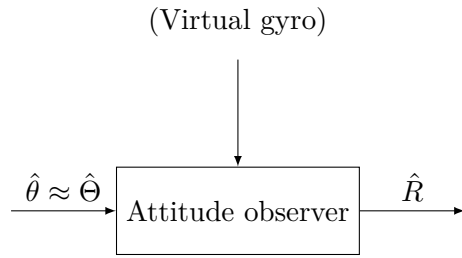


Figure 1.4.4: Attitude Estimation.

described in Figure 1.4.5. It uses a 3-axis Accelerometer (actually, only one of its transverse sensors) and a 3-axis Magnetometer. Experimental results obtained with this method will be given in Chapter 6.

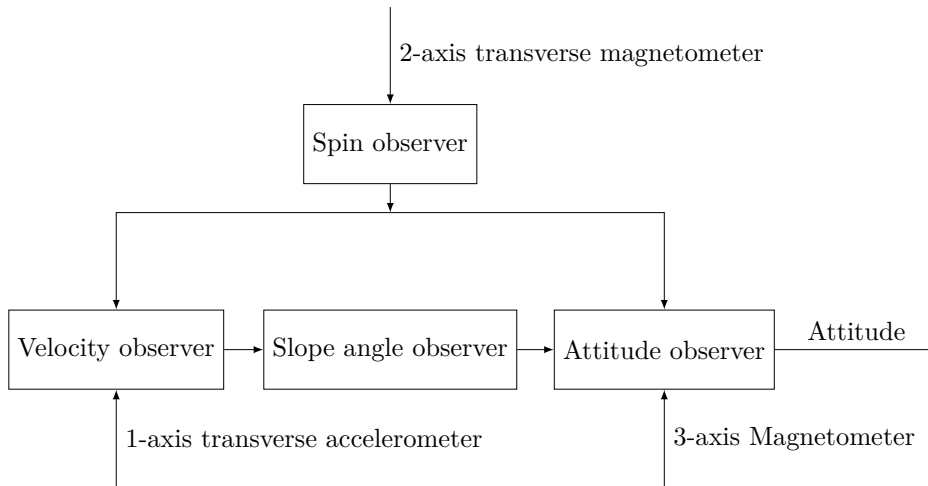


Figure 1.4.5: Attitude Estimation Algorithm from on-board sensors.

## 1.5 Organization of the thesis

The manuscript is organized as follows.

Chapter 2 presents the mathematical notations employed to describe the flight dynamics of the shell under the form of a 6-degrees of freedom model of a rigid body subjected to aerodynamic forces and moments, and gravity. The two types of rotationally symmetric shells (155 mm and Basic Finner) under consideration in the thesis are described. The main equation governing the pitching and yawing motion of the shell is presented. The combined oscillations define an epicyclic motion. The set of strapdown sensors is described. Some data obtained during experimental tests serve to illustrate typical measurements observed in-flight.

In Chapter 3, the signals generated by the epicyclic motion of the shell are processed by frequency detection techniques. The frequency is related to the norm of the velocity w.r.t. the air of the shell. This relation is a key ingredient for the velocity estimator that is developed to account for observability issues near Mach 1.0.

In Chapter 4, the previously developed velocity estimation serves to establish an estimation of the pitch angle of the shell. A simple linear time varying (LTV) formulation serves to establish the convergence of a Luenberger observer, which can be replaced for sake of improved performance with an extended Kalman filter.

Chapter 5 develops an extension of the attitude complementary filter dealing with a single vector measurement and the knowledge of one angle. The convergence analysis is established.

Finally, Chapter 6 is devoted to the application of all the methods presented above to real flight data, using solely on-board measurements. Comparisons with high-fidelity measurements from a ground based position radar are provided.

Conclusions and perspectives are given in Chapter 7.

## Chapitre 2 - Résumé

Ce second chapitre permet la mise en équation du problème, en introduisant les différents repères utilisés, la nomenclature des différents états considérés, et les paramètres physiques propres à la munition et à son environnement. On y décrira en partie la dynamique de vol d'une munition, en distinguant dynamiques de translation et de rotation, et en mettant en évidence les équations sur lesquelles reposeront nos différentes estimations. Les différents capteurs à notre disposition sont présentés ici, ainsi que les problèmes pratiques auxquels leur utilisation nous confronte (accélérations d'entraînement, induction), et la structure du signal qu'ils mesurent. Bien qu'on se passe de gyromètres, on présentera également des méthodes d'estimation de vitesse angulaire simplifiée à partir des capteurs dont on dispose. Enfin, ce chapitre se conclut par la présentation du dispositif expérimental utilisé et des jeux de données considérés dans cette thèse.



## Chapter 2

# Mathematical formulation, notations, flight dynamics and instrumentation

### 2.1 Reference frames and Six-Degrees-of-Freedom description

Let the frame  $L$  be defined by orthogonal unit vectors  $1^L, 2^L, 3^L$  where  $1^L$  direction is the direction of the shot on the horizontal plane and  $3^L$  is vertical and pointing to the ground. This direct frame, referred to from now on as the « local frame », is an adaptation of the classical « North-East-Down » (NED) frame commonly used in aeronautics, rotated so that its first vector is oriented in the initial direction of the shot.

Classically, the shell can be modeled as a Six-Degrees-of-Freedom (6-DOF) rigid body. The full notations are summarized in Table 2.1.1. The orientation of the rigid body is defined by a set of three Tait-Bryan angles (here « ZYX » angles are chosen, following the nomenclature of [58], where, as commonly considered, the spin is defined as the rotation about its axis of least inertia). As a result, the orientation of the body with respect to the local inertial frame is described by the Tait-Bryan angle sequence:

yaw:  $\Psi$ , pitch:  $\Theta$ , roll:  $\Phi$

The shell state comprises 12 variables, namely the position, velocity, attitude (under the form of the three angles previously introduced) and angular velocity. It reads

$$(2.1.1) \quad X_{full} = (x \ y \ z \ v_x \ v_y \ v_z \ \Psi \ \Theta \ \Phi \ p \ q \ r)^T$$

$x, y, z$	Position of the shell in the local frame
$v_x, v_y, v_z$	Velocity of the shell w.r.t. the local frame
$h = -z > 0$	Altitude of the shell
$V$	Velocity of the shell w.r.t. the airflow
$v =  V $	Scalar velocity of the shell w.r.t. the airflow
$N_{mach}$	Mach number of the shell
$v_B^I$	Velocity of the shell w.r.t. the local frame
$X$	Position of the shell w.r.t. the local frame
$R = [T]^{LB}$	Attitude matrix of the shell (transition matrix from the local frame to the body frame)
$\Psi, \Theta, \Phi$	Tait-Bryan angles
$\Psi$	Yaw angle
$\Theta$	Pitch angle
$\Phi$	Roll angle
$\Omega = (p, q, r)$	Angular velocity of the shell w.r.t. the local frame expressed in the body frame
$\omega_L^I$	Angular velocity of the local frame w.r.t. a geocentric frame (Earth's rotation, adding Coriolis effect)
$p = \langle \Omega, 1^B \rangle$	Spin rate of the shell (or longitudinal component of $\Omega$ )
$q = \langle \Omega, 2^B \rangle$	transverse component of $\Omega$ along $2^B$
$r = \langle \Omega, 3^B \rangle$	transverse component of $\Omega$ along $3^B$
$[T]^{BW}$	Transition matrix from the body frame to the wind velocity frame
$\alpha, \beta$	Incidence angles (see below)
$\alpha$	Attack angle
$\beta$	Sideslip angle
$\alpha_t$	Total angle of attack of the shell (angle between vectors $1^B$ and $V$ )
$\theta$	Slope angle (« pitch » angle of $[T]^{LW}$ in « ZYX » decomposition)

Table 2.1.1: Nomenclature.

This vector contains several groups of variables of interest. Let us define the following partial state variables : the position  $X$ , the velocity  $V$  (and

its norm  $v = |V|$ ), three angles defining the attitude matrix  $R$  (and the corresponding quaternion  $q$ ) and the angular velocity  $\omega$ . Details are given in (2.1.2).

We note  $(e_1, e_2, e_3)$  a canonical base of  $\mathbb{R}^3$ ,  $R_{a,v}$  the matrix defining the 3D-rotation of angle  $a$  about the vector  $v$ , and  $q_{a,v}$  one of the two unit quaternions representing  $R_{a,v}$  (see Section 5.1 for more details). Conversely, the  $R_{a,v}$  matrix can be derived from the quaternion  $q_{a,v}$ , see Section 5.1.

$$(2.1.2) \quad \begin{cases} X = (x \ y \ z)^T \\ V = (v_x \ v_y \ v_z)^T \\ R = [T]^{LB} = R_{\Psi, e_3} R_{\Theta, e_2} R_{\Phi, e_1} \\ q = q_{\Psi, e_3} \otimes q_{\Theta, e_2} \otimes q_{\Phi, e_1} \\ \Omega = (p \ q \ r)^T \end{cases}$$

Besides the local (inertial) frame  $L$  and the body  $B$  frame, a third frame is considered and referred to as the « wind velocity frame », denoted  $W$ . It is defined from the body frame using the velocity of the shell with respect to the airflow, denoted  $v_B^A$  or  $V$ , as described by Figure 2.1.1.

The attack angle  $\alpha$  and the sideslip angle  $\beta$  are defined by

$$(2.1.3) \quad [T]^{BW} = R_{-\alpha, e_2} R_{\beta, e_3}$$

where  $[T]^{BW}$  is the transition matrix from the body frame to the wind velocity frame

The angles between the frames  $L$ ,  $B$  and  $W$  are illustrated in Figure 2.1.1 (with the introduction of an intermediate frame  $L'$ ) and Figure 2.1.2.

## 2.2 Environment model

The environment of the shell is modeled with standard atmosphere, gravity, and Earth magnetic field reference models. In details, following the Standardization Agreement STANAG 4355 from NATO, the gravitational acceleration at altitude  $h$  is

$$(2.2.1) \quad g(h) = g_0 \left( \frac{R}{R+h} \right)^2$$

where

$$g_0 = 9.80665 \times (1 - 0.0026 \cos(2 \text{Lat}))$$

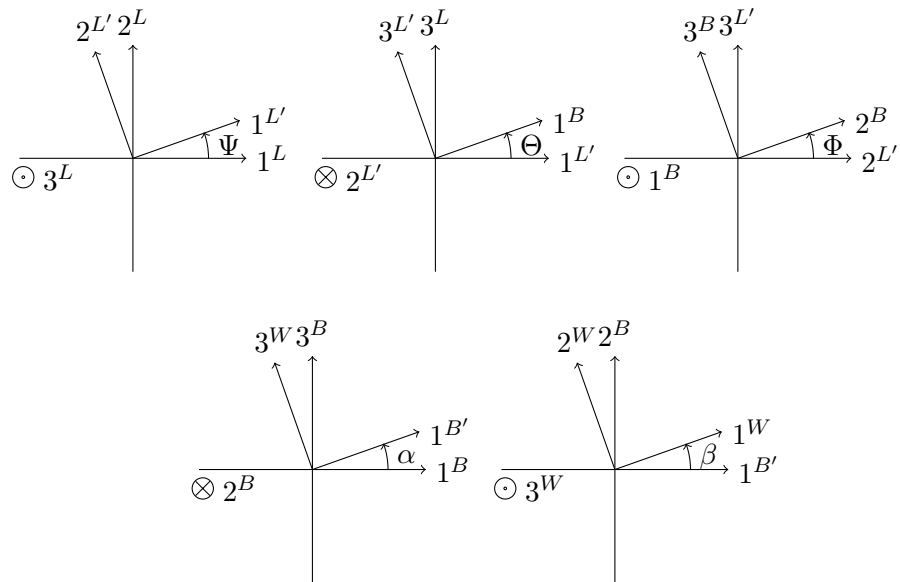


Figure 2.1.1: Definition of Tait-Bryan and incidence angles.

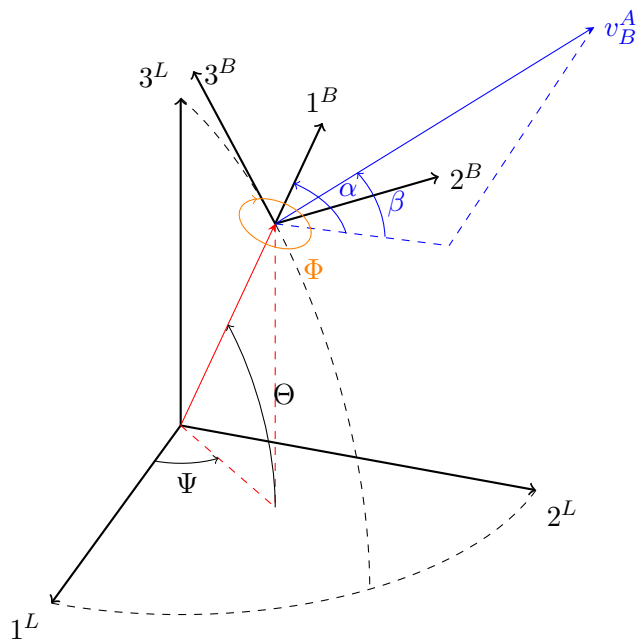


Figure 2.1.2: Definition of Tait-Bryan and incidence angles at  $\Phi = 0$  ;  $\alpha$  refers to a rotation around  $2^B$  and  $\beta$  around  $3^W$ .

while  $R$  is an average value of the Earth radius and  $\text{Lat}$  is the geodetic latitude of the local frame  $L$  ( $g$  slightly increases when moving away from the equator).

At any altitude  $h$ , the air density is given, following [39],

$$(2.2.2) \quad \rho(h) = \rho_0 \left( \frac{T_0 - 0.0065h}{T_0} \right)^{4.2561}$$

with  $\rho_0$  the air density on the ground. In turn, this defines the sound velocity

$$(2.2.3) \quad v_{\text{sound}}(h) = a_0 \left( \frac{T_0 - 0.0065h}{T_0} \right)^{\frac{1}{2}}$$

where  $a_0$  is the velocity of the sound at ground level. The Mach number is, as usual,

$$(2.2.4) \quad N_{\text{mach}}(v, h) \triangleq \frac{v}{v_{\text{sound}}(h)}$$

This variable is a main input of the aerodynamic forces and moment look-up tables introduced in Section 2.3.

The various constants appearing in the previous equations are given in Table 2.2.1.

Constant	value	unit
$\rho_0$	1.225	kg.m <sup>-3</sup>
$a_0$	340.429	m.s <sup>-1</sup>
$R$	$6.356766 \times 10^6$	m
Lat	45	deg
$T_0$	288.16	K

Table 2.2.1: Environment constants.

Throughout the thesis (in simulation and for the analysis of actual flight data), the values for the environment constants are those reported in Table 2.2.1.

## 2.3 Projectile model: dimensional parameters and aerodynamic coefficients

In the thesis, we consider two types of projectiles : 155 mm shells, fired with a high spin rate thanks to a rifled barrel (granting gyroscopic stability), and

Basic Fanners, which are smaller and lighter, fired without any initial spin rate but possessing roll-inducing fins<sup>1</sup>.

The 155 mm is an all-purpose standard for NATO armies. The Basic Finner is a more recent experimental shell which has served for many years as a reference projectile and was tested extensively in numerous aero-ballistic ranges and in wind tunnels. The model consists of a 20 deg nose cone on a cylindrical body with four rectangular fins. The main dimensional parameters of the projectiles are listed in Table 2.3.1 with typical values detailed in Table 2.3.2. Reliable look-up table for their aerodynamic coefficients have been established (see e.g. [102, 15, 28, 1]).

$D$	Caliber of the shell
$S$	Reference area of the shell
$M$	Mass of the shell
$I_l$	Longitudinal moment of inertia
$I_t$	Transverse moment of inertia
$\delta_{fin\ cant}$	Angle of the fins with the shell outer surface (for Basic Finner only)

Table 2.3.1: Dimensional parameters.

Type	D (m)	S (m <sup>2</sup> )	M (kg)	$I_l$ (kg.m <sup>2</sup> )	$I_t$ (kg.m <sup>2</sup> )
Basic Finner	0.028	$6.16 \times 10^{-4}$	0.4	$4.36 \times 10^{-5}$	$2.14 \times 10^{-3}$
155 mm	0.155	$1.89 \times 10^{-2}$	43.25	0.15	1.61

Table 2.3.2: Type of projectiles studied.

The coefficients defining the aerodynamics forces and moment are listed in Table 2.3.3. Their values are reported as a function of the Mach number in Figure 2.3.1 for the 155 mm artillery shell and in Figure 2.3.2 for the Basic Finner, for a total angle of attack of zero degree. All the variables in Table 2.3.3 are functions of  $(N_{mach}, \alpha_t)$ .

## 2.4 Flight dynamics

For generality, the high velocity shell under consideration is a 6-DOF rigid body which is given both initial translational velocity and spin rate<sup>2</sup> by

<sup>1</sup>more precisely, a specific spin rate can be achieved by setting the initial velocity of the projectile and the angle  $\delta_{fin\ cant}$  of its fins.

<sup>2</sup>in the case of the Basic Finner, the initial spin rate can be simply set to zero.

$C_D$	Drag force coefficient
$C_{L\alpha}$	Lift force coefficient
$C_{mag-f}$	Magnus force coefficient
$C_{mag-m}$	Magnus moment coefficient
$C_{l\delta}$	Rolling moment coefficient
$C_{spin}$	Roll damping moment coefficient
$C_{Mq}$	Pitch damping moment coefficient
$C_{M\alpha}$	Overturning moment coefficient

Table 2.3.3: Aerodynamics coefficients. All the variables in Table 2.3.3 are functions of  $(N_{mach}, \alpha_t)$ .

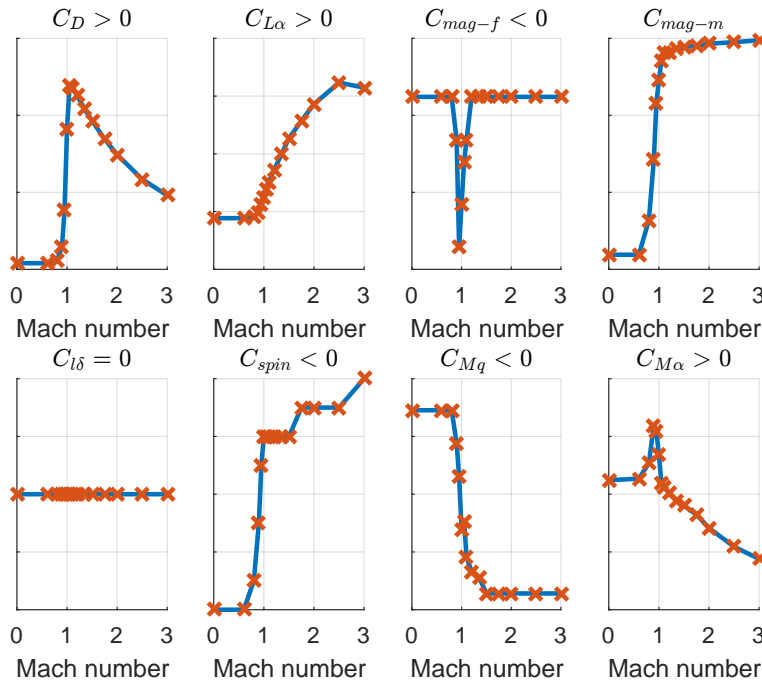


Figure 2.3.1: Aerodynamic coefficients profiles for 155 mm artillery shell.

the gun launch. By contrast with rocket-propelled devices, the shell has a constant mass during the whole flight. It is subjected to drag and lift forces, Magnus forces, Coriolis force, gravity, and several moments: Magnus, overturning <sup>3</sup>, rolling <sup>4</sup>, pitch damping and roll damping moments [72, 60].

<sup>3</sup>aerodynamic moment associated with the lift which is applied at the center of pressure.

<sup>4</sup>only for differentially canted finned shells, as the Basic Finner.

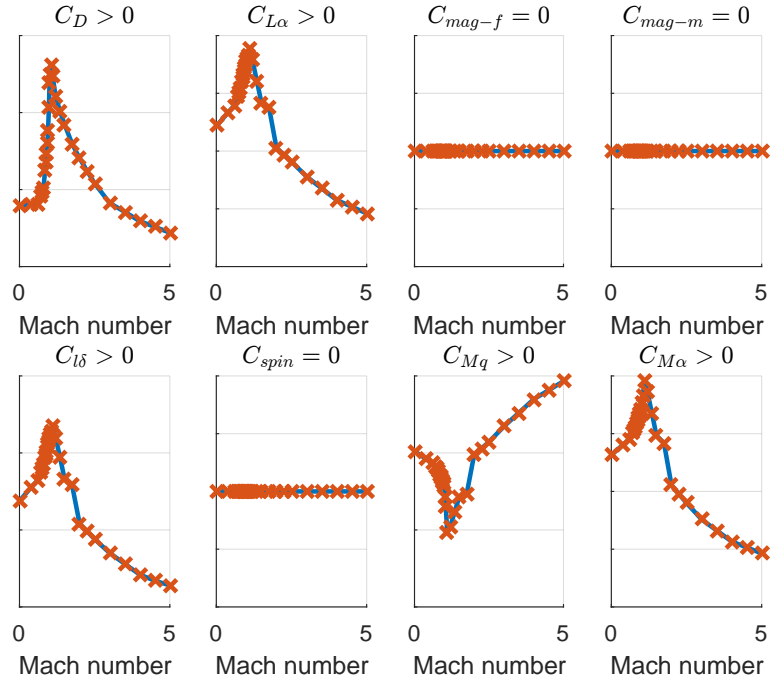


Figure 2.3.2: Aerodynamic coefficients profiles for Basic Finner.

These forces and moments have been extensively studied and measured using wind tunnels, free-flight ballistic ranges, spark and Schlieren photography among others methods. Experimentally established look-up tables are available for the two projectiles under consideration (see e.g. [102, 15]). Concise expressions are given in Table 2.4.1 and Table 2.4.2, respectively.

Force	Expression
Drag force	$-\frac{1}{2}\rho S C_D v v_B^A$
Lift force	$\frac{1}{2}\rho S C_{L\alpha} \left( v_B^A \times \left( 1^B \times v_B^A \right) \right)$
Magnus force	$\frac{1}{2}\rho S \left( \frac{p^D}{V} \right) C_{mag-f} v \left( v_B^A \times 1^B \right)$
Coriolis force	$2M v_B^I \times \omega_L^I$
Weight	$Mg$

Table 2.4.1: Forces applied on the shell.

Moment	Expression
Magnus moment	$\frac{1}{2}\rho SD \left(\frac{pD}{v}\right) C_{mag-m} v \left(1^B \times \left(v_B^A \times 1^B\right)\right)$
Overturning moment	$\frac{1}{2}\rho SDC_{M\alpha} v \left(v_B^A \times 1^B\right)$
Rolling moment	$\frac{1}{2}\rho SD\delta_{fin\ cant} C_{l\delta} v^2 1^B$
Pitch damping moment	$\frac{1}{2}\rho SD^2 C_{Mq} v \left(1^B \times \left(\Omega \times 1^B\right)\right)$
Roll damping moment	$\frac{1}{2}\rho SD \left(\frac{pD}{v}\right) C_{spin} v^2 1^B$

Table 2.4.2: Moments applied on the shell.

### 2.4.1 Translational dynamics

After some reordering, the application of Newton Second Law yields, in a concise form

$$(2.4.1) \quad \dot{v} = -\frac{\rho S \tilde{C}_D v^2}{2M} - g \sin \theta, \quad \dot{h} = v \sin \theta$$

with

$$(2.4.2) \quad \tilde{C}_D(h, v, \alpha_t) \triangleq C_D(N_{mach}(h, v), \alpha_t)$$

Equation (2.4.1) is obtained with some approximations, namely neglecting the difference between  $V$  the velocity of the shell w.r.t. the airflow and  $\dot{X}$  the velocity in the local frame, and the contribution of the Coriolis force. Those approximations are detailed in Appendix A.3.

In (2.4.1), the drag is a dominant effect and deserves some more comments. Some effects of the shell shape on the drag coefficient at various Mach numbers have long been studied. Those effects depend on a number of dimensionless variables. The fluid mechanism that transmits the drag force to the shell consists of two parts: surface pressure and surface shear stress (a.k.a. skin friction drag). The force generated on the forebody and the base of the shell are different. Therefore, the various components of the drag force behave in significantly different ways in the various speed regions. At subsonic flight speeds (below Mach 1.0), the drag coefficient is essentially constant. It rises sharply near Mach 1.0, then slowly decrease at higher supersonic speeds. The sudden rise appearing just below Mach 1.0 is caused by the formation of shock waves in the flow-field surrounding the shell [72]. This rise is visible in the  $C_D$  profiles of Figure 2.3.1 and Figure 2.3.2.

## 2.4.2 Rotational dynamics

Euler equation of rotation of a rigid body subjected to external aerodynamic moments can be written under the following form. One shall note the cancellation of the bilinear term  $q r$  in (2.4.3) due to the symmetric nature of the shell.

$$(2.4.3) \quad \dot{p} = \frac{\rho(h)SD^2C_{spin}v}{2I_l}p + \frac{1}{2}\rho(h)SD\delta_{fin\ cant}C_{l\delta}v^2$$

$$(2.4.4) \quad \dot{q} = \frac{1}{I_t} \left( (I_l - I_t)pr + \frac{1}{2}\rho SpD^2C_{mag-m}v\beta + \frac{1}{2}\rho SDC_{M\alpha}v^2\alpha + \frac{1}{2}\rho SD^2C_{Mq}vq \right)$$

$$(2.4.5) \quad \dot{r} = \frac{1}{I_t} \left( (I_l - I_t)pq + \frac{1}{2}\rho SpD^2C_{mag-m}v\alpha - \frac{1}{2}\rho SDC_{M\alpha}v^2\beta + \frac{1}{2}\rho SD^2C_{Mr}vr \right)$$

As is exposed in the early work of [42], the complex reaction of the shell to aerodynamic forces and moment has a much simplified form when its axis of symmetry, its axis of rotation and the direction of motion of its center of mass though the air all coincide. This is precisely the case for the shells studied in the thesis. Actually, more advanced calculus, and several steps of careful first-order approximations<sup>5</sup>, see [72, Chapter 10], allow one to derive the equation governing the Pitching and Yawing motion of the rotationally symmetric projectiles.

Our choice of incidence angles  $\alpha$ ,  $\beta$  differ from [72]. Ours are attached to the body, which makes it easier to relate them to the measurement of both strapdown transverse accelerometers (these angles are oscillating at the spin rate frequency), whereas in [72] the angles correspond to the horizontal and vertical oscillating motion as could be observed from the ground. Note  $\alpha_2$  and  $\beta_2$ , the angles considered by [72] (see Appendix A.2 for alternate angles definition and approximation). The correspondence is given, under a small total angle of attack assumption (see Appendix A.2) by

$$(2.4.6) \quad \begin{cases} \alpha_2 = \sin(pt)\alpha - \cos(pt)\beta \\ \beta_2 = -\cos(pt)\alpha - \sin(pt)\beta \end{cases}$$

By introducing the *complex yaw*

$$\xi = \alpha_2 + i\beta_2$$

---

<sup>5</sup>during the whole flight (typically lasting less than 45s for ballistic flight and less than 2s for flat-fire) the spin rate remains very high, and the angles of attitude w.r.t. the wind frame remain small. Therefore, it is possible to study the attitude dynamics, and, in turn, the translational dynamics, under the assumption of small-angles.

one obtains the following complex valued ordinary differential equation

$$(2.4.7) \quad \ddot{\xi} + \frac{v}{D}(H - iP)\dot{\xi} - \frac{v^2}{D^2}(M + iPT)\xi = -iPG$$

with

$$\begin{aligned} H &= C_{L\alpha}^* - C_D^* - \frac{MD^2}{I_t}(C_{Mq}^* + C_{M\alpha}^*), & P &= \frac{I_l pD}{I_t v} \\ M &= \frac{MD^2}{I_t}C_{M\alpha}^*, & T &= C_{L\alpha}^* + \frac{MD^2}{I_l}C_{mag-m}^*, & G &= \frac{gD \cos \Phi}{v^2} \end{aligned}$$

where for each aerodynamic coefficient  $C_X$  one uses the scaled proxy

$$C_X^* = \frac{\rho SD}{2M}C_X$$

The complex equation (2.4.7) will be central in the works presented in the thesis. It has been established by several authors, under various forms, which are all equivalent: [52, 53, 76, 39], among others. Also, it has been shown to be a very good approximation to the actual flight of symmetric projectiles.

This equation is a linear, second order differential equation with « almost constant » (slowly-varying) complex coefficients. Assuming now that the coefficients are indeed constants (as a short-term approximation), solving (2.4.7) reveals that the pitching and yawing motion of a symmetric projectile consists of two modes that rotate at different frequencies so that the complex yaw  $\xi$  follows an *epicyclic motion* in the complex plane, i.e. a motion of the general form<sup>6</sup>

$$(2.4.8) \quad \xi(t) = A_n e^{i\omega_n t} + A_p e^{i\omega_p t} + A_0$$

where  $\omega_n$  and  $\omega_p \ll \omega_n$  designate the so-called « nutation » and « precession » angular frequencies, respectively. The epicyclic motion is pictured in Figure 2.4.1.

Going back to the « body-attached » incidence angles  $\alpha$  and  $\beta$  which are, by solving (2.4.6),

$$(2.4.9) \quad \begin{cases} \alpha = \sin(pt) \alpha_2 - \cos(pt) \beta_2 \\ \beta = -\cos(pt) \alpha_2 - \sin(pt) \beta_2 \end{cases}$$

one has that (2.4.8) yields (2.4.10) through  $\alpha + i\beta = -e^{ipt}(\beta_2 + i\alpha_2)$

$$(2.4.10) \quad \alpha + i\beta = -i \left( A_n e^{i(p-\omega_n)t} + A_p e^{i(p-\omega_p)t} + A_0 e^{ipt} \right)$$

---

<sup>6</sup>This expression is only a short-term approximate solution.

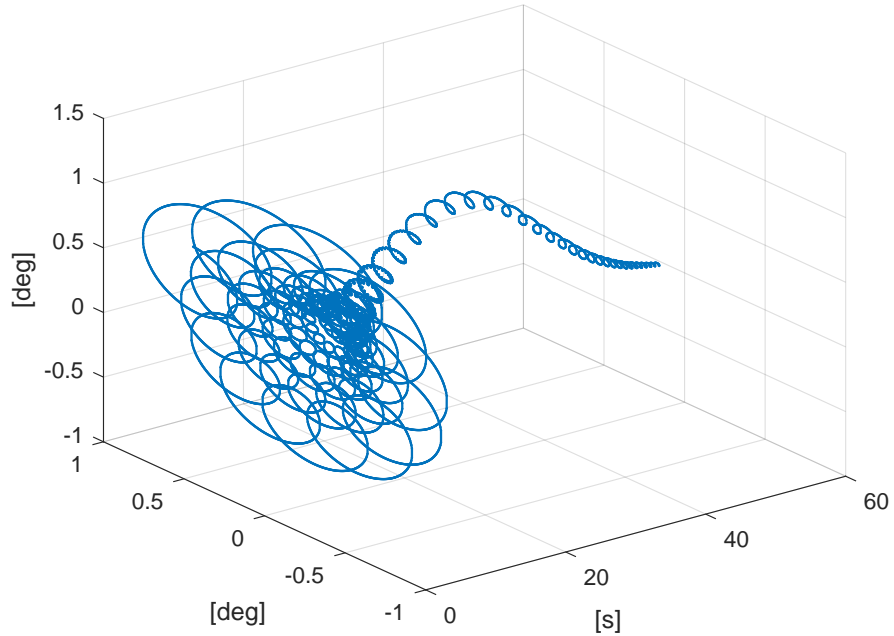


Figure 2.4.1: Epicyclic motion of the shell during a typical flight ; locus of the complex yaw  $\xi$  from Equation (2.4.8) [simulation results].

## 2.5 Onboard Sensors

### 2.5.1 Description of the embedded system

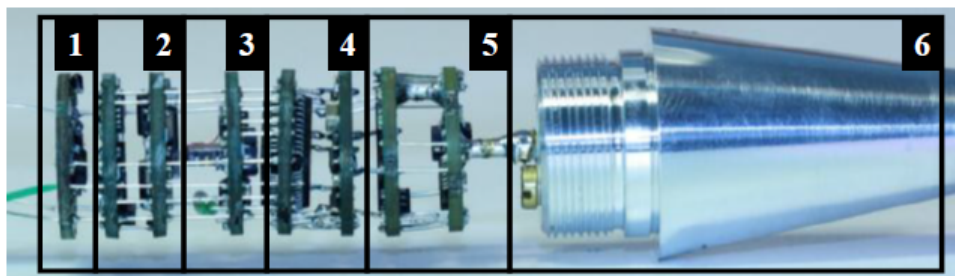


Figure 2.5.1: Embedded Instrumentation in a Basic Finner, from [19].

① Power supply unit, ② 3-axis Magnetometer, ③ 3-axis Accelerometer, ④ CPU (for signal conditioning), ⑤ RF Transmitter, ⑥ Monopole Antenna.

The strapdown sensors embedded into the shells (see Figure 2.5.1) consists of a 3-axis Accelerometer and a 3-axis Magnetometer. The data from the sensors is collected and sent by the radio Frequency transmitter using

the cone of the shell as a monopole Antenna during the flight. The bandwidth allows to stream 2 megabytes of data per second with a low level of data losses<sup>7</sup>. All sensors are synchronous and sampled at the same rate ( $T = 124 \mu\text{s}$  for experiments,  $T = 100 \mu\text{s}$  in simulations).

The measurement equation are given in (2.5.1).

$$(2.5.1) \quad \begin{cases} Y_{acc} = \dot{V} - R^T g = \frac{F_{ext}}{M} - R^T g = \frac{F_{aero}}{M} \\ Y_{mag} = R^T b_0 \end{cases}$$

The 3-axis Accelerometer measures the *proper acceleration* (or acceleration relative to a free-fall) of the shell, i.e. the sum of the aerodynamic forces  $F_{ext}$  applied onto the shell (divided by the mass), which varies according to

1. the shell velocity (and the associated incidence)
2. its altitude (directly through the corresponding air density, and indirectly through the Mach number)
3. and its spin rate, mostly through Magnus effect.

In turn, the 3-axis Magnetometer provides a measurement of the Earth magnetic field  $b_0$  expressed in the body frame. Any rotation about the Earth magnetic field vector leaves the measurement unchanged, which clearly indicates that the magnetometry measurements are not sufficient for estimating the shell attitude.

Classically, in aircraft applications where during most of the flight the applied forces compensate each other<sup>8</sup>, the actual acceleration  $\dot{V}$  remains close to zero, so that the proper acceleration measured by accelerometers verifies  $Y_{acc} \simeq -R^T g$ . This is the main reason why accelerometers are commonly used as a vector measurement, by improperly considering that they measure the vector gravity  $g$ . Under such circumstances, (2.5.1) boil down to the measurement of two linearly independent vectors ( $b_0$  being almost never co-linear to  $g$ <sup>9</sup>), which readily allows one to solve Wahba's problem of attitude determination.

However, in our case of free-flight,  $\dot{V}$  remains non-negligible from gunshot until the end of the flight. The shell has no thrust, and is not designed in a way such that aerodynamic forces could (even approximately) compensate its weight, the two variables remaining unrelated. The proper acceleration is different from  $-R^T g$ , and the difference is strongly varying along the

<sup>7</sup>as will be visible when treating data, some outliers appears, especially at the end of the flight when the shell is the farthest from the receiving antenna.

<sup>8</sup>mostly thanks to thrust and a design making lift sufficient to compensate gravity at the velocities reached thanks to the thrust.

<sup>9</sup>this would be false above the North Pole, strictly speaking.

trajectory, since it corresponds to the aerodynamic forces changing rapidly with the Mach number, the total angle of attack, and the altitude. This prevents us from using accelerometers as a vector measurement. We will see in the following chapters how to circumvent this problem and find a novel usage of its measurement, providing insights into incidence angles and velocities, with the help of reliable aerodynamic models.

## 2.5.2 Detrimental effects and mitigation means

### Eddy currents

Once embedded into the shell, the 3-axis Magnetometer no longer directly provides a valuable vector measurement, because it is corrupted by an induction effect created by the high spin rate of the electrically conductive shell. This rotation around its main axis is the root cause for eddy currents. The effects of eddy currents are mitigated by suppressing the known induction response to a given spin rate, previously modeled and measured on a testbed (see Figure 2.5.2) [19]. In the rest of the thesis, it is assumed that the induction effects are already compensated for. This assumes that the spin rate is measured, which will be a question treated first of all, in Section 2.6.

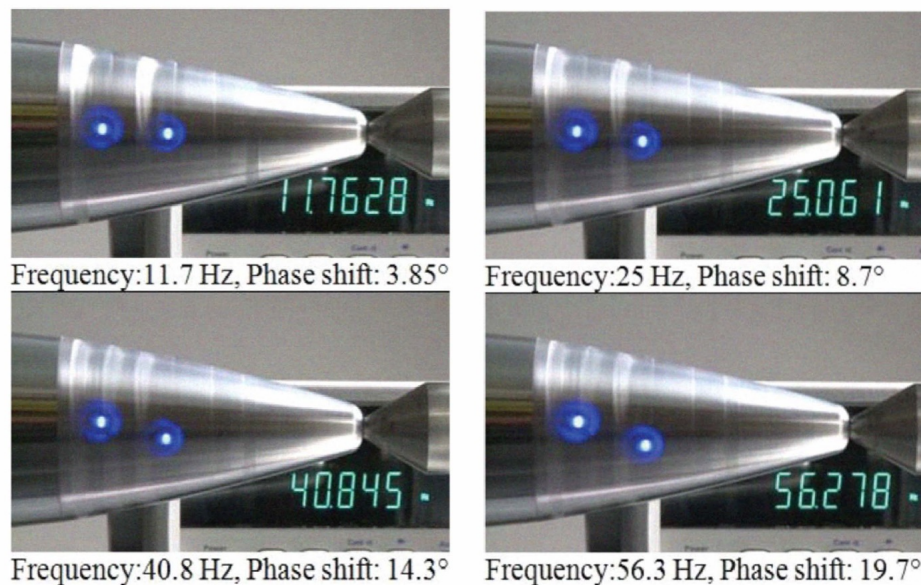


Figure 2.5.2: Compensation of eddy currents effect on 3-axis Magnetometer. Two blinking LEDs are synchronized for various spin rates, showing the accuracy of the model-based compensation[19].

## Misalignment

Ideally, the sensors should be perfectly aligned with the body frame. In practice, there exists a (usually small) rotation between the sensors frame and the body frame, which results in a malicious modulation visible in the signals. In theory, there should be no oscillations at the spin rate frequency on the longitudinal magnetometer. This fact suggests a procedure to reduce the misalignment issue. Conversely, by applying to the 3-axis Magnetometer measurement the rotation minimizing the variance of the longitudinal component enables us to have an *a posteriori* better feedback. Ideally, a similar procedure could be done on the ground prior to the shot with sufficiently fast varying external magnetic field (generated by Helmholtz bobbins). The benefits of the misalignment compensation, and the reduction of the variance of the signal after the rotation, is shown on real flight data in Figure 2.5.3.

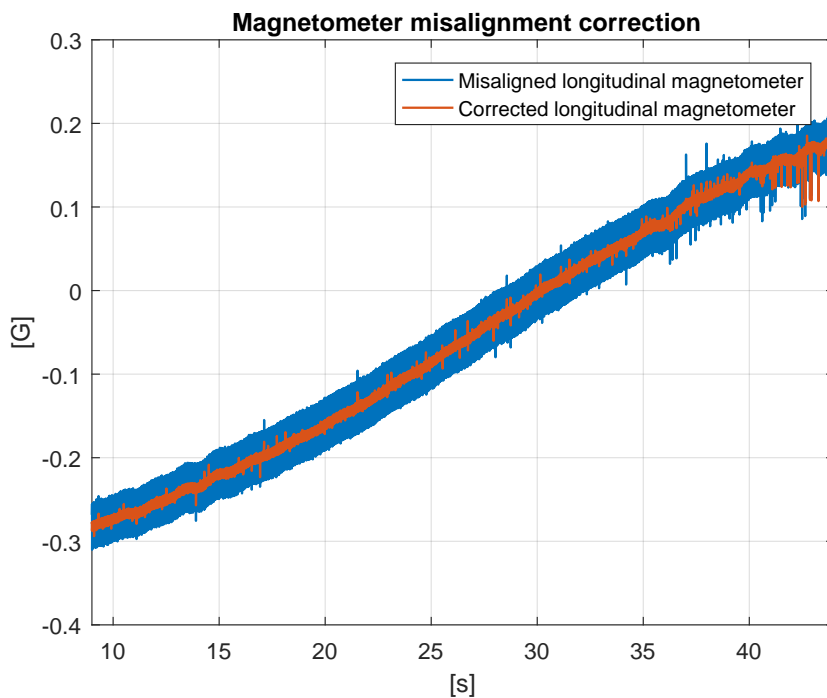


Figure 2.5.3: Compensation of the longitudinal magnetometer misalignment. A rotation of approximately 4 deg was employed. [155 mm experimental data].

After correction of the misalignment and eddy currents, the 3-axis Magnetometer gives signals that are close to theory, but significantly corrupted by the spin rate, as can be seen in Figure 2.5.4

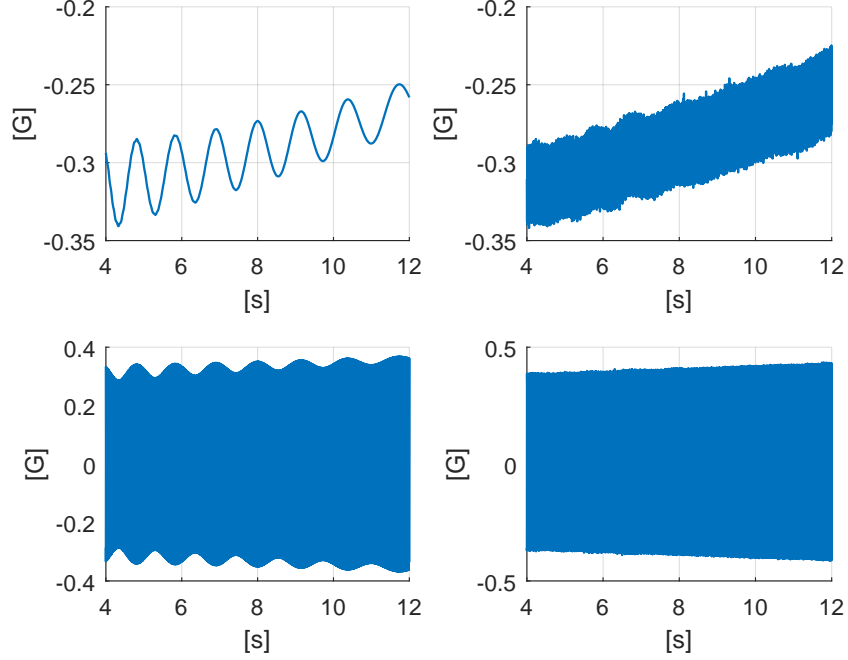


Figure 2.5.4: Values of longitudinal and transverse 3-axis Magnetometer signals in 155 mm shell : simulation (left), experimental (right). No misalignment correction is shown on experimental data, hence the heavy spin rate oscillations in the longitudinal measurement.

### Fictitious forces

The accelerometers are disturbed by fictitious forces. Indeed, due to the high values of spin rate under consideration, even small misalignments (see above) or lateral shift of the sensors from the shell main axis induce substantial fictitious forces which directly corrupt the readings of the 3-axis Accelerometer. Interestingly, this will prove to be harmless for the frequency-based method we develop in the thesis. For reasons we will detail in Chapter 3, the dominant fictitious forces share the same frequency content as the ideal accelerometers.

In details, let  $Y_{acc0}$  denote the proper acceleration measured at the center of mass of the shell, then the proper acceleration occurring at a location shifted by a vector  $r$  is

$$(2.5.2) \quad Y_{acc} = Y_{acc0} + \Omega \times (\Omega \times r) + \frac{d\Omega}{dt} \times r$$

As is clearly visible in Figure 2.5.5, the longitudinal component of  $r$  is

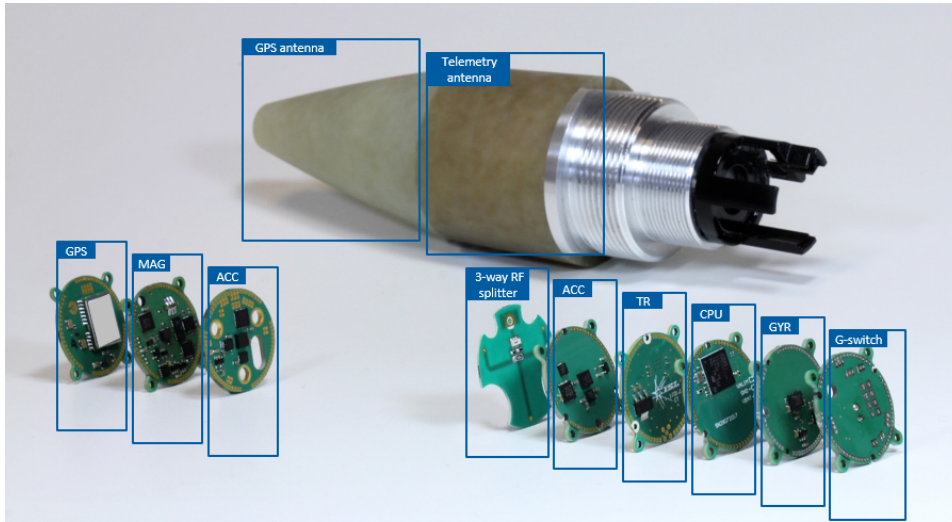


Figure 2.5.5: Instrumentation of an experimental 155 mm artillery shell from ISL. Sensors are located in the nose, thus being typically 20 cm away from the center of mass of the shell.

large (typically, the sensors are located approx. 20 cm from the center of mass in the direction of the nose). Furthermore, the sensors are not located right onto the shell symmetry axis, which correspond to small but non negligible *transverse* components in  $r$ . This is due to mechanical tolerances and uncertainties in the exact location of the sensors in the shell payload case. In turn, the high spin rate has a tremendous effect even for small such transverse shift in (2.5.2). This effect is clearly visible in Figure 2.5.6 in the case of a 155 mm shell. The shift in sensors location is larger than in the case of a Basic Finner, due to the extended length of the shell. The effect is mainly due to the high values of the spin rate, and is thus negligible on low spin rate projectiles such as Basic Finner. In the case of a Basic Finner, experimental measurements are similar to the simulation feedback, even though the location of the sensors is still shifted from the center of mass of the shell.

The analysis in the case of the 155 mm shell can be pursued as follows. According to (2.5.2), the factors that can cause fictitious forces are listed in Table 2.5.1, along with their typical values. In turn, the various disturbance terms appearing in (2.5.2) are listed by descending order of magnitude in Table 2.5.2. It is worth mentioning that the term  $r_1 p q + r_1 \dot{r}$  is actually much smaller than its constituting factors because, as can be seen in the last part of the rotational dynamics (2.4.5), one has that

$$I_t \gg I_l \text{ implies that } \dot{r} \approx -p q$$

This term is not negligible but it has the same frequency content as  $Y_{acc0}$ .

Then, it appears that the dominant fictitious force is  $-r_2 p^2$  and that it acts as a (slowly drifting) bias on the 3-axis Accelerometer. The « frequency content » column in Table 2.5.2 describes the oscillating contribution of each term ( $q$  and  $r$  obeying (2.4.4) and (2.4.5), respectively, and  $p$  being almost linearly damped according to (2.4.3)). This drifting bias is visible in Figure 2.5.6 (compare bottom-left and -right plots). Interestingly the bias is very large but it does not alter the frequency content of the 3-axis Accelerometer signals. This point will be instrumental in Chapter 3.

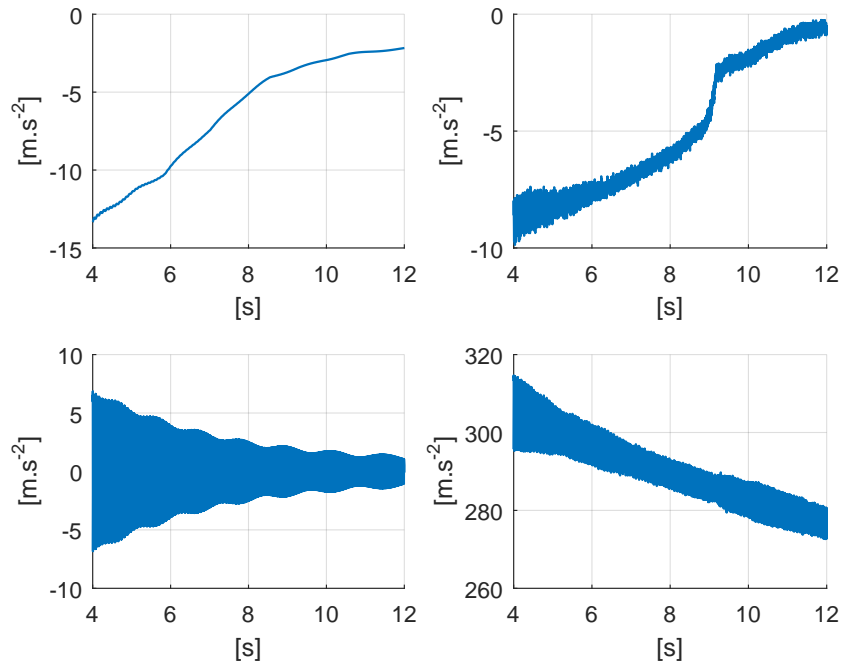


Figure 2.5.6: Values of longitudinal and transverse 3-axis Accelerometer signals: simulation (left), experimental (right).

Long. shift $r_1$ (m)	Trans. shift $r_2, r_3$ (m)	$p$ (rad.s <sup>-1</sup> )	$q, r$ (rad.s <sup>-1</sup> )
$10^{-1}$	$10^{-4}$	$10^3$	$10^1$

Table 2.5.1: Root causes of fictitious forces in 155 mm gyro stabilized projectiles.

Expression	Range of value (m.s <sup>-2</sup> )	Frequency content
$Y_{acc0}$	$10^1 \rightarrow 10^0$	$p, p - \omega_n, p - \omega_p$
$-r_2 p^2$	$10^2$	None
$r_1(pq + \dot{r})$	$10^1 \rightarrow 10^0$	$p, p - \omega_n, p - \omega_p$
$r_3 q r$	$10^{-2}$	Interfer. <sup>a</sup> of $p, p - \omega_n, p - \omega_p$
$-r_2 r^2$	$10^{-2}$	Interfer. of $p, p - \omega_n, p - \omega_p$
$-r_3 \dot{p}$	$10^{-3}$	None

Table 2.5.2: Signal at the center of mass and fictitious forces in one transverse accelerometer in a 155 mm gyro-stabilized projectile.

<sup>a</sup>wave interference: any  $a \pm b$  where  $a$  and  $b$  are picked from the given list.

## 2.6 Preliminary estimation of the angular velocity around main axis

As already noted, the symmetric nature of the shell implies the cancellation of the bilinear term  $q r$  in (2.4.3) so that that the equation (2.4.3) governing  $p$  is almost independent on the other angular rates  $q$  and  $r$ .

The spin rate  $p$  thus has a practically autonomous dynamics with almost linear damping. On the other hand, the transverse components  $q, r$  of the angular rate are linked to the attack and sideslip angles and follows a damped oscillator dynamics similar to Equation (2.4.7).

The shell is equipped with a dummy gyrometer, which can not be exploited for the various reasons mentioned in Chapter 1. It can be seen on Figure 2.5.5. We have explored various options to replace it. A two direction measurement method (clearly out of the scope of the thesis) is detailed in [38], and this particular topic has been studied also in the literature (see e.g. [25, 63, 83, 65, 13]). For the shells considered in the thesis, a simpler approach can be used, by considering that the angular velocity  $(p, q, r)$  is actually close to  $(p, 0, 0)$ .

Thankfully, such an estimation is easy, as the spin rate is the fastest frequency of both transverse accelerometers and transverse magnetometers. A frequency detection methods works well. Adding a physical model of its dynamics (relying mostly on rolling moment and roll-damping moment) could be useful, but is not necessary. In short, an extended Kalman filter with a model  $\ddot{p} = 0$  yields satisfying results. Figure 2.6.1a shows results on simu-

lation data, while Figure 2.6.1b shows experimental results. For the latter, the first estimation features outliers related to magnetometer measurement outliers. This is readily solved with a complex argument calculation method more robust to outliers (see Appendix B.1.)

## 2.7 Shooting range and external instrumentation

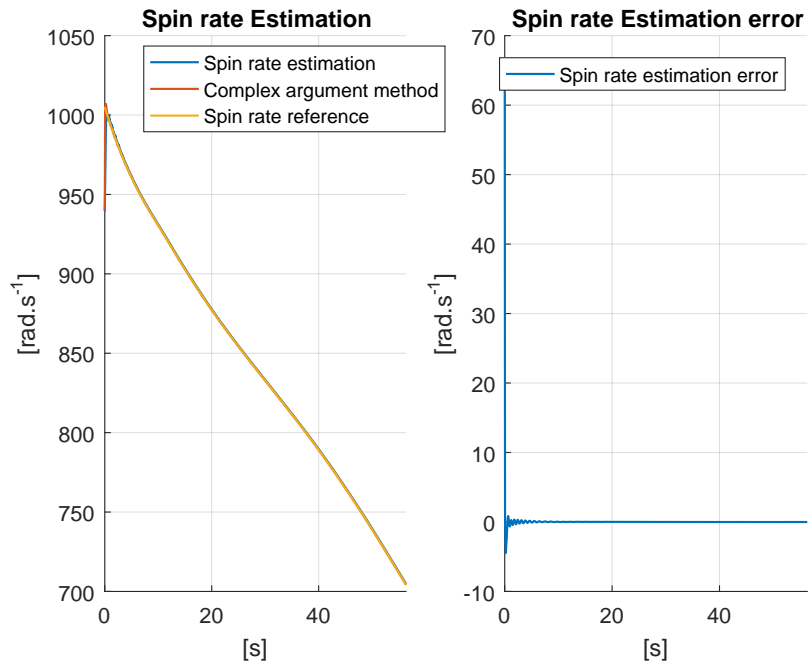
The shells are fired on the shooting range shown in Figure 2.7.1a. The setup of the shooting range is detailed in Figure 2.7.1b. This pictorial view illustrates the roles of the ground based position radar (Synthetic-aperture radar, Sarah radar) used to *a posteriori* reconstruct the trajectory of the shell. The ground based position radar can also be used to reconstruct the translational velocity of the shell. The Weibel Radar is a Doppler radar used to measure the initial velocity only. The ISL telemetry system corresponds to the embedded system presented in Section 2.5 combined with ground receivers and antennas.

## 2.8 Testcases considered in the thesis

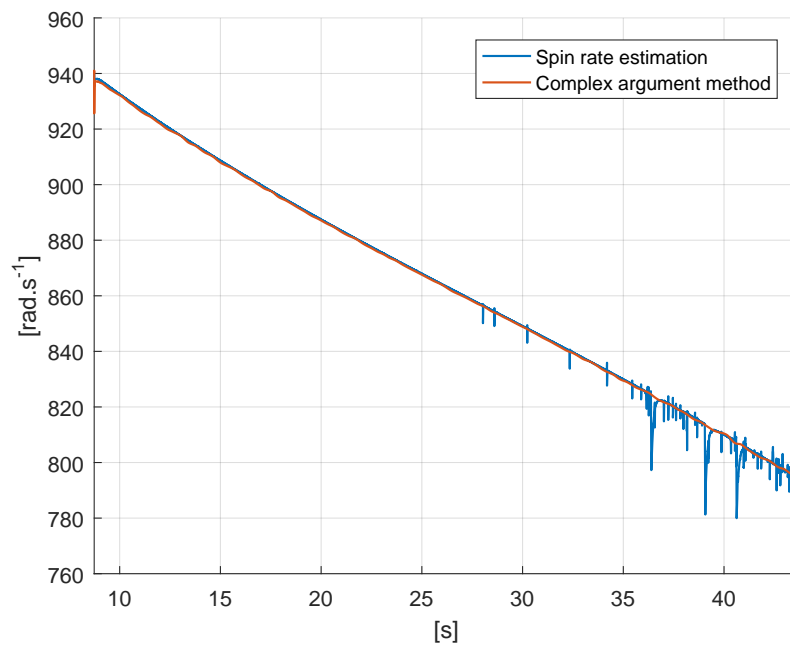
The four testcases listed in Table 2.8.1 will be considered in the manuscript. The reported time windows are chosen under the form of a single time interval avoiding instants when most data corruption issues take place. These issues are sensor saturation, data transmission losses and radar measurement failures. Some outliers remain in the considered data though, to keep the time windows relatively long.

Ref	Projectile	Data type	Init. elevation angle (mil)	Init. vel. (m.s <sup>-1</sup> )	Max. spin rate (rad.s <sup>-1</sup> )	Duration (s)	Time window (s)
1	155 mm	Simulation	800	493	1005	56	[0, 56]
2	155 mm	Experimental	800	493	≈ 1000	49	[8.7, 43]
3	Basic Finner	Simulation	0.2	450	0	1	[0, 1]

Table 2.8.1: Data sets considered in this thesis.



(a) Estimation of spin rate for a 155 mm shell [simulation results].

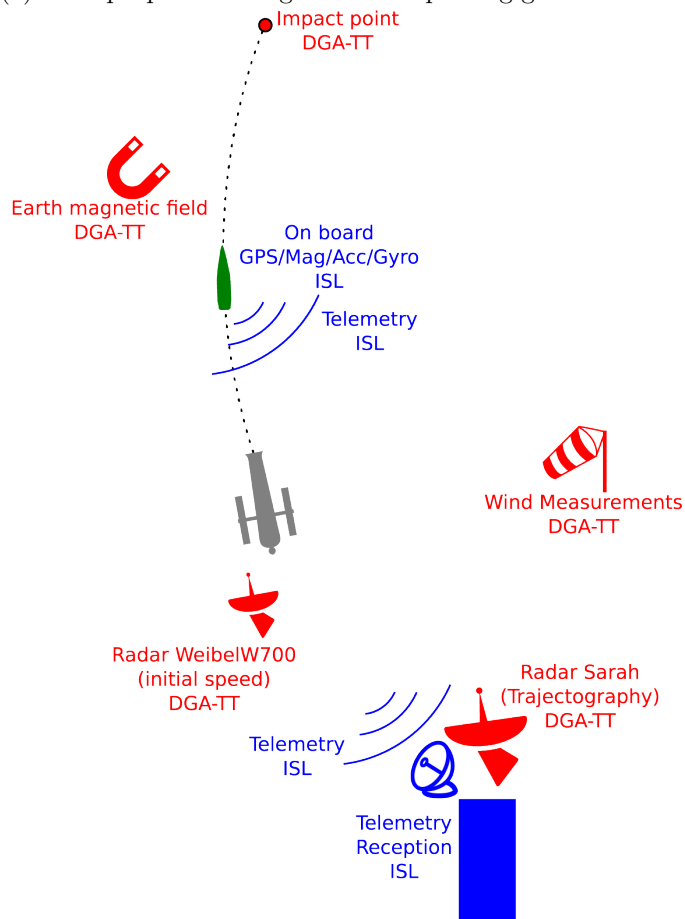


(b) Estimation of spin rate for a 155 mm shell [experimental results].

Figure 2.6.1: Estimation of spin rate.



(a) Multipurpose free-flight outdoor proving ground at ISL.



(b) Setup of the proving ground.

Figure 2.7.1: Proving ground.



## Chapitre 3 - Résumé

Dans ce chapitre, on présente une méthode pour estimer la vitesse par rapport à l'air d'une munition, à l'aide du contenu fréquentiel des accéléromètres, évoqué dans le chapitre précédent. Le mouvement oscillatoire de précession et de nutation de la munition est caractérisé grâce à la modélisation évoquée précédemment. On détaille ensuite les méthodes de détection de fréquence utilisées pour extraire ces différentes fréquences des signaux d'accéléromètres, puis on présente un observateur utilisant ces mesures de fréquences pour estimer la vitesse de la munition. Une preuve de convergence est donnée, et des résultats expérimentaux sont présentés.



## Chapter 3

# Frequency analysis of the epicyclic rotational dynamics

### 3.1 Problem statement

As will be discussed, a way to estimate the velocity w.r.t. the air of a shell submitted to known aerodynamic moments is through the analysis of the frequencies of its Pitching and Yawing oscillations. The method detailed in this chapter is instrumental for using the aerodynamic model of a gun-fired ammunition, since estimating forces requires the knowledge of its velocity with respect to the air. In our case, this is used for attitude estimation purposes as exposed in Figure 3.1.1.

As discussed in Chapter 2, the absolute values of the sensors are biased. In particular, the 3-axis Accelerometer is strongly biased by the fictitious forces. However, the bias does not impact the frequency content of the measurements. For this reason the various frequency detection methods employed in this chapter are in fact insensitive to the effects of fictitious forces. Compared to other methods aiming at reconstructing the velocity w.r.t. the air, frequency detection reveals to be more reliable and accurate than more direct methods using the absolute values of the sensors such as inversion of models from accelerometric measurements.

From the description of the rotational dynamics in Section 2.4.2, the Pitching and Yawing oscillations define an epicyclic motion (depicted by Figure 2.4.1 where the locus of the complex yaw  $\xi$  from Equation (2.4.8) is shown). The frequencies of the yawing and pitching motions are visible on the measurements of the strapdown inertial sensors (although one needs to discriminate them from the spin rate oscillation beforehand, as will be explained (see Equation 2.4.7 and Table 2.5.2 for the frequency content of transverse accelerometers).

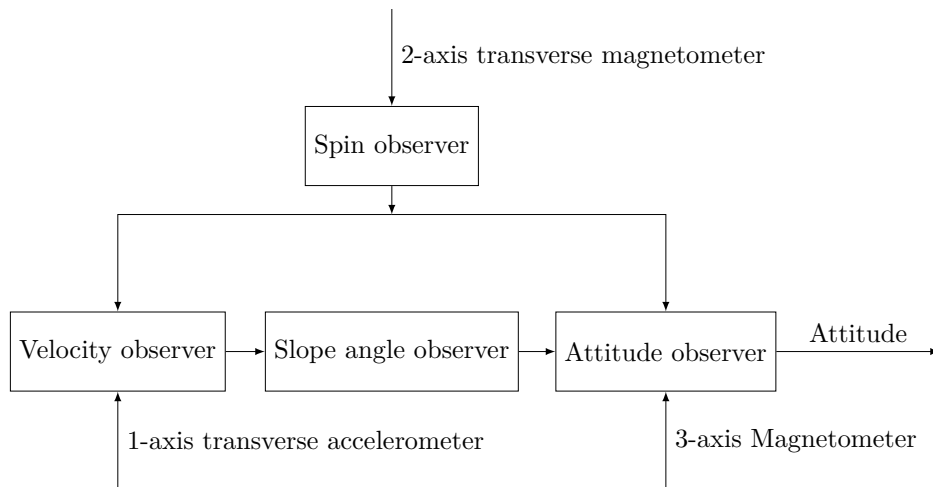


Figure 3.1.1: Considered cascaded estimation of the attitude. The velocity information is of interest to estimate the slope and incidence of the shell.

As it will be explained in Section 3.2, those frequencies carry information on the Mach number, the spin rate of the shell and its aerodynamics coefficients. The methodology we advocate is pictured in Figure 3.1.2. However, the frequency information can be more or less difficult to extract, especially in the trans-sonic region. For this reason, the methodology combines a frequency detection algorithm and a state observer playing the role of filter.

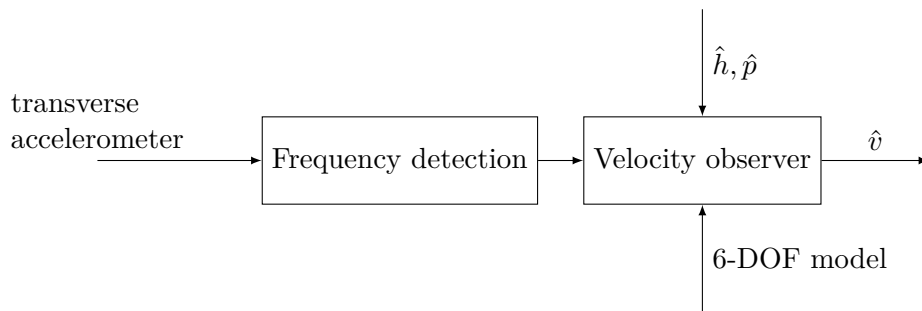


Figure 3.1.2: Method to estimate the velocity of the shell.

### 3.2 Frequency content of the embedded inertial measurements

Some lengthy calculations allow one to determine the frequencies appearing in the solution of the rotational dynamics (2.4.7). These frequencies are the

results of some wave interferences<sup>1</sup> caused by the nutation, precession and spin rotations.

The nutation and precession frequencies,  $\omega_n$  and  $\omega_p < \omega_n$  respectively, have symmetrical expressions

$$(3.2.1) \quad \omega_n = \frac{pI_l}{2I_t} + \frac{v}{2D}(P_1^2 + P_2^2)^{\frac{1}{4}} \cos \left[ \frac{1}{2} \arctan \left( \frac{P_2}{P_1} \right) \right]$$

$$(3.2.2) \quad \omega_p = \frac{pI_l}{2I_t} - \frac{v}{2D}(P_1^2 + P_2^2)^{\frac{1}{4}} \cos \left[ \frac{1}{2} \arctan \left( \frac{P_2}{P_1} \right) \right]$$

where

$$\begin{aligned} P_1(v, h, p) &= a_1(v, h)^2 - b_1(v, p)^2 - 4a_2(v, h) \\ P_2(v, h, p) &= 4b_2(v, h, p) - 2a_1(v, h)b_1(v, h) \end{aligned}$$

with

$$\begin{aligned} a_1(v, h) &= -B_M C_{Mq} + B_F(C_{L\alpha} - C_D) \\ a_2(v, h) &= -B_M C_{M\alpha} \\ b_1(v, p) &= \frac{p}{v} D \frac{I_l}{I_t} \\ b_2(v, h, p) &= b_1(B_F C_{L\alpha} - B_M C_{mag-m} \frac{I_t}{I_l}) \\ B_F(h) &= \frac{\rho_a(h)SD}{2m}, \quad B_M(h) = \frac{\rho_a(h)SD^3}{2I_t} \end{aligned}$$

### 3.3 Instantaneous frequency detection: measuring varying frequencies

#### 3.3.1 Definition of the frequency of interest

As discussed in Section 2.5, the transverse strapdown accelerometers measure a projection of the aerodynamic forces in the body frame. Their signal is thus proportional to the incidence angles of the shell. Typical measurements are reported in Figure 3.3.1. According to (2.4.10), these angles oscillate with frequencies

$$\{p - \omega_n, p - \omega_p, p\}$$

where  $\omega_n$  and  $\omega_p$  are the precession and nutation frequencies (referred to as « epicyclic frequencies ») defined in eqs. (3.2.1) and (3.2.2).

---

<sup>1</sup>(recall from Chapter 2.) wave interference between  $a$  and  $b$  are any  $a \pm b$  ; here, only  $p, p - \omega_n$  and  $p - \omega_p$  show in the signal due to the peculiar expression of the accelerometer feedback

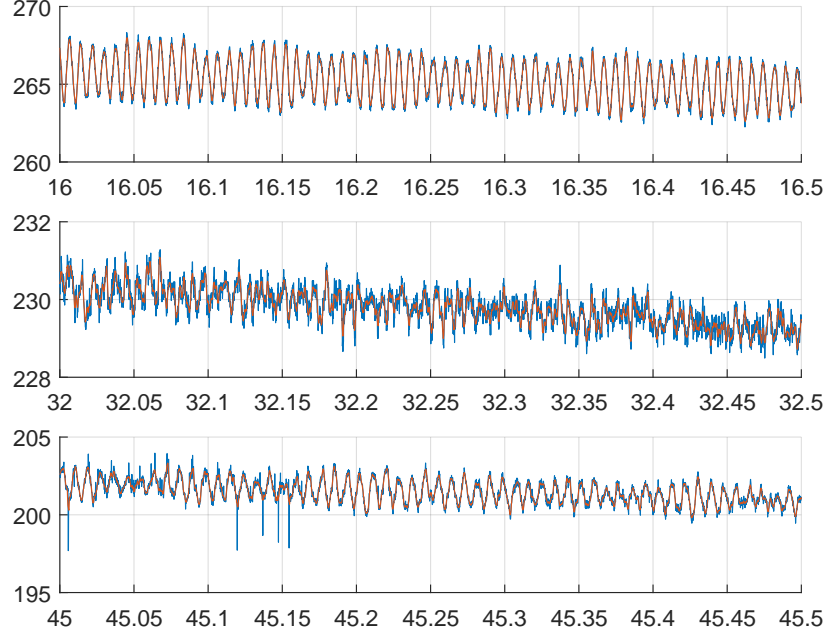


Figure 3.3.1: Examples of signals from one of the transverse accelerometers. Three distinct time windows are reported. [experimental results]. Signals with and without noise filtering are shown.

In the following, we define our « measurement »  $\omega_{\text{meas}}$  as

$$(3.3.1) \quad \omega_{\text{meas}} = \omega_n - \frac{p I_l}{2 I_t} = \frac{p I_l}{2 I_t} - \omega_p = \frac{\omega_n - \omega_p}{2}$$

There are a number of possible choices to isolate the velocity-dependent factor appearing in the equations. Because  $p$  is easy to estimate as discussed in Section 2.6, a simple strategy is to simply subtract it from the detected frequencies.

Figure 3.3.2 shows the frequency content of a transverse accelerometer, and the epicyclic frequencies themselves, over the course of a typical ballistic flight. The nutation frequency  $\omega_n$ , faster than the precession  $\omega_p$ , is both easier to measure on short time windows (because a larger number of its periods can be observed over a given time window) and to distinguish from the spin rate in the accelerometer feedback (see Figure 3.3.2-right). For these reasons, we now focus on detecting the nutation frequency  $\omega_n$ .

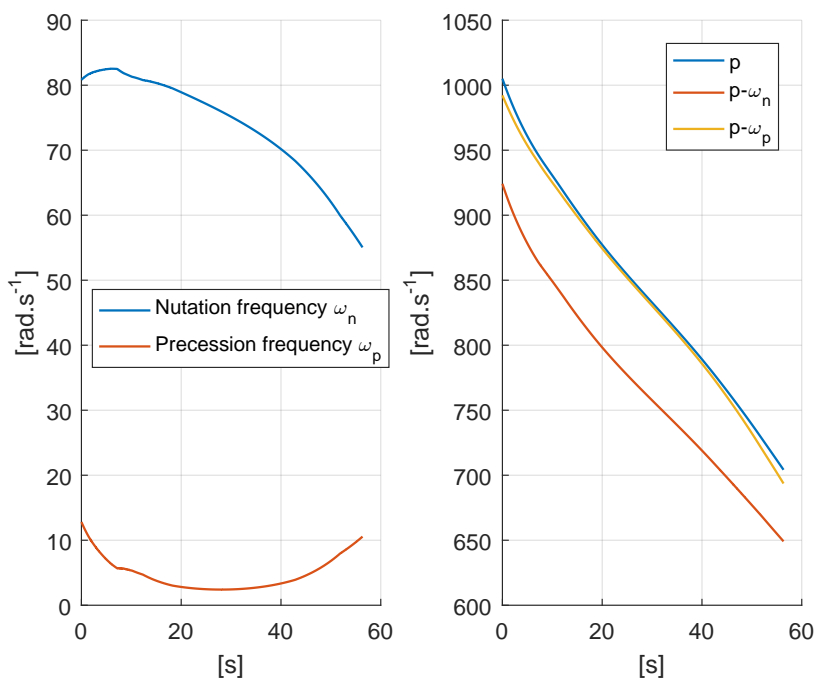


Figure 3.3.2: Theoretical frequencies of the epicyclic motion  $\omega_p < \omega_n$  (left) and theoretical frequencies  $p - \omega_n < p - \omega_p < p$  contained in the signal from any of the transverse accelerometers (right) [simulation results for a 155 mm shell].

### 3.3.2 Envelope filter and FFT

A common practice to estimate the frequency of a monochromatic signal or a multisinusoidal signal is to use Fast Fourier Transform (FFT) over sliding windows. This state-of-the-art technique is at the heart of the *periodogram* technique [69] and is often employed in various applicative situations.

As previously discussed, the sensor signals contains the frequency  $p - \omega_n$ , while our interest lies in detecting  $\omega_n$ . A solution is to treat the signal directly, detect  $p - \omega_n$  as one of peaks of the FFT, and deduce  $\omega_n$  by subtracting the known value of  $p$ . This is possible, but is not the best option because, as illustrated in Figure 3.3.2 and Figure 3.3.5, the frequencies peaks  $p - \omega_n < p - \omega_p < p$  of the signal are relatively close, and the accuracy of the obtained estimate may not be very high.

A useful alternative is to consider the envelope of the signal, which rules out the spin rate present in the signal. The envelope is calculated using a standard numerical routine (e.g. an envelope follower filter), or alternatively using the Hilbert transform.

An envelope follower filter is nonlinear and its simplest form implements a low-pass filter of (4 times) the square of the signal to be treated or implements the discrete version of a diode detector [45]:

$$\dot{y} = \begin{cases} -\frac{x}{\tau} & \text{if } x > s \\ \frac{ks-x}{\tau} & \text{otherwise} \end{cases}$$

where  $k$  and  $\tau$  defines the properties of the filter.

The method employing the Hilbert transform of the signal  $y$  considers the complex-valued signal

$$s(t) = y(t) + iH(y)(t)$$

with

$$H(y) = \frac{1}{\pi} \int_{-\infty}^{+\infty} \frac{y(x)}{t-x} dx$$

where the integral is evaluated as a Cauchy principal value. This shows, by a convolution argument, that  $H(y)$  the Hilbert transform can be computed as the product of the Fourier transform of  $y$  with the function  $-i \operatorname{sign}(x)$ . The envelope is simply the modulus of  $s(t)$ .

To minimize aliasing effect and leakage in the FFT (mostly due to the number of cycles in the time window being fractional), a Han window is applied to the envelope. Finally, to improve the resolution of the FFT, zero-padding is applied. Then the frequency estimate is found as one of the peaks of the FFT, and is computed as the maximum of a local polynomial fit for improved accuracy. The result of this procedure is the estimator  $f_1$ .

### 3.3.3 Detecting peaks in the autocorrelation function

Further, an alternative estimator has been designed. This estimate is based on the pseudo periods of successive peaks in the envelope of the autocorrelation function of the signal.

Prior to calculating the autocorrelation function, the raw signal is de-biased and its observed drift is canceled by subtracting a best-fit affine time function. Then, the autocorrelation function is numerically calculated over a linearly-spaced grid of lags. Then, the envelope of this function is calculated. At this stage, reported in Figure 3.3.3, a pseudo periodic signal is found. It is smoothed to ease the determination of peaks, which are computed as the maximum of a local polynomial fit (as previously). The sequence of peaks is then fit to an affine function of the lag. The distances between the first three consecutive peaks (the most visible) provide another estimate  $f_2$ . The steps above are pictured in Figure 3.3.4.

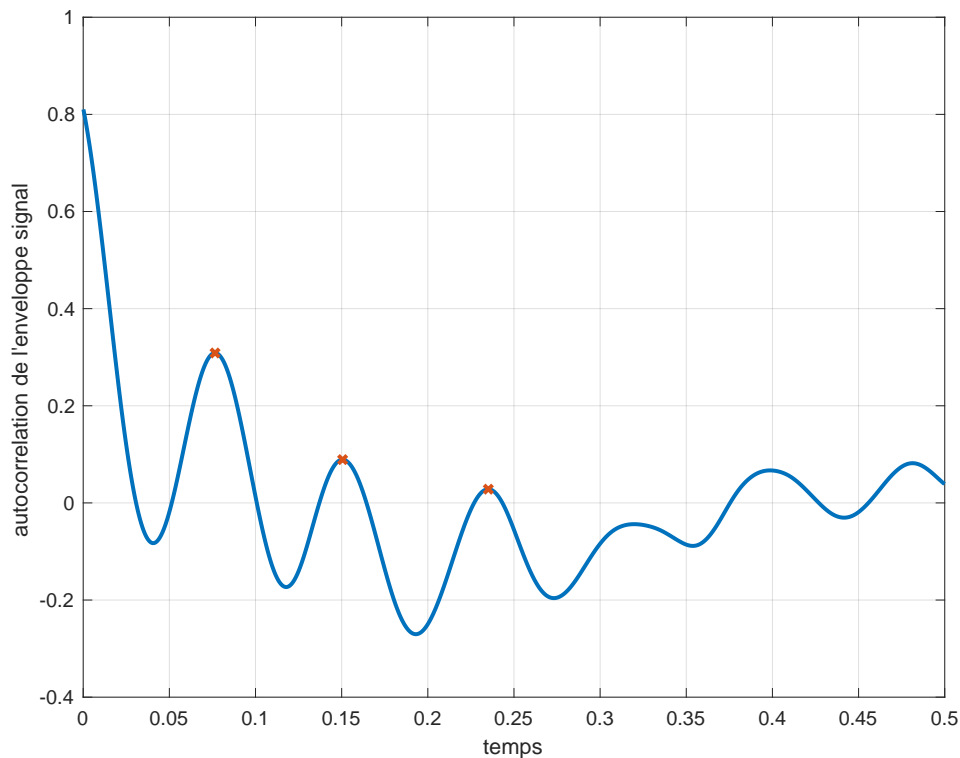


Figure 3.3.3: Envelope of autocorrelation function [experimental results].

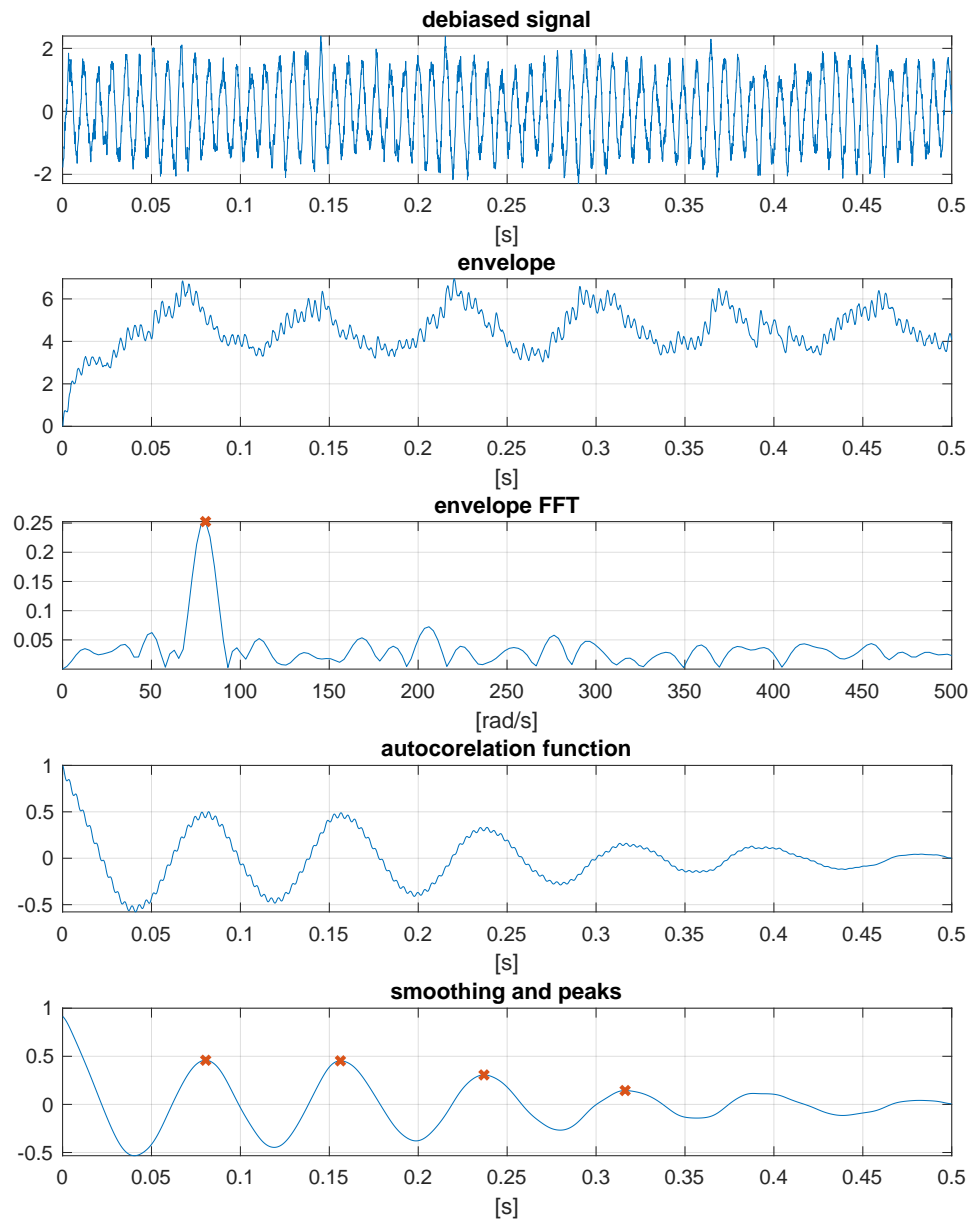


Figure 3.3.4: Treatment steps [experimental results].

### 3.3.4 Frequency detection using super-resolution

In theory FFT based methods directly employed on the signal are not really ideally suited in the case considered here. The main culprit is that FFT is only effective in cases where a relatively large number of periods can be used to estimate the frequency. If this assumption fails, then numerous malicious effects appear such as spectral aliasing, and frequency leak [69].

Large time windows can not be employed here, because the oscillations of the aerodynamics forces are decaying over time (see Figure 2.4.1). Employing a large window violates the assumption that the signal has constant magnitude, which is implicitly required for the FFT technique to produce quality results. Therefore some traded-off must be made.

Instead, we can use a super-resolution technique. In a nutshell, this technique is optimization-based (in the time domain). It seeks the frequencies of a multisinusoidal signal as the solution of a best-fit problem. Various implementations exist, from the classic Prony based methods (MUSIC [44]) to more recent total-variation norm minimization methods [34, 33]. On top of improving resolution, the methods have proven capabilities of outlier rejection even with high noise/signal ratios. To work effectively, super-resolution methods require that the numbers of frequencies to be located in the signal can be known in advance. This is precisely the case in our application, as we have seen it in Section 3.2. On experimental data, we use the knowledge of every cross-frequency wave interference added by fictitious forces, as described in Table 2.5.2.

Super-resolution methods can deal with short time windows, typically half a period of the lowest frequency to be detected is enough. This is a helpful feature in our case. We report in Figure 3.3.5, a typical example where the spin, and linear combinations with nutation and precession frequencies are detected as the sharp peaks of the spectrum obtained from MUSIC.

Assuming that the frequency-detection algorithm discussed above has been implemented<sup>2</sup>, its output is noted  $f_3$  and should ideally be equal to the sought-after angular frequency

Even with relatively large amounts of noise, this output is relatively reliable. This point is easy to check in simulations. It is not noise-free, as the output of the super-resolution algorithm is by definition lying on a (fine) grid of possible values.

In practice, treating experimental data can be more troublesome, this point will be discussed in Chapter 6. More can be said about that, see Appendix B.2.

### 3.3.5 Filtering the estimates

Careful tuning of the various parameters of the estimation procedures described above allows to determine successive values for  $f_1$ ,  $f_2$ ,  $f_3$ . On occasions, each estimator may fail to provide a dependable value. To circumvent this, some filtering of this signal must be performed. This is the purpose of

---

<sup>2</sup>for application we will use the PMUSIC implementation in Matlab.

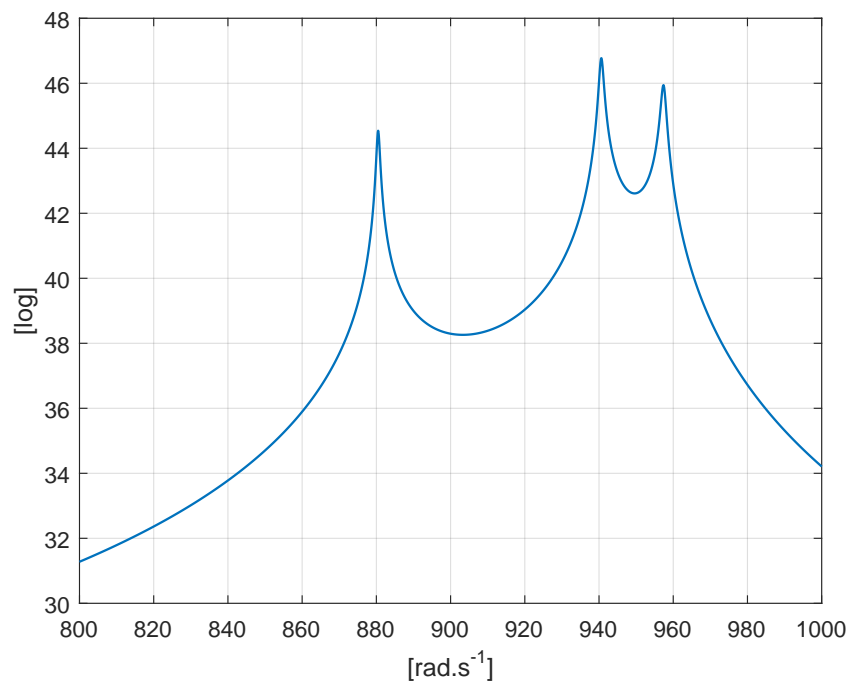


Figure 3.3.5: Detection of the frequencies  $p - \omega_n < p - \omega_p < p$  contained in the signal from one of the transverse accelerometers (simulation results on 155 mm shell).

the state observer used in Chapter 6.

## 3.4 Design of an observer for the velocity from frequency measurements

### 3.4.1 System dynamics and output map

To filter the measurement of the velocity w.r.t. the airflow  $v$ , we design a state observer, relying on the dynamics below

$$(3.4.1) \quad \dot{v} = \frac{-\rho_a(h)SC_D(v, h)v^2}{2M} - g \sin(\theta)$$

$$(3.4.2) \quad y = \frac{v}{2D} (P_1(v, h, p)^2 + P_2(v, h, p)^2)^{\frac{1}{4}} \cos \left[ \frac{1}{2} \arctan \left( \frac{P_2(v, h, p)}{P_1(v, h, p)} \right) \right]$$

For now, we assume that two of the variables appearing in the right-hand sides above are in fact known in advance, at least to a certain degree of accuracy<sup>3</sup>: the planned altitude  $h(t)$  and slope angle of the trajectory  $\theta(t)$ , and the real spin rate  $p(t)$  are known. This allows us to rewrite the dynamics as a single-state time-varying nonlinear dynamics

$$(3.4.3) \quad \dot{v}(t) \triangleq f(v, t)$$

$$(3.4.4) \quad y(t) \triangleq g(v, t)$$

Various plots of the mappings  $f$  and  $g$  are reported in Figure 3.4.1 and Figure 3.4.2.

Observer design for this nonlinear dynamics(3.4.3)-(3.4.4) seems, at first, a routine problem. The main difficulty here is that  $g$  in (3.4.4) is not one-to-one. In fact, a general property stemming from the behavior of aerodynamic drag-induced effects near Mach 1.0 (see discussion in §2.4.1), is that for any given  $t$ ,  $v \mapsto \frac{\partial g}{\partial v}(v, t)$  has a fixed number  $N$  of zeros (at least 2), that we note  $m_i(t)$  with

$$m_1(t) < \dots < m_N(t)$$

To clarify, those zeros are linked to specific fixed Mach values. They represent time-varying critical velocities, because said velocities are linked to Mach values by the sound velocity at the altitude  $h(t)$  reached at time  $t$ , via the corresponding air density.

This fact is illustrated in Figure 3.4.2, with  $N = 2$  for a typical ballistic trajectory of a 155 mm shell. We may call this the *non-bijectionality of the*

---

<sup>3</sup>in practice it can be noted that the variables can be defined from reference histories provided that they are well synchronized, which is easily done by detecting gun fire from any of the embedded signal, e.g. any of the accelerometers.

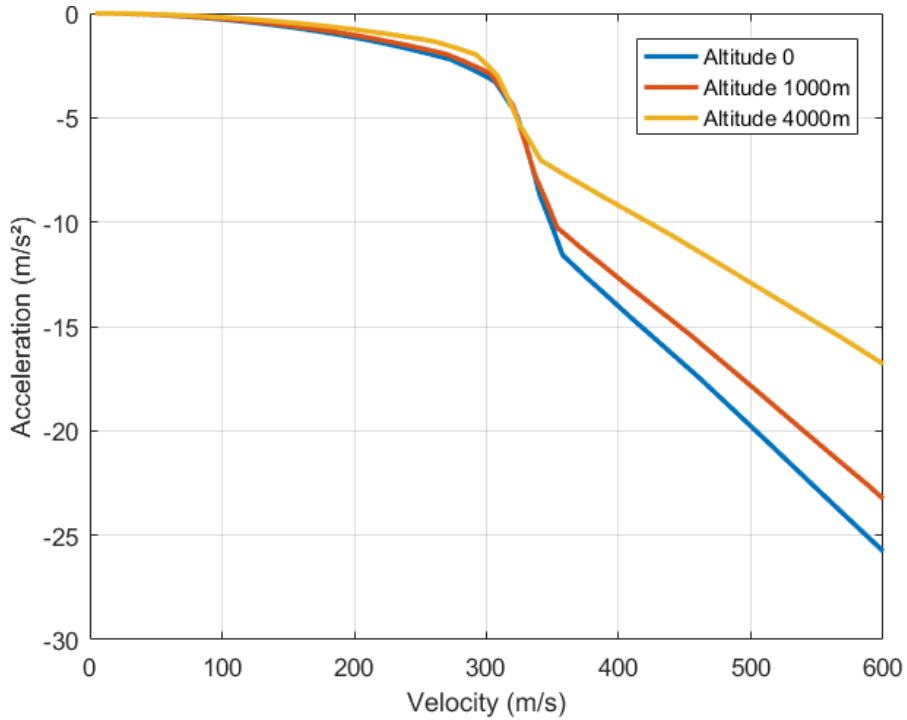


Figure 3.4.1: Representation of  $f(v, t)$  (for a fixed  $t$ , at various altitudes).

*frequency-velocity mapping in transonic regime.* Finally, one can also note that  $f$  becomes step in the same regime (see Figure 3.4.1). However, it remains monotonic w.r.t.  $v$  at all times. Some (tedious) analytical study reveals that  $\frac{\partial C_D}{\partial v}$  remains small enough, for all  $v$  and  $t$  of interest in this study, so that  $\frac{\partial f}{\partial v}$  stays strictly negative and bounded<sup>4</sup>.

For a given trajectory, traveling through the atmosphere, the  $m_i$  are time-varying because the extremum points depend on the Mach number, and thus on the air density in addition to the velocity. For the rest of the analysis, we consider that the  $m_i$  are continuous and differentiable functions of the time (*de facto*, they are continuous and differentiable functions of the air density and the spin rate, which vary continuously over time), without any further assumption on the aerodynamic coefficients.

For all applications considered below, i.e. speed and time ranges, the mapping  $f$  is a contraction in the sense of [57] as

$$\frac{\partial f}{\partial v} < -\gamma < 0$$

for some  $\gamma > 0$ .

<sup>4</sup>Establishing this could be more involved for other shells, e.g. reentry vehicles for which trajectories cover much wider velocity and time ranges.

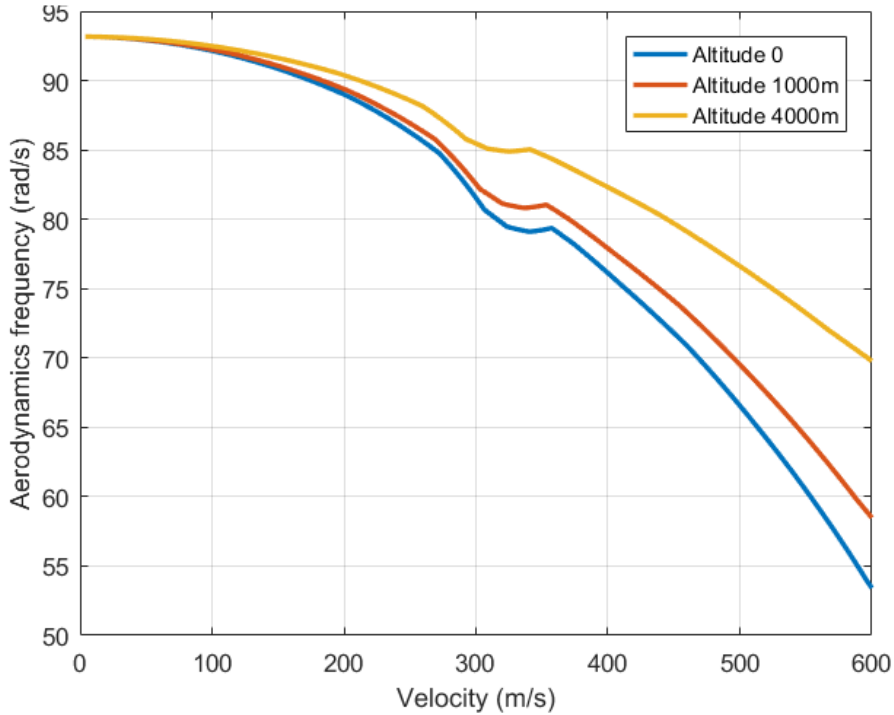


Figure 3.4.2: Representation of  $g(v, t)$  (for a fixed  $t$ , at various altitudes).

### 3.4.2 Observer design

The observer is quite easy to design, using the fact that  $f$  defines a contractive mapping. However, the exponential convergence stemming from this property is not sufficient for practical application of velocity estimation (note that the total flight time is short). To speed-up the convergence, we make an active usage of the measurement  $y$ .

As discussed earlier, the output mapping is not one-to-one. Locally, it is monotonic, but since the estimate from the observer is the only way to guess whether the mapping is currently increasing or decreasing, there is no straightforward condition to determine the sign of the observer gain. This problem is relatively frequent in control system theory, see e.g. [14] and references therein.

What we propose is a gain-switching observer, following a classic approach [2, 22], where the gain is a function of the current estimate. To guarantee exponential convergence, we consider the squared error as candidate Lyapunov function and design the gain so that it is always decreasing. This is achieved by shutting-down the gain in certain areas near specific Mach numbers, where the derivative of  $g$  w.r.t. the velocity changes sign. The on-off times are tailored according to the properties of the aerodynamics

model (upper and lower Lipschitz constants).

### 3.4.3 Convergence analysis

Let  $k$  and  $\epsilon$  be two strictly positive numbers. Consider the gain

$$(3.4.5) \quad K(\hat{v}, t) \triangleq \chi(\hat{v}, t) k \frac{\partial g}{\partial v}(\hat{v}, t)$$

with

$$(3.4.6) \quad \chi(v, t) = \begin{cases} 0 & \text{if } v \in \bigcup_{i=1}^N m_i(t) - \epsilon, m_i(t) + \epsilon \\ 1 & \text{otherwise} \end{cases}$$

Then, one can state the following result:

**Theorem 1.** *Consider the state dynamics (3.4.3). Let us assume that there exists  $M > 0$  such that  $|v(0) - \hat{v}(0)| < M$ , and that  $\hat{v}(0) > m_N(0)$  and  $v(0) > m_N(0)$ . Then, there exists  $\epsilon$  and  $k_M$  such that the observer  $\hat{v}$  defined by  $\dot{\hat{v}} = f(\hat{v}, t) + K(\hat{v}, t)(y - g(\hat{v}, t))$  and (3.4.5)-(3.4.6) produces an estimation error  $|v - \hat{v}|$  which converges exponentially to 0.*

*Proof.* Let  $\delta$  and  $\epsilon$  be two strictly positive numbers such that  $\hat{v}(0) > m_N(0) + \epsilon$  and  $v(0) > m_N(0) + \epsilon + \delta$  and  $k_M > 0$  satisfies

$$(3.4.7) \quad k_M > \frac{1}{\zeta_1} \frac{m}{\ell}$$

and

$$(3.4.8) \quad k_M > \frac{-1}{\zeta_2^2 T} \log \left( \frac{\epsilon}{M} \right)$$

where the following constants are defined (they depend solely on the trajectory under consideration)

$$\begin{aligned} T &\triangleq \inf \{t \geq 0, v(t) \leq m_N(t) + \epsilon + \delta\} \\ m &\triangleq \max \{m_N(t), t \in [0, T]\} + \max \{-f(m_N(t) + \epsilon, t), t \in [0, T]\} \\ \ell &\triangleq \min \{|g(m_N(t) + \epsilon + \delta) - g(m_N(t) + \epsilon, t)|, t \in [0, T]\} \\ \zeta_1 &\triangleq \min_{0 \leq t \leq T, m_N(t) + \epsilon \leq v \leq +\infty} \left( \left| \frac{\partial g}{\partial v}(v, t) \right| \right) \\ \zeta_2 &\triangleq \max_{0 \leq t \leq T, m_N(t) + \epsilon \leq v \leq +\infty} \left( \left| \frac{\partial g}{\partial v}(v, t) \right| \right) \end{aligned}$$

Note that  $\zeta_1$  and  $\zeta_2$  are properly defined as long as we extend our mapping of the aerodynamic coefficients by a continuous and differentiable saturation to the end of our mapping. In practical,  $v$  stays bounded in a

finite-flight (the shell has finite energy and the altitude has to remain positive), and  $\hat{v}$ , even though having a different dynamics, only gets closer to  $v$  as  $t$  increases, bounding him as well.

Set  $V = \frac{1}{2}(v - \hat{v})^2$  as a candidate Lyapunov function. It is strictly positive, and we will show its time derivative is strictly negative along the system trajectory for any initial conditions satisfying the assumptions of the statement.

By the mean-value theorem applied to  $f$  and  $g$ , separately, for any  $t \geq 0$ , there exists  $a_t$  and  $b_t$  in between  $v$  and  $\hat{v}$  such that :

$$\dot{V} = (v - \hat{v})^2 \left( \frac{\partial f}{\partial v}(a_t, t) - K(\hat{v}, t) \frac{\partial g}{\partial v}(b_t, t) \right)$$

which expands as

$$\dot{V} = 2V \left( \frac{\partial f}{\partial v}(a_t, t) - \chi(\hat{v}, t) k_M \frac{\partial g}{\partial v}(\hat{v}, t) \frac{\partial g}{\partial v}(b_t, t) \right)$$

As we know it,  $\frac{\partial f}{\partial v} < -\gamma < 0$ . On the other hand the sign of the second factor is less obvious. In fact, from the definition of the indicator function (3.4.6), if  $\chi(\hat{v}, t)$  is non-zero, then  $\frac{\partial g}{\partial v}(\hat{v}, t)$  and  $\frac{\partial g}{\partial v}(b_t, t)$  are of the same sign for any  $b_t$  in between  $v$  and  $\hat{v}$ . We will show firsthand that this is the case for  $t \in [0, T]$ , implying that  $\dot{V} < -2\gamma V$  on that domain, then we will show that this inequality also holds for  $t \geq T$  for a similar reason.

**Before time  $T$**  By definition, for  $t \in [0, T]$ ,  $v(t) \geq m_N(t) + \epsilon + \delta$ . Let us show that for  $t \in [0, T]$ ,  $\hat{v} \geq m_N(t) + \epsilon$ .

Given any  $t \in [0, T]$  such that  $\hat{v}(t) = m_N(t) + \epsilon$ , then  $\dot{\hat{v}}(t) = f(m_N(t) + \epsilon, t) + k_M \frac{\partial g}{\partial v}(m_N(t) + \epsilon, t)(g(v, t) - g(m_N(t) + \epsilon, t))$ .

We show, from (3.4.7), that in this case  $\dot{\hat{v}}(t) > m_N(t)$ . This quite easily leads to the fact that for  $t \in [0, T]$ ,  $\hat{v} \geq m_N(t) + \epsilon$ .

We thus concludes that for  $t \in [0, T]$ ,  $\chi(\hat{v}, t) = 1$ , and that

$$k_M \frac{\partial g}{\partial v}(\hat{v}, t) \frac{\partial g}{\partial v}(b_t, t) < 0$$

As a result,  $\dot{V} < -2\gamma V$  on  $[0, T]$ .

**After time  $T$**  Let us show that  $\dot{V}$  remains strictly less than  $-2\gamma V$  after time  $T$ .

Because of (3.4.8), one gets  $k_M > \frac{-1}{\zeta_2^2 T} \log \left( \frac{\epsilon}{|v(0) - \hat{v}(0)|} \right)$  and obviously  $\dot{V} < -2\zeta_2^2 k_M V$  on  $[0, T]$  by definition of  $\zeta_2$ , we get  $V(T) < V(0)e^{-2\zeta_2^2 k_M T} < V(0) \left( \frac{\epsilon}{|v(0) - \hat{v}(0)|} \right)^2$  which gives us  $|v(T) - \hat{v}(T)| < \epsilon$ .

Let us assume that there exists a minimal  $t_c > T$  where  $\dot{V} \geq -2\gamma V$ . For  $t \in [T, t_c[$ , we have  $\dot{V} < -2\gamma V$  and thus  $|v(t_c) - \hat{v}(t_c)| < \epsilon$ .

As a result, there are two (exclusive) alternatives : either  $\hat{v}(t_c)$  belongs to  $\bigcup_{i=1}^N ]m_i(t) - \epsilon, m_i(t) + \epsilon[$ , which nullifies  $\chi$  and sets the gain to zero ; or  $\hat{v}(t_c)$  does not, and then obviously  $\frac{\partial g}{\partial v}(v, t)$  is of the same sign as  $\frac{\partial g}{\partial v}(\hat{v}, t)$ , because  $|v(t_c) - \hat{v}(t_c)| < \epsilon$  and then neither of the  $m_i(t_c)$  can be between  $v(t_c)$  and  $\hat{v}(t_c)$  ; in that case  $k \frac{\partial g}{\partial v}(\hat{v}, t) \frac{\partial g}{\partial v}(b_t, t) < 0$ . Either way,  $\dot{V}(t_c) < 2\gamma V$ , which is a contradiction.

**Conclusion of the proof** In summary,  $V$  is a Lyapunov function for our observation system  $(v, \hat{v})$ . The convergence is exponential, as  $\dot{V} < -2\gamma V$  with  $\gamma > 0$ . This concludes the proof. □

## 3.5 Illustrative results

### 3.5.1 Reference velocity

A difficulty in treating experimental results is that no reliable reference for the velocity with respect to the airflow is available. Instead we use that velocity w.r.t. the local frame which is measured<sup>5</sup>, on the shooting range with the ground based position radar. The algebraic difference between the two variables is the wind velocity.

Interestingly, it is possible to determine the wind velocity at the instant when the shell reaches Mach 1 speed. Indeed, this time is obviously materialized in the longitudinal accelerometer feedback (due to the shock wave), as shown by Figure 2.5.6, and the altitude given by the ground based position radar makes us able to compute the velocity corresponding to Mach 1. In data set 2 (see Table 2.8.1), it is equal to 332 m/s, when the ground based position radar gives a local velocity of 317.8 m/s, implying a contribution of 14.2 m/s of the airflow. Of course, the contribution of the wind velocity onto the velocity is not constant because the orientations of both the shell and the wind are subject to change during the course of the flight. This however gives a good insight on the confidence interval around the local velocity in which the velocity with respect to the airflow might be located. This inter-

<sup>5</sup>its values are available *a posteriori*.

val can be corroborated with meteorological measurements, which are often available for experiments at the shooting range. Typically, a value from 0 to 15 m/s is not surprising at higher altitudes, even when there is no wind on the ground.<sup>6</sup>

Additionally, the estimate of the bias obtained near Mach 1 should be accounted for as a bias on the frequency estimated in Section 3.3.

Note that other model bias can be considered. Among those, a possibly dominant factor lies in the atmosphere model exposed in Section 2.2. However, such effects are small. An error in the ground temperature, resulting in an error in the air density, has an impact on the function linking the velocity to extracted frequencies. Typical resulting errors are showcased in Figure A.4.1 and Figure A.4.2.

### 3.5.2 Results

The observer proposed in this chapter has been tested on experimental data. For the illustration given here, a filtered fusion of frequency detection methods is used (it will be detailed on Chapter 6, focused on practical issues arising when carrying several estimations relying on on-board sensors only). It represents a significant improvement compared to an open-loop estimation<sup>7</sup>. Typical results obtained on experimental data are reported in Figure 3.5.1. The shell under consideration is a 155 mm in ballistic flight. An accurate measurement of its local velocity is obtained by the state-of-the-art ground based position radar we presented earlier. As is visible in Figure 3.5.1, our method allows one to approach this value, even from a very poor initial estimate of the shell velocity (50 % error). The reader should keep in mind we are comparing an estimation of the velocity w.r.t. the airflow to the local velocity. We define an arbitrary confidence interval of  $\pm 15 \text{ m.s}^{-1}$  around the radar reference in which the actual velocity w.r.t. the airflow should lie for visualization purposes.

## 3.6 Conclusion

As we have illustrated it, the estimation methodology represents a significant improvement compared to an open-loop estimation.

For the control applications described in Section 1.3 one can note that the shell trajectory is controlled by impulsive actions near the end of the flight. The convergence time of our observer thus is not a limiting factor in

---

<sup>6</sup>often, experiments are postponed if the measured wind at ground level is above 10 m/s.

<sup>7</sup>i.e. forward-time integration from some given initial conditions.

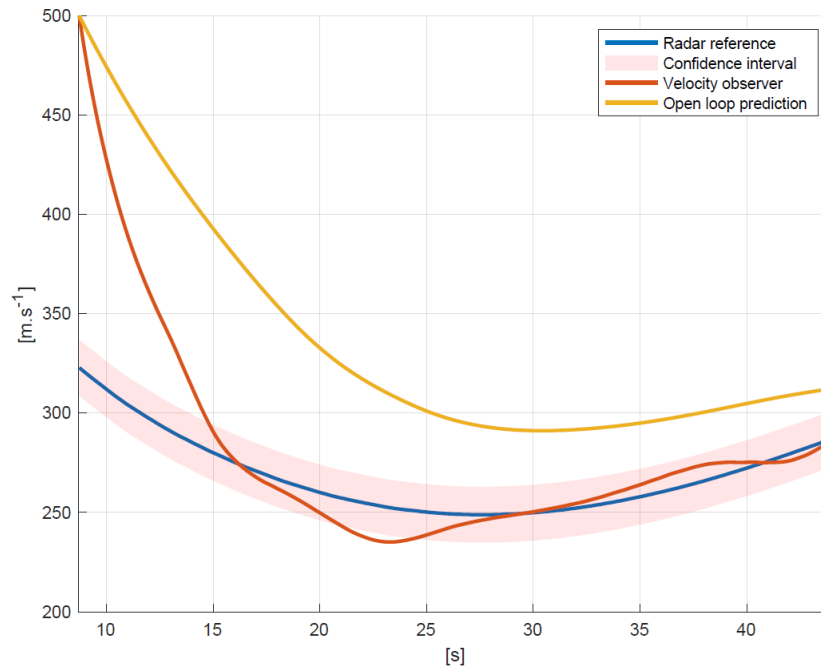


Figure 3.5.1: Velocity Observer compared to an open-loop estimation (experimental results).

that regard, as long as it has converged with satisfying accuracy before the attitude estimation is carried out and the controller is being used.

This estimation of the velocity enables us to use the aerodynamic model of the shell to carry out an attack and sideslip angles estimation, which would be a useful input to know the attitude of the shell and estimating its position by integration, and makes this a key part of any navigation algorithm. This is certainly a path to explore in future works. As for its use in this thesis, we will show in the next chapters how the velocity estimation can provide an input on the attitude, via slope angle estimation.

## Chapitre 4 - Résumé

On cherche ici à obtenir une information d'orientation partielle pour compléter la direction donnée par le magnétomètre 3-axes. Pour ce faire, on va utiliser la dynamique de la vitesse, dont le chapitre précédent propose une méthode d'estimation. Grâce aux variations de la vitesse, il est possible de former un observateur de l'angle de pente d'une munition en vol, qui à terme fera office d'estimation approchée de son angle de tangage. Un observateur est présenté, et sa convergence exponentielle démontrée sur un horizon de temps fixe quantifiable, au bout duquel les gains doivent être mis à jour. Un filtre de Kalman étendu, plus simple d'implémentation, a été utilisé en pratique, et des résultats obtenus sur des données de simulation et des données expérimentales sont présentés.



## Chapter 4

# Slope estimation through an analysis of the velocity dynamics

The previous chapters have focused on providing an estimate of the shell velocity with respect to the air, by exploiting the low frequencies of the shell epicyclic motion.

Prior to addressing the attitude estimation problem, we focus on a particular angle, the pitch angle, which can be directly related to the velocity discussed above. Indeed, the slope angle heavily influence the shell trajectory, as illustrated in Figure 4.1.1 where trajectories with various initial pitch angle (only differing from the slope angle by the angle of attack) are reported.

Previously, in Chapter 3 an estimate of the translational velocity w.r.t. the airflow of the shell was proposed. According to the description of the translational dynamics in Chapter 2, the velocity of the shell in-flight is only affected by the drag force and the gravity. Observing its variations over time is a way to estimate the slope angle, and consequently the pitch angle, under the assumption that it is approximately equal to the former. This is the approach developed in this chapter.

### 4.1 Slope angle observer

As a reminder of the notations in Chapter 2, the slope angle is defined by the orientation of the shell velocity, and is equal to the pitch angle when the

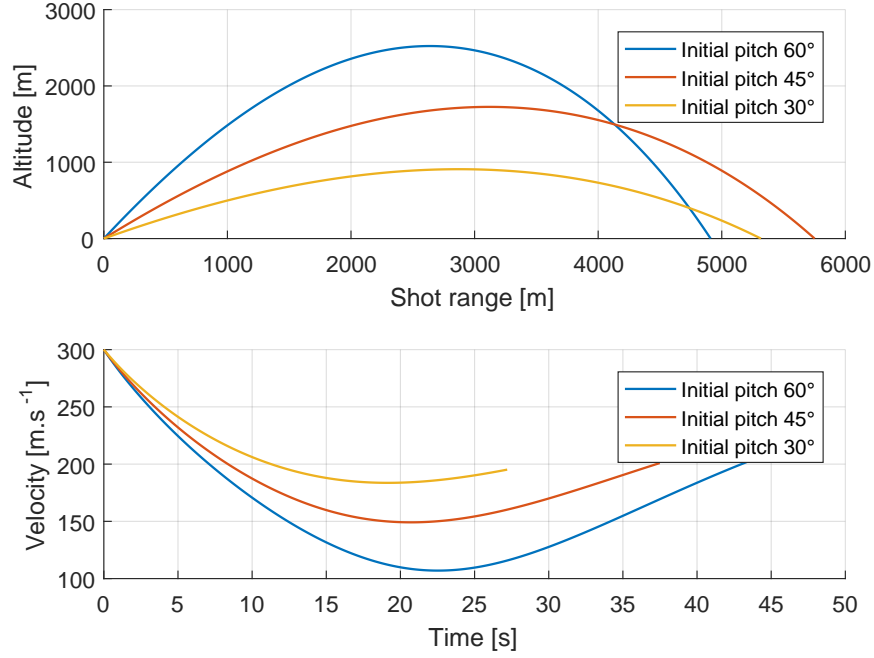


Figure 4.1.1: Altitude and local Velocity for various initial pitch angles [simulation results].

total angle of attack is zero, which is true on average <sup>1</sup> in typical flights (see Figure 2.4.1 for typical values of incidence angles).

Below, a method is exposed to construct  $\hat{\theta}$  an estimate of  $\theta$  from a measurement of the linear velocity  $v$ , by exploiting the equations (containing a reordering of (2.4.1)) obtained under the assumptions of zero total angle of attack.

$$\begin{cases} \dot{h} &= v \sin \theta \\ \dot{\theta} &= \omega \\ \dot{\omega} &= f(t) \\ \dot{v} &= -\frac{\rho(h)S\tilde{C}_D(h,v,0)v^2}{2M} - g \sin \theta \end{cases}$$

where  $f(t) = \ddot{\theta}$  is an unknown bounded function of time. Let us define the

---

<sup>1</sup>except near apogee.

following output injection observer, with  $D(h, v) \triangleq \frac{\rho(h)S\tilde{C}_D(h, v, 0)v^2}{2M}$

$$(4.1.1) \quad \begin{cases} \dot{\hat{h}} &= v \sin \hat{\theta} + l_1(v - \hat{v}) \\ \dot{\hat{\theta}} &= \omega + l_2(v - \hat{v}) \\ \dot{\hat{\omega}} &= l_3(v - \hat{v}) \\ \dot{\hat{v}} &= -D(\hat{h}, v) - g \sin \hat{\theta} + l_4(v - \hat{v}) \end{cases}$$

The error dynamics is, with the usual notations  $\tilde{h} = h - \hat{h}$ ,  $\tilde{\theta} = \theta - \hat{\theta}$ ,  $\tilde{\omega} = \omega - \hat{\omega}$ ,  $\tilde{v} = v - \hat{v}$ ,

$$(4.1.2) \quad \begin{cases} \dot{\tilde{h}} &= v(\sin \theta - \sin \hat{\theta}) - l_1(v - \hat{v}) \\ \dot{\tilde{\theta}} &= \tilde{\omega} - l_2(v - \hat{v}) \\ \dot{\tilde{\omega}} &= f(t) - l_3(v - \hat{v}) \\ \dot{\tilde{v}} &= -(D(h, v) - D(\hat{h}, v)) - g(\sin \theta - \sin \hat{\theta}) - l_4(v - \hat{v}) \end{cases}$$

This can be rewritten as a linear time-varying (LTV) model

$$(4.1.3) \quad \dot{\tilde{X}} = A(t)\tilde{X} + B(t)$$

with

$$(4.1.4) \quad A(t) = \begin{pmatrix} 0 & v \int_0^1 \cos(\hat{\theta} + (1-s)(\theta - \hat{\theta})) ds & 0 & -l_1 \\ 0 & 0 & 1 & -l_2 \\ 0 & 0 & 0 & -l_3 \\ -\int_0^1 \frac{\partial D}{\partial h}(\hat{h} + (1-s)(h - \hat{h}), v) ds & -g \int_0^1 \cos(\hat{\theta} + (1-s)(\theta - \hat{\theta})) ds & 0 & -l_4 \end{pmatrix}$$

$$(4.1.5) \quad B(t) = \begin{pmatrix} 0 \\ 0 \\ f(t) \\ 0 \end{pmatrix}$$

To elaborate, the derivative of the drag force  $D$  with respect to the altitude  $h$  is

$$(4.1.6) \quad -\frac{\partial D}{\partial h}(h, v) = -\frac{\partial \rho}{\partial h} \frac{S\tilde{C}_D(h, v, 0)v^2}{2M} - \frac{\rho(h)Sv^2}{2M} \frac{\partial \tilde{C}_D}{\partial h}(h, v, 0)$$

with, using the model of § 2.2,

$$(4.1.7) \quad \begin{cases} \frac{\partial \rho}{\partial h} &= \frac{-0.0065 \times 4.2561}{T_0 - 0.0065h} \rho \\ \frac{\partial \tilde{C}_D}{\partial h}(h, v, 0) &= -\frac{v}{v_{sound}(h)^2} \frac{\partial v_{sound}}{\partial h} \frac{\partial C_D}{\partial N_{mach}} \left( \frac{v}{v_{sound}(h)}, 0 \right) \\ \frac{\partial \tilde{C}_D}{\partial v}(h, v, 0) &= \frac{1}{v_{sound}(h)} \frac{\partial C_D}{\partial N_{mach}} \left( \frac{v}{v_{sound}(h)}, 0 \right) \\ \frac{\partial v_{sound}}{\partial h} &= \frac{-0.0065a_0}{2T_0} \left( \frac{T_0}{T_0 - 0.0065h} \right)^{\frac{1}{2}} \end{cases}$$

### 4.1.1 Observer design

$A$  can be rewritten as

$$(4.1.8) \quad A(t) \triangleq \begin{pmatrix} 0 & a_1(t) & 0 & -l_1 \\ 0 & 0 & 1 & -l_2 \\ 0 & 0 & 0 & -l_3 \\ a_2(t) & -a_3(t) & 0 & -l_4 \end{pmatrix}$$

with the  $a_i$  being time-varying functions with strictly positive values.

For any given time  $t_0$ , consider the matrix

$$A_0 = \begin{pmatrix} 0 & a_1(t_0) & 0 & 0 \\ 0 & 0 & 1 & 0 \\ 0 & 0 & 0 & 0 \\ a_2(t_0) & -a_3(t_0) & 0 & 0 \end{pmatrix}$$

From the (frozen-time) observability matrix of the pair  $(A_0, (0 \ 0 \ 0 \ 1))$  which is

$$\begin{pmatrix} 0 & 0 & 0 & 1 \\ a_2(t_0) & -a_3(t_0) & 0 & 1 \\ 0 & a_1(t_0) a_2(t_0) & -a_3(t_0) & 1 \\ 0 & 0 & a_1(t_0) a_2(t_0) & 1 \end{pmatrix}$$

and is clearly non singular, there exist gains  $l_1, l_2, l_3, l_4$  such that the matrix

$$(4.1.9) \quad A_0 - LC = \begin{pmatrix} 0 & a_1(t_0) & 0 & -l_1 \\ 0 & 0 & 1 & -l_2 \\ 0 & 0 & 0 & -l_3 \\ a_2(t_0) & -a_3(t_0) & 0 & -l_4 \end{pmatrix}$$

is Hurwitz. The error dynamics can be rewritten, without any approximation, under the form

$$(4.1.10) \quad \dot{\tilde{X}} = (A_0 - LC + \epsilon_1(t)A_1 + \epsilon_2(t)A_2 + \epsilon_3(t)A_3)\tilde{X} + B(t)$$

with the following matrices:

$$A_1 = \begin{pmatrix} 0 & 1 & 0 & 0 \\ 0 & 0 & 0 & 0 \\ 0 & 0 & 0 & 0 \\ 0 & 0 & 0 & 0 \end{pmatrix}, \quad A_2 = \begin{pmatrix} 0 & 0 & 0 & 0 \\ 0 & 0 & 0 & 0 \\ 0 & 0 & 0 & 0 \\ 1 & 0 & 0 & 0 \end{pmatrix}, \quad A_3 = \begin{pmatrix} 0 & 0 & 0 & 0 \\ 0 & 0 & 0 & 0 \\ 0 & 0 & 0 & 0 \\ 0 & -1 & 0 & 0 \end{pmatrix}$$

and the variables

$$(4.1.11) \quad \epsilon_1 = a_1(t) - a_1(t_0), \quad \epsilon_2 = a_2(t) - a_2(t_0), \quad \epsilon_3 = a_3(t) - a_3(t_0)$$

Since  $A_0 - LC$  is Hurwitz, there exists  $P$  a symmetric definite positive matrix such that

$$P(A_0 - LC) + (A_0 - LC)^T P = -I$$

Choosing the candidate Lyapunov function  $V$  defined by  $V(t) = \tilde{X}^T P \tilde{X}$ , one obtains

$$(4.1.12) \quad \dot{V} = -\tilde{X}^2 + \sum_{i=1}^3 \epsilon_i(t) \tilde{X}^T (A_i^T P + P A_i) \tilde{X}$$

To obtain exponential stability, one needs to ensure that  $\sup \epsilon_i(t) \|(A_i^T P + P A_i)\|$  remains small enough. For sufficiently short duration after  $t_0$ , this will be granted by the Lipschitz continuity in (4.1.11). The acceptable bound on the duration will depend on  $A_0$  (which defines  $P$ , and then the quantities  $\|(A_i^T P + P A_i)\|$ ). Over the duration, the constant gain  $L$  need not be updated.

In details, a sufficient exponential stability condition on  $[t_0, t_1]$  is

$$\sum_i \sup_{t \in [t_0, t_1]} |\epsilon_i(t)| \|(A_i^T P + P A_i)\| < 1$$

Note  $M_i$  the Lipschitz constant of the  $a_i$  (w.r.t. time), then the proposed observer is exponentially stable on  $[t_0, t_1[$  where

$$(4.1.13) \quad t_1 = t_0 + \frac{1}{\sum_i M_i \|(A_i^T P + P A_i)\|}$$

Quantitatively, a preliminary change of variables gives some flexibility. Consider  $Z = NX$ , with  $N$  invertible, so that we get, with  $\bar{A}_i = N A_i N^{-1}$ , with  $P$  such that  $PN(A_0 - LC)N^{-1} + (N(A_0 - LC)N^{-1})^T P = -I_4$  and  $V = Z^T P Z$ , so that  $\dot{V} = -\tilde{Z}^2 + \sum_i \epsilon_i(t) Z^T (\bar{A}_i^T P + P \bar{A}_i) Z$ . For a given gain  $L$ , the proposed observer is then exponentially stable on  $[t_0, t_1[$  where

$$(4.1.14) \quad t_1 = t_0 + \sup \frac{1}{N \sum_i M_i \|\bar{A}_i^T P + P \bar{A}_i\|}$$

This result is mostly theoretical, and for treatment of the actual case of interest we will replace it with a standard EKF.

## 4.1.2 Simulation results

For the sake of implementation, the results we will showcase are obtained on an Extended Kalman Filter (EKF) relying on the same model as the observer we offered in last section. Figure 4.1.2 shows the evolution of the EKF gains over time, regarding each state  $h, \theta, \dot{\theta}, v$ .

The results displayed in Figure 4.1.3 correspond to the simulated data set 1 (see Table 2.8.1), using the simulated velocity of the shell.

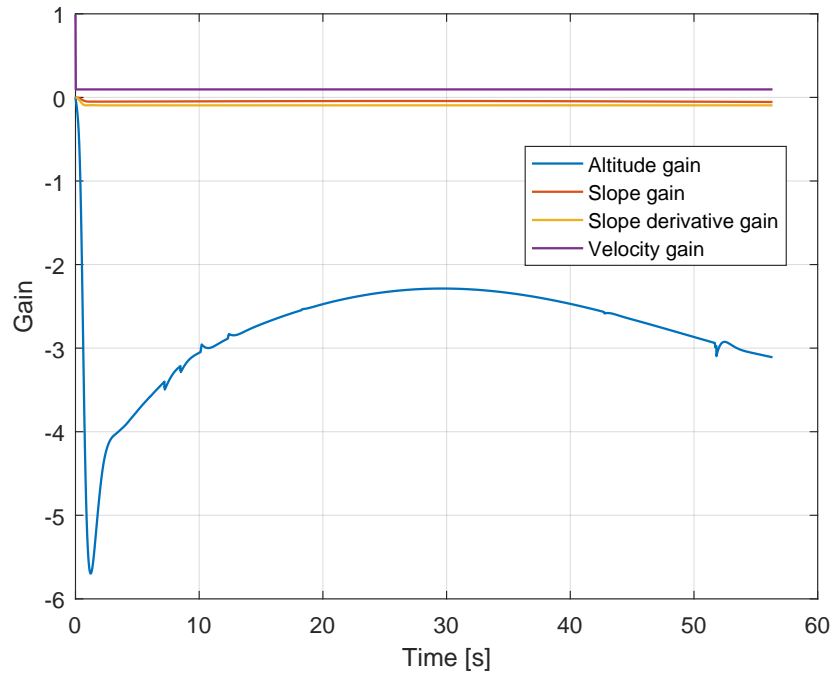


Figure 4.1.2: Evolution of the gains of an EKF for slope angle estimation [simulation results].

### 4.1.3 Experimental results

For the sake of the implementation, the results we will showcase are obtained on an Extended Kalman Filter (EKF) relying on the same model as the observer we offered in last section. Figure 4.1.4 shows the evolution of the EKF gains over time, regarding each state  $(h, \theta, \dot{\theta}, v)$ .

The results reported in Figure 4.1.5 are implemented on data set 2 (see Table 2.8.1), using a ground based position radar measurement of the velocity, as a proof of concept. It appears that the slope angle can be estimated with a residual error of less than 2 deg. An obvious delay is visible, this could be improved by extending the state of the observer. The final results displayed in Chapter 6 will correspond to a fully on-board method, but will rely on a less accurate velocity measurement, obtained as described in Chapter 3.

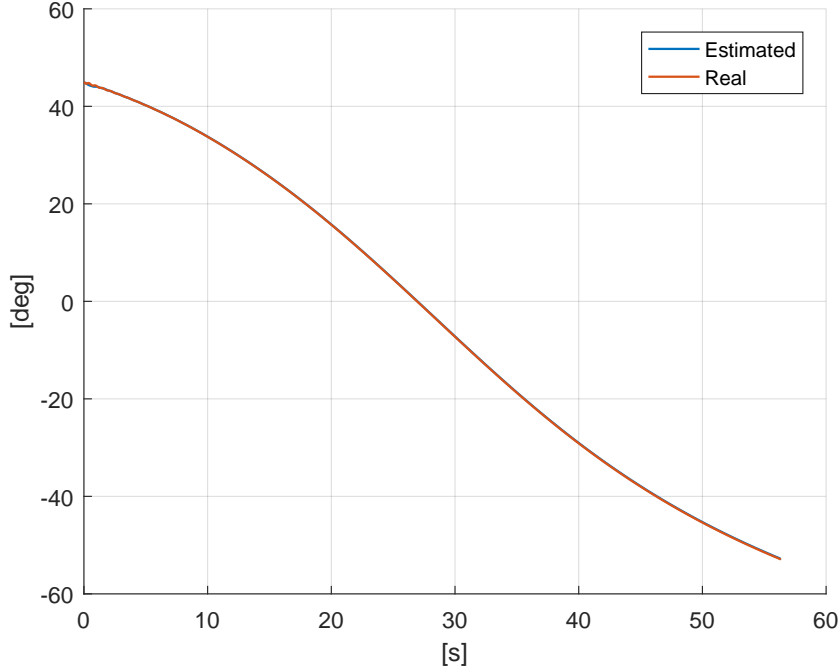


Figure 4.1.3: Slope angle estimation from velocity [simulation results].

## 4.2 From the slope angle to the pitch angle

The slope angle we estimate here is related to the velocity orientation, and is not strictly equal to the pitch angle (they are equal if the incidence of the shell is zero).

A good approximation at small total angle of attack is

$$(4.2.1) \quad \hat{\Theta} = \hat{\theta} + \alpha_2$$

which can be used if we are able to estimate the shell incidence from transverse accelerometers.

The global results we will present in Chapter 6 will use this correction for simulation data, as we have access to the angle of attack, but will not for actual gyrostabilized shells. Instead we will use the slope angle observer as a pitch angle observer :

$$(4.2.2) \quad \hat{\Theta} = \hat{\theta}$$

The additional error we introduce by making this assumption is bounded

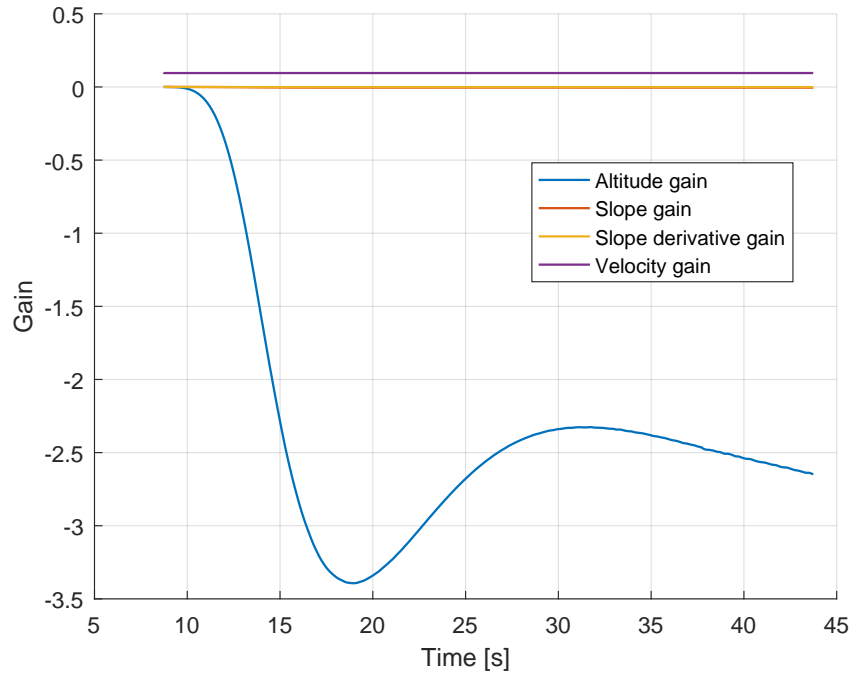


Figure 4.1.4: Evolution of the gains of an EKF for slope angle estimation [experimental results on 155 mm, data set 2].

by the total angle of attack of the shell, which commonly does not exceed a few degrees, and exponentially decreases during the course of the flight.

### 4.3 Conclusion

An output injection gain observer has been provided to reconstruct the slope angle under assumption of small total angle of attack. A procedure has been established to compute constant gains that provide exponential convergence over a covering of the flight time interval. In practice, it should be noted that the estimate of the frequency of necessary update of the gain is conservative, and that a single gain is usually sufficient to obtain exponential convergence over the whole flight. Advantageously, if computational load is not a concern, an EKF can be preferred. This will be used in Chapter 6, even if the conditions of convergence of the EKF will not be treated (Uniform Complete Observability [82] will not be investigated).

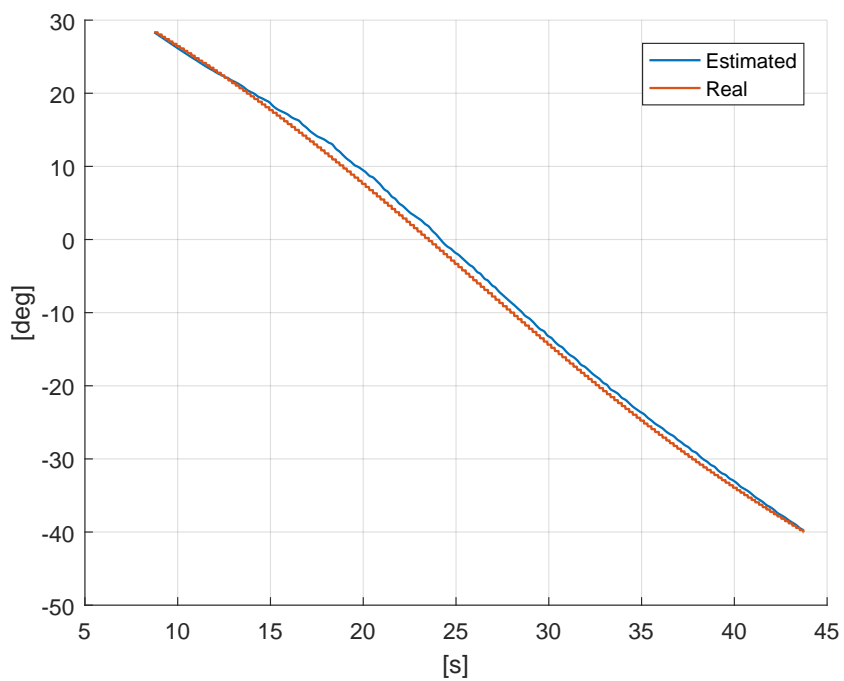


Figure 4.1.5: Slope angle estimation from ground based position radar velocity. A ground based position radar provides velocity measurements to be treated by the proposed observer [experimental results on 155 mm, data set 2]. Initialization is delayed due to the availability of the input from radar measurements.



## Chapitre 5 - Résumé

Ce chapitre aborde enfin le problème central d'estimation d'attitude. Avant d'intégrer celle-ci à notre étude, en utilisant les mesures et estimations préalablement obtenues, il propose un estimateur d'attitude inspiré du filtrage complémentaire. L'estimateur proposé utilise une information d'orientation partielle, sous la forme d'une mesure d'angle de tangage, remplaçant la mesure de direction manquante et complétant celle donnée par le magnétomètre. On introduira dans un premier temps quelques résultats de convergence partielle du filtrage complémentaire utilisant une seule mesure de direction, et les solutions algébriques d'une attitude donnant même mesure de champ magnétique et même angle de tangage que l'attitude réelle, avant d'introduire notre observateur corrigé utilisant la mesure d'angle de tangage pour recalibrer le résultat du filtre complémentaire. Une preuve de convergence est donnée, et des résultats de simulation et expérimentaux sont présentés.



## Chapter 5

# An attitude observer from 3-axis Magnetometer and pitch angle

To provide an estimate of the attitude we now use the 3-axis Magnetometer as one direction measurement, and use the pitch estimation constructed in Chapter 4 as an additional input.

The reader should bear in mind that gyroscopes are not available. We simply replace them with spin rate estimation, as described in Section 2.6.

This chapter offers an adaptation of the classic complementary filter for attitude of a rigid body, based on [67], using the pitch angle estimation instead of a second direction measurement. By construction, in Section 2.6 and Appendix B.1, the spin rate estimate is not biased. Therefore, it is not necessary to implement the gyro bias compensation equation in the complementary filter, which is left out of the discussion.

### 5.1 A quaternion representation of the problem

The set of unit quaternions is denoted  $\mathbb{Q} = \{q = (s, v \triangleq \text{dir}(q)) \in \mathbb{R} \times \mathbb{R}^3, |q| = 1\}$ . It is a group under the operation  $\otimes$  with

$$q_1 \otimes q_2 = \begin{pmatrix} s_1 s_2 - v_1^T v_2 \\ s_1 v_2 + s_2 v_1 + v_1 \times v_2 \end{pmatrix}$$

with identity element  $(1, 0, 0, 0)$ . The group of unit quaternions is homomorphic to  $SO_3$ , the group of all rotations about the origin of  $\mathbb{R}^3$ , via the mapping

$$(5.1.1) \quad F(q) := I_3 + 2s[v_\times] + 2[v_\times]^2$$

where  $[v_\times]$  is the skew-symmetric matrix corresponding to the cross product in  $\mathbb{R}^3$ ,  $v \times \cdot$ . This map is a two to one mapping of  $\mathbb{Q}$  onto  $SO_3$  with kernel

$$\{(1, 0, 0, 0), (-1, 0, 0, 0)\}$$

Thus,  $\mathbb{Q}$  is locally isomorphic to  $SO_3$  via  $F$ . Given  $R \in SO_3$  such that  $R = \exp(\theta a_\times)$ , then

$$F^{-1}(R) = \{\pm(\cos(\frac{\theta}{2}), \sin(\frac{\theta}{2})a)\}$$

For convenience, we will define the quaternion associated with the rotation  $R = \exp(\theta a_\times)$  as

$$q_{\theta,a} = \left( \cos\left(\frac{\theta}{2}\right), \sin\left(\frac{\theta}{2}\right)a \right)$$

Let  $\omega$  denote a body-fixed frame velocity, then the pure quaternion  $\mathbf{p}(\omega) \triangleq (0, \omega)$  is associated with a quaternion velocity. The usual rotation kinematics thus becomes

$$(5.1.2) \quad \dot{\hat{q}} = \frac{1}{2} \hat{q} \otimes \mathbf{p}(\omega)$$

## 5.2 Single-direction attitude complementary filter

### 5.2.1 Recalls on attitude complementary filter

Consider a rigid body subjected to an angular velocity  $\omega$  which is equipped with two embedded vector sensors producing measurements

$$(5.2.1) \quad v_i = R^T \hat{v}_i, \quad i = 1, 2$$

where  $R$  is the rotation matrix describing the rigid body attitude w.r.t. a set inertial frame, and  $\hat{v}_1, \hat{v}_2$  are two constant vectors expressed in the inertial frame. Without loss of generality, the vectors  $\hat{v}_1, \hat{v}_2$  are unit vectors<sup>1</sup>. They are assumed to be non-colinear, i.e.  $\hat{v}_1^T \hat{v}_2 \neq 0$ . The dynamics of the attitude matrix  $R$  are, by definition,

$$(5.2.2) \quad \dot{R} = R[\omega_\times]$$

In [68], the following result has been established :

---

<sup>1</sup>in practical applications these vectors corresponds to fixed directions, e.g. direction to the Sun, or to the center of the Earth, local magnetic field, among others.

**Theorem 2.** [Explicit complementary filter [68]] The filter defined by

$$(5.2.3) \quad \begin{cases} \dot{\hat{R}} = \hat{R} \left( [(\omega^y - \hat{b})_{\times}] + k_P [\sigma_{\times}] \right) \\ \dot{\hat{b}} = -k_I \sigma \\ \sigma = k_1 v_1 \times (\hat{R}^T \hat{v}_1) + k_2 v_2 \times (\hat{R}^T \hat{v}_2) \end{cases}$$

where  $\omega^y = \omega + b$  is the measurement from an embedded gyro assumed to be corrupted with a constant bias  $b$ , and where  $k_I$  and  $k_P$  are constant positive tuning parameters, has three unstable equilibria characterized by

$$(\hat{R}_{\star i}, \hat{b}_{\star i}) \triangleq (U_0 D_i U_0^T R, b), i = 1, 2, 3$$

where  $D_1 = \text{diag}(1, -1, -1)$ ,  $D_2 = \text{diag}(-1, 1, -1)$  and  $D_3 = \text{diag}(-1, -1, 1)$ , and  $U_0 \in SO(3)$  such that

$$M_0 \triangleq \sum_{i=1}^2 k_i \hat{v}_i \hat{v}_i^T = U_0 \Lambda U_0^T$$

with  $\Lambda$  a diagonal matrix. Its error  $(\tilde{R}(t), \tilde{b}(t))$  is locally exponentially stable to  $(I, 0)$  and for almost all initial conditions  $(\hat{R}_0, \hat{b}_0) \neq (\hat{R}_{\star i}^T R, b)$  the trajectory  $(\hat{R}(t), \hat{b}(t))$  converges to the trajectory  $(R(t), b)$ .

## 5.2.2 Partial convergence using a single direction

The complementary filter of [67, 68] can deal with an arbitrary number of direction measurements. When the number of linearly independent direction is larger or equal to 2, the filter converges to the true value of the attitude, in almost all cases (except on the zero-measure set described in the statement), see Theorem 2. With a single direction the filter converges to a continuous set that is not restricted to the actual attitude. Some partial convergence results can be stated and will prove to be instrumental in the adaptation we propose. These results, already established in [67], will be the focus of this section.

Consider the following single direction observer, without bias compensation, which is directly obtained from [67]:

$$(5.2.4) \quad \dot{\hat{R}} = \hat{R} \left( [\omega_{\times}] + k_p [(Y_{mag} \times \hat{R}^T b_0)_{\times}] \right)$$

where  $Y_{mag} = R^T b_0$  is the measurement from the 3-axis Magnetometer.

With  $\hat{q}$  the unit quaternions representation of  $\hat{R}$ ,  $\otimes$  the quaternion product, and  $\mathbf{p}$  is the operator defining the pure quaternion of its argument (see again Section 5.1), an equivalent formulation is

$$(5.2.5) \quad \dot{\hat{q}} = \frac{1}{2} \hat{q} \otimes \mathbf{p} \left( \omega + k_p (Y_{mag} \times (\hat{q}^{-1} b_0 \hat{q})) \right)$$

In what follows,  $\sigma(q, \hat{q})$  or shortly  $\sigma(t)$  or  $\sigma$  will stand for

$$(5.2.6) \quad \sigma \triangleq Y_{mag} \times (\hat{q}^{-1} b_0 \hat{q}) = (q^{-1} b_0 q) \times (\hat{q}^{-1} b_0 \hat{q})$$

Commonly,  $\sigma$  is referred to as the innovation vector. It is null when the measurement matches the prediction. For any quaternions  $q_1, q_2$  in  $\mathbb{Q}$ , we define the following error functions

$$(5.2.7) \quad \delta(q_1, q_2) \triangleq 2 \arccos((q_2 \otimes q_1^{-1})_1)$$

$$(5.2.8) \quad u(q_1, q_2) \triangleq \begin{cases} \frac{\text{dir}(q_2 \otimes q_1^{-1})}{\sin \frac{\delta(q_1, q_2)}{2}} & \text{if } \delta(q_1, q_2) \neq 0 \\ b_0 & \text{otherwise} \end{cases}$$

where  $(\cdot)_1$  is the first component of its argument and  $\text{dir}$  is the last three components of its argument (see Section 5.1). From eqs. (5.2.7) and (5.2.8), one has

$$q_2 = q_{\delta(q_1, q_2), u(q_1, q_2)} \otimes q_1$$

The convergence analysis provided in [67] states that, in almost all cases<sup>2</sup>,

$$(5.2.9) \quad \lim_{t \rightarrow +\infty} \sigma(t) = 0$$

Additionally, since  $\hat{q}^{-1} b_0 \hat{q}$  converges exponentially to  $q^{-1} b_0 q$  (see [67]), and following the definition of  $\sigma$ , the convergence stated by (5.2.9) is exponential as well, i.e. there exists  $\kappa > 0, \mu > 0$  such that

$$(5.2.10) \quad \forall t \geq 0, \|\sigma(t)\| \leq \kappa \|\sigma(0)\| \exp(-\mu t)$$

Equation (5.2.9) implies

$$(5.2.11) \quad (q \otimes \hat{q}^{-1}) \cdot b_0 \cdot (\hat{q} \otimes q^{-1})(t) \rightarrow b_0, \quad \text{as } t \rightarrow +\infty$$

Equivalently, since by definition of  $\otimes$

$$q \otimes \hat{q}^{-1} = \begin{pmatrix} \cos\left(\frac{\delta(q, \hat{q})}{2}\right) \\ \sin\left(\frac{\delta(q, \hat{q})}{2}\right) u(q, \hat{q}) \end{pmatrix}$$

one has

$$(5.2.12) \quad \left( I + 2\delta(q, \hat{q})[u(q, \hat{q})_{\times}] + 2[u(q, \hat{q})_{\times}]^2 \right) b_0 \rightarrow b_0, \quad \text{as } t \rightarrow +\infty$$

To analyze this property, consider two alternatives: either  $\delta(q, \hat{q}) \rightarrow 0$  or there exists an unbounded sequence  $(t_n > 0)$  such that  $\delta(q(t_n), \hat{q}(t_n)) >$

<sup>2</sup>except for a set having zero-measure, see the unstable equilibrium described by Theorem 2.

$M$  for some  $M > 0$ . The first one gives  $[u(q, \hat{q})_\times]^2 b_0 \rightarrow 0$  which implies  $u(q, \hat{q}) \rightarrow b_0$ . The second case yields the same conclusion. Indeed we have

$$(5.2.13) \quad 2\delta(q, \hat{q})[u(q, \hat{q})_\times]b_0 + [u(q, \hat{q})_\times]^2 b_0 \rightarrow 0$$

If  $u(q, \hat{q})$  was not converging to  $b_0$ , there would be a contradiction since we could extract from  $[u(q, \hat{q})_\times]b_0$  and  $-[u(q, \hat{q})_\times]^2 b_0$  two infinite sequences of non zero orthogonal vectors, which would contradict (5.2.13). Gathering the arguments above, we get the following result :

$$(5.2.14) \quad \lim_{t \rightarrow +\infty} u(q(t), \hat{q}(t)) = b_0$$

### 5.3 Complementarity of pitch angle information and magnetic vector measurement

As previously discussed, when employed with the 3-axis Magnetometer signals only, the complementary filter (5.2.4)-(5.2.5) converges according to (5.2.9) and (5.2.14), which means that  $\hat{q}$  asymptotically approaches a set containing the true attitude quaternion  $q$ . The set is not limited to this desirable value, unfortunately.

We intend to design an observer adding the knowledge of the pitch angle corresponding to the true attitude. As will be discussed in this section, this information is well complementing the measurement of the magnetic vector direction. Several properties will explain this.

#### 5.3.1 Reduction of the convergence set

##### Attitude solutions

Let us define the following quadratic functions on  $\mathbb{Q}$

$$(5.3.1) \quad q = (q_1, q_2, q_3, q_4) \rightarrow \begin{cases} T(q) = q_1 q_3 - q_2 q_4 \\ T_2(q) = q_1 q_4 + q_2 q_3 \\ T_3(q) = 1 - 2(q_3^2 + q_4^2) \\ T_4(q) = q_1 q_2 + q_3 q_4 \\ T_5(q) = 1 - 2(q_2^2 + q_3^2) \end{cases}$$

It is worth noting that the Tait-Bryan angles are directly expressed as

$$(5.3.2) \quad \begin{cases} \Psi(q) = \arctan \frac{2T_2(q)}{T_3(q)} \\ \Theta(q) = \arcsin 2T(q) \\ \Phi(q) = \arctan \frac{2T_4(q)}{T_5(q)} \end{cases} \quad \ll \text{pitch angle} \gg$$

Let us define, for any  $q \in \mathbb{Q}$ , the set

$$(5.3.3) \quad C(q) = \{q', u(q, q') = b_0\} = \{q', q^{-1}b_0q = q'^{-1}b_0q'\} = \{q', \sigma(q, q') = 0\}$$

corresponding of the set of attitudes  $q'$  sharing the same 3-axis Magnetometer measurement as  $q$ .

The question naturally arising when considering the additional pitch angle information is: what are the  $q_f$  verifying both conditions in (5.3.4)?

$$(5.3.4) \quad \begin{cases} q_f \in C(q) \\ T(q_f) = T(q) \end{cases}$$

or equivalently :

$$(5.3.5) \quad \begin{cases} \sigma(q, q_f) = 0 \\ T(q_f) = T(q) \end{cases}$$

Given that  $C(q)$  is the intersection of  $\text{span}(q, \mathbf{p}(b_0) \otimes q)$ , and the unit sphere of  $\mathbb{R}^4$ , it is a circle of  $\mathbb{R}^4$  and we can parametrize it with  $t$  :

$$(5.3.6) \quad C(q) = \{(\cos t)q + (\sin t)(\mathbf{p}(b_0) \otimes q), t \in [0, 2\pi]\}$$

An immediate solution of (5.3.4) is  $q_f = q$  ; what are the others ? The parametrization (5.3.6) gives the answer to this question. With the notations

$$(5.3.7) \quad \begin{cases} b_0 \triangleq [a \ b \ c]^T \\ q_t = (\cos t)q + (\sin t)(\mathbf{p}(b_0) \otimes q) \end{cases}$$

some heavy calculation (see Appendix A.5) yields

$$T(q_t) = (\cos^2 t)T(q) + (\cos t \sin t)(bT_3(q) - 2aT_2(q)) + (\sin^2 t)(-acT_3(q) - 2bcT_2(q)) + (\sin^2 t)(c^2 - a^2 - b^2)T(q)$$

implying that there exists only two  $t \in [0, \pi[$  solutions for  $T(q_t) = T(q)$  : the obvious  $t = 0$  (corresponding to  $q_t = q$  and the following (see again see Appendix A.5) :

$$(5.3.8) \quad t_{\#} = \frac{\pi}{2} + \arctan \left( \frac{bT_3(q) - 2aT_2(q)}{2(a^2 + b^2)T(q) + acT_3(q) + 2bcT_2(q)} \right)$$

which corresponds to  $q^{\#}$  under the form

$$(5.3.9) \quad q \mapsto q^{\#} \triangleq (\cos t_{\#})q + (\sin t_{\#})(\mathbf{p}(b_0) \otimes q)$$

yielding

$$\begin{cases} q^{\#} \in C(q) \\ T(q^{\#}) = T(q) \\ q^{\#} \neq q \text{ in most cases, as we will see with Proposition 2} \end{cases}$$

The two additional (besides  $t = 0$  and  $t = t_{\#}$ ) solutions in  $[0, 2\pi[$  are just  $t = \pi$  and  $t = t_{\#} + \pi$ , corresponding to  $-q$  and  $-q_{\#}$ , representing the same rotations in  $SO_3$ .

In the end, we can now formulate the following proposition.

**Proposition 1.** *There are only four elements of  $C(q)$  having the same pitch angle  $\Theta$  as  $q$ . These are  $q$ ,  $-q$ ,  $q_{\#}$  and  $-q_{\#}$ . They define only two rotations in  $SO_3$ .*

### Separation of the solutions

According to the preceding proposition, one should anticipate that any observer we might construct based on the additional knowledge of the pitch angle is bound to converge to any of the two isolated rotations. In the following we explain how the whole 3-sphere  $\mathbb{Q}$  can be separated into two potential basins of attraction for  $q$  and  $q_{\#}$ . The need for this property will naturally arise when we introduce our proposed observer in the next section.

As a preliminary remark, let us notice, after some steps of calculus, that for any  $q \in \mathbb{Q}$ , we have

$$(5.3.10) \quad \nabla T(q)^T (\mathbf{p}(b_0) \otimes q) = bT_3(q) - 2aT_2(q)$$

This quantity is linked to the local variation of the pitch of the quaternion  $q$  onto which a rotation around  $b_0$  has been applied (precisely, it is the first order coefficient of the local expansion of  $T(q_{\delta, b_0} \otimes q)$  in  $\delta$ .)

Let us define the sets

$$(5.3.11) \quad \begin{cases} E_0 = \{q \in \mathbb{Q}, \nabla T(q)^T (\mathbf{p}(b_0) \otimes q) = 0\} \\ E_+ = \{q \in \mathbb{Q}, \nabla T(q)^T (\mathbf{p}(b_0) \otimes q) > 0\} \\ E_- = \{q \in \mathbb{Q}, \nabla T(q)^T (\mathbf{p}(b_0) \otimes q) < 0\} \end{cases}$$

Geometrically,  $E_0$  is the intersection of the sphere  $\mathbb{Q}$  and a hyperplane separating  $E_+$  from  $E_-$ .

Then, one has the following.

**Proposition 2.** *For any  $q \in \mathbb{Q}$ , exactly one among those properties holds:*

$$\begin{aligned} (5.3.12a) \quad & \left\{ \begin{array}{l} q \in E_0 \wedge q = q_{\#} \\ q \in E_+ \wedge q_{\#} \in E_- \\ q \in E_- \wedge q_{\#} \in E_+ \end{array} \right. \\ (5.3.12b) \quad & \\ (5.3.12c) \quad & \end{aligned}$$

*Additionally,  $-q$  and  $-q_{\#}$  lie in the same set as their counterparts  $q$  and  $q_{\#}$  respectively*

The proof directly follows from the definition of the sets (5.3.11), the fact that properties (5.3.12a)-(5.3.12b)-(5.3.12c) are mutually exclusive and jointly exhaustive, and that  $\nabla T(-q) = -\nabla T(q)$  and  $\mathbf{p}(b_0) \otimes (-q) = -\mathbf{p}(b_0) \otimes q$ .

### 5.3.2 A continuity property

**Proposition 3** (Small innovation and pitch error imply small  $\delta$ ). *For any  $\varepsilon > 0$ , there exist  $(\varepsilon_1, \varepsilon_2)$  such that, for any  $(q, q') \in \mathbb{Q}^2$*

$$\begin{cases} \|\sigma(q, q')\| < \varepsilon_1 \\ |T(q) - T(q')| < \varepsilon_2 \end{cases} \implies \min(|\delta(q, q')|, |\delta(-q, q')|, |\delta(q_{\#}, q')|, |\delta(-q_{\#}, q')|) < \varepsilon$$

where  $q_{\#}$  is given by (5.3.9).

*Proof.* By contradiction, let us assume there exist  $\varepsilon > 0$ , such that for all  $\varepsilon' > 0$ , there exist  $q'$  such that

$$(5.3.13) \quad \begin{cases} \|\sigma(q, q')\| < \varepsilon' \\ |T(q) - T(q')| < \varepsilon' \\ \min(|\delta(q, q')|, |\delta(-q, q')|, |\delta(q_{\#}, q')|, |\delta(-q_{\#}, q')|) \geq \varepsilon \end{cases}$$

Let us choose a sequence  $(\varepsilon'_n)$  converging to zero, and a sequence  $(q'_n)$  such that, for all integer  $n$

$$(5.3.14) \quad \begin{cases} \|\sigma(q, q'_n)\| < \varepsilon'_n \\ |T(q) - T(q'_n)| < \varepsilon'_n \\ \min(|\delta(q, q'_n)|, |\delta(-q, q'_n)|, |\delta(q_{\#}, q'_n)|, |\delta(-q_{\#}, q'_n)|) \geq \varepsilon \end{cases}$$

The mapping  $\delta$  defines a distance on  $\mathbb{Q}$ . Therefore, the set

$$Q_0 \triangleq \mathbb{Q} \setminus \{q', \min(|\delta(q, q')|, |\delta(-q, q')|, |\delta(q_{\#}, q')|, |\delta(-q_{\#}, q')|) < \varepsilon\}$$

is a compact set. The continuous function  $q' \mapsto \|\sigma(q, q')\| + |T(q) - T(q')|$  reaches a non-zero (since its zeros on  $\mathbb{Q}$ , given by Proposition 1, are isolated) minimum  $m$  on  $Q_0$ . Since every  $q'_n$  belongs to  $Q_0$ , every  $\|\sigma(q, q'_n)\| + |T(q) - T(q'_n)|$  is superior to  $m$ , contradicting the fact it should converges to zero, through the inequality  $\|\sigma(q, q'_n)\| + |T(q) - T(q'_n)| < 2\varepsilon'_n$ .

□

Proposition 3 would be sufficient to show asymptotic stability of the observer using pitch angle and magnetometer measurement we will introduce later. We will complete this property in the proof of convergence, showing how  $\varepsilon_1$  and  $\varepsilon_2$  are related to  $\varepsilon$ . This will be of use to guarantee exponential stability.

## 5.4 Proposed observer

We now present the observer we propose (see below in (5.4.1)). It is a modified version of the complementary filter, as can be seen in its first line below. The second equation is a gradient-based integrator, containing a comparison of the actual pitch and the predicted one. The gain contains a linearizing term which is saturated. The prediction is performed on the basis of the update quaternion  $\bar{q}$  obtained by a rotation of the filtered quaternion  $\hat{q}$ , the rotation being of magnitude defined by the state  $\chi$  of the gradient-based integrator. The input of the observer are the innovation  $\sigma$  computed using the 3-axis Magnetometer measurement according to (5.2.6) as before, the angular rate  $\omega$  as before (here supposed to be known, which will be replaced in applications by the estimate discussed in Section 2.6), and the pitch angle under the form  $T(q)$ . The output of interest of the observer is  $\bar{q}$ .

$$(5.4.1) \quad \begin{cases} \dot{\hat{q}} = \frac{1}{2} \hat{q} \otimes \mathbf{p}(\omega + k_p \sigma) \\ \sigma \triangleq Y_{mag} \times (\hat{q}^{-1} b_0 \hat{q}) \\ \dot{\chi} = k_c \frac{T(q) - T(\bar{q})}{f(\nabla T(\bar{q})^T(\mathbf{p}(b_0) \otimes \bar{q}))} \\ \bar{q} = \left( \cos \frac{\chi}{2} + \sin \frac{\chi}{2} b_0 \right) \otimes \hat{q} \end{cases}$$

where the measured pitch angle gives  $\frac{1}{2} \sin(\Theta) = T(q)$ , and with

$$f : x \mapsto \sqrt{1 + x^2} / \tanh(x)$$

The graph of the smooth function  $f$  is given in Figure 5.4.1. Because  $1/f(\cdot)$  is always defined, the observer (5.4.1) is well defined for all times  $t \geq 0$ .

## 5.5 Assumptions on the flight

In the following  $\text{Cl}(\cdot)$  designates the closure (in the set sense).

**Assumption 1.** *The compact set  $D_{flight} \triangleq \text{Cl}(\{q(t), t \geq 0\})$  is strictly contained into  $E_+$  i.e.  $D_{flight} \subsetneq E_+$ .*

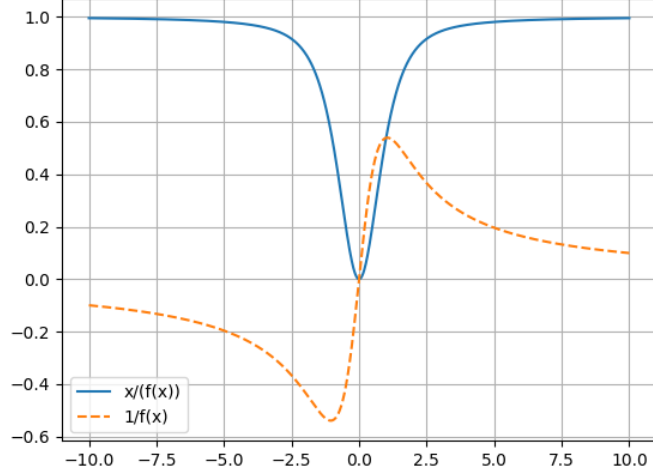


Figure 5.4.1: Mapping used to define the observer gain in (5.4.1).

Assumption 1 can be made without loss of generality, the reverse situation (where  $q$  lies in  $E_-$  and  $q_{\#}$  in  $E_-$ ) being strictly equivalent in the rest of the proof. Under Assumption 1, we directly get the following properties :

**Proposition 4** ( $q$  stays in  $E_+$ ). *For all  $t \geq 0$ ,  $\nabla T(q)^T(\mathbf{p}(b_0) \otimes q) \neq 0$*

**Proposition 5** ( $q_{\#}$  stays in  $E_-$ ). *There exists a compact set  $D_{flight\#} \subsetneq E_-$  such that for all  $t, q_{\#}(t) \in D_{flight\#}$ . On  $D_{flight\#}$ , one has  $\nabla T(q_{\#})^T(\mathbf{p}(b_0) \otimes q_{\#}) \neq 0$ .*

Quaternions lie in the unit sphere of  $\mathbb{R}^4$ . To visualize these, the classical stereographic projection of this unit sphere onto  $\mathbb{R}^3$  can be used, as is done in Figure 5.5.1. In this figure the stereographic view of the trajectories of  $q$  and  $q_{\#}$  in  $\mathbb{R}^3$  are represented. The stereographic mapping is described by (5.5.1). It is chosen such that its only singularity corresponds to the identity rotation. This last situation, in a ballistic flight, never occurs, since the body frame is never fully aligned with the local frame. It naturally defines an isomorphic function from  $\{q \in \mathbb{Q}, q_1 \neq -1\}$  onto  $\mathbb{R}^3$ .

$$(5.5.1) \quad q \mapsto \frac{1}{1 + q_1} \begin{pmatrix} q_2 & q_3 & q_4 \end{pmatrix}$$

This view is handy to interpret Assumption 1. On a typical 155 mm shell flight, Figure 5.5.1 reports the stereographic representation of  $q$  and  $q_{\#}$ . Their loci appear to be non intersecting. This property makes Assumption 1

true :  $q(t)$  varies continuously, and because  $q \in E_0$  implies  $q_{\#} = q$  from Proposition 2, for the trajectory  $q$  to intersect  $E_0$  one should have that at some instant  $q_{\#} = q$ , which is never the case as shown in Figure 5.5.1.

Additionally, the quantities  $\nabla T(q)^T(\mathbf{p}(b_0) \otimes q)$  and  $\nabla T(q_{\#})^T(\mathbf{p}(b_0) \otimes q_{\#})$  are displayed in Figure 5.5.2. Both quantities remains away from zero during the flight, stressing again that  $q$  remains in  $E_+$  and  $q_{\#}$  in  $E_-$  (without loss of generality, the reverse is possible and would not contradict Proposition 4 and 5, which are the relevant consequences of Assumption 1 we will actually use).

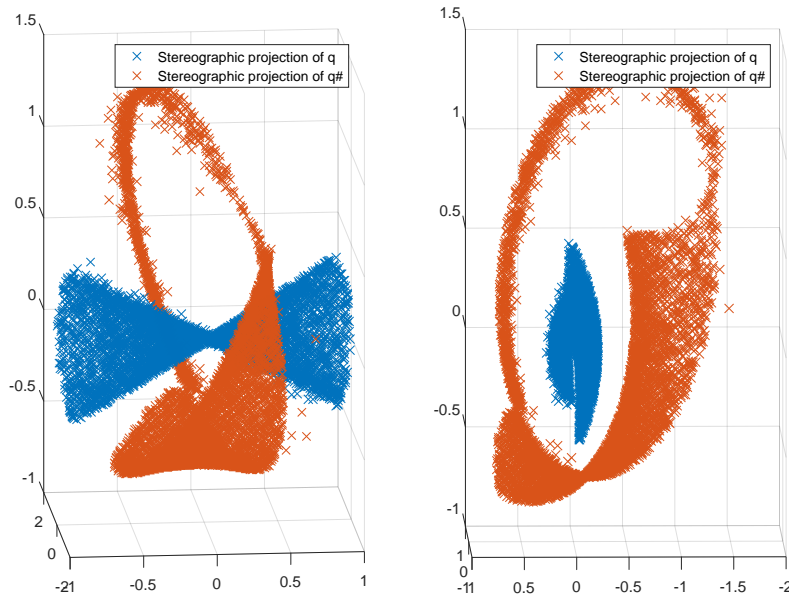


Figure 5.5.1: Stereographic representation of  $q$  and  $q_{\#}$  during the flight. Their loci are non intersecting, as shown by two different views. Simulation results for a typical 155 mm flight.

We will need a second assumption on the boundedness of the angular velocity of the shell during a flight, which physical interpretation is that the aerodynamics and the gravity cannot indefinitely increase  $\omega$  :

**Assumption 2.** *There exists  $\omega_{max} > 0$  such that for all  $t \geq 0$ ,  $|\omega(t)| < \omega_{max}$*

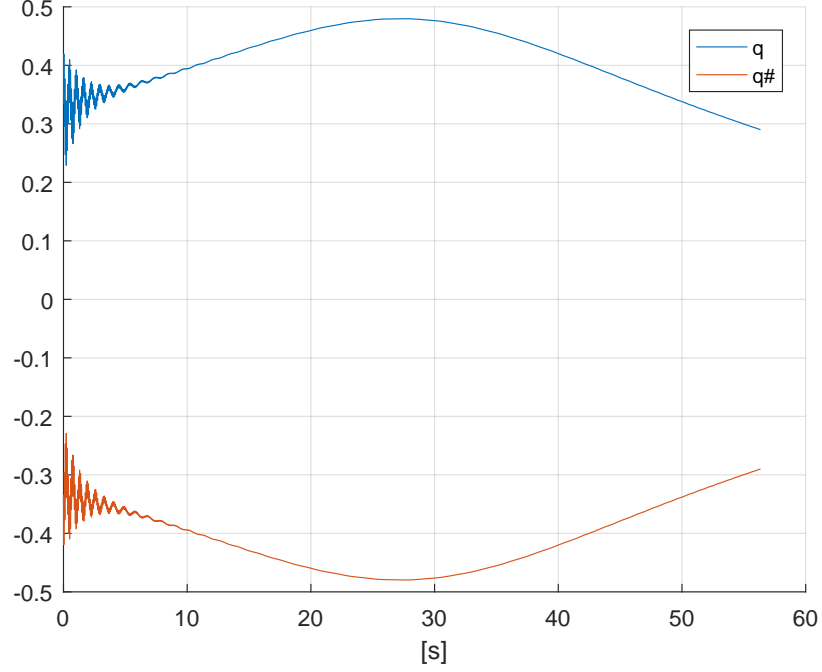


Figure 5.5.2: Variation of the quantities  $\nabla T(q)^T(\mathbf{p}(b_0) \otimes q)$  and  $\nabla T(q\#)^T(\mathbf{p}(b_0) \otimes q\#)$  during a typical 155 mm flight.

## 5.6 Main result

**Theorem 3** (Main result). *Let us assume  $\hat{q}(0)$  and  $\chi(0)$  are such that  $\bar{q}(0) \notin E_0$ . There exist  $\eta_2 > 0$  such that, for any  $\varepsilon > 0$  small enough, there exist  $\eta_1 > 0$  and  $k_{c*} > 0$  such that, if  $\|\sigma(0)\| < \eta_1$ ,  $|T(q(0)) - T(\bar{q}(0))| < \eta_2$  and  $k_c > k_{c*}$ , there exist  $K, \lambda > 0$  such that :*

$$\forall t \geq 0, \min(|\delta(q, \bar{q})|, |\delta(-q, \bar{q})|, |\delta(q\#, \bar{q})|, |\delta(-q\#, \bar{q})|) < \varepsilon + K \exp^{-\lambda t}.$$

Next section will be dedicated to the proof of Theorem 3.

## 5.7 Proof of convergence

### 5.7.1 Asymptotic behavior

Consider

$$(5.7.1) \quad V_1 = 1 - \langle Y_{mag}, \hat{R}^T b_0 \rangle = 1 - \langle R^T b_0, \hat{R}^T b_0 \rangle$$

$$(5.7.2) \quad V_2 = \frac{1}{2} \left| \frac{1}{2} \sin(\Theta) - T(\bar{q}) \right|^2 = \frac{1}{2} |T(q) - T(\bar{q})|^2$$

Differentiating  $V_2$  yields :

$$(5.7.3) \quad \dot{V}_2 = \left( \nabla T(q)^T \dot{q} - \nabla T(\bar{q})^T \dot{\bar{q}} \right) (T(q) - T(\bar{q}))$$

By substituting, using  $q_{\chi+\pi, b_0} = q_{\pi, b_0} \otimes q_{\chi, b_0} = \mathbf{p}(b_0) \otimes q_{\chi, b_0}$  and the associative property of  $(\mathbb{Q}, \otimes)$ ,

$$(5.7.4) \quad \dot{\bar{q}} = \left( \cos \frac{\chi}{2} + \sin \frac{\chi}{2} b_0 \right) \otimes \dot{q} + \frac{\dot{\chi}}{2} \mathbf{p}(b_0) \otimes \left( \cos \frac{\chi}{2} + \sin \frac{\chi}{2} b_0 \right) \otimes \hat{q}$$

one obtains

$$\dot{V}_2 = - \frac{k_c}{2} \frac{\nabla T(\bar{q})^T (\mathbf{p}(b_0) \otimes \bar{q})}{f(\nabla T(\bar{q})^T (\mathbf{p}(b_0) \otimes \bar{q}))} |T(q) - T(\bar{q})|^2 + B(q, \hat{q}, \chi)$$

Or, more conveniently,

$$(5.7.5) \quad \dot{V}_2 = - \frac{k_c}{2} h(\bar{q}) V_2 + B(q, \hat{q}, \chi)$$

with

$$(5.7.6) \quad h(\bar{q}) \triangleq \frac{\nabla T(\bar{q})^T (\mathbf{p}(b_0) \otimes \bar{q})}{f(\nabla T(\bar{q})^T (\mathbf{p}(b_0) \otimes \bar{q}))}$$

and

$$B(q, \hat{q}, \chi) \triangleq \left( \nabla T(q)^T \dot{q} - \nabla T(\bar{q})^T \left( \cos \frac{\chi}{2} + \sin \frac{\chi}{2} b_0 \right) \otimes \dot{q} \right) (T(q) - T(\bar{q}))$$

which rewrites

$$(5.7.7) \quad B(q, \hat{q}, \chi) = \frac{1}{2} \left( \nabla T(q)^T (q \otimes \mathbf{p}(\omega)) - \nabla T(\bar{q})^T (\bar{q} \otimes \mathbf{p}(\omega + \sigma)) \right) (T(q) - T(\bar{q}))$$

or under the form,  $B = B_1 + B_2$  with

$$(5.7.8) \quad \begin{cases} B_1(q, \hat{q}, \chi) \triangleq \frac{1}{2} \left( \nabla T(q)^T (q \otimes \mathbf{p}(\omega)) - \nabla T(\bar{q})^T (\bar{q} \otimes \mathbf{p}(\omega)) \right) (T(q) - T(\bar{q})) \\ B_2(q, \hat{q}, \chi) \triangleq -\frac{1}{2} \left( \nabla T(\bar{q})^T (\bar{q} \otimes \mathbf{p}(\sigma)) \right) (T(q) - T(\bar{q})) \end{cases}$$

Let us note that  $|B|$  can be simply bounded using (5.7.7) and the expression of  $\sigma$ , independently of  $q, \bar{q}, \chi$ , using the fact it can be seen as a continuous function of  $(q, \bar{q}, \omega)$  which lies in a compact set (see Assumption 2). We will denote  $B_{max}$  its upper bound.

Under the assumptions of Theorem 3,  $\bar{q}(0) \notin E_0$ . By definition (5.3.11), this implies  $\nabla T(\bar{q}(0))^T (\mathbf{p}(b_0) \otimes \bar{q}(0)) \neq 0$ . This property can be propagated for all times as stated below in Proposition 6.

**Proposition 6** ( $\bar{q}$  stays on one side of  $E_0$ ). *There exist  $\varepsilon_a > 0$ ,  $\varepsilon_b > 0$ , and  $k'_c$  such that if  $\|\sigma(0)\| \leq \varepsilon_a$ ,  $|T(q(0)) - T(\bar{q}(0))| < \varepsilon_b$ , and  $k_c \geq k'_c$  then one has*

$$(5.7.9) \quad \forall t \geq 0, \quad \nabla T(\bar{q}(t))^T (\mathbf{p}(b_0) \otimes \bar{q}(t)) \neq 0$$

and

$$(5.7.10) \quad \forall t \geq 0, \quad h(\bar{q}(t)) > \ell$$

for some  $\ell > 0$ .

*Proof.* From Assumption 1, there exists  $\varepsilon_c$  such that if for all  $t \geq 0$ , one has

$$\min(|\delta(q(t), \bar{q}(t))|, |\delta(-q(t), \bar{q}(t))|, |\delta(q_{\#}(t), \bar{q}(t))|, |\delta(-q(t)_{\#}, \bar{q}(t))|) \leq \varepsilon_c$$

then one has (5.7.9).

Consider  $\Delta_\varepsilon$  the set

$$\{q_1 \in \mathbb{Q}, \text{ s.t. } \exists q \in D_{flight} \\ \text{with } \min(|\delta(q, q_1)|, |\delta(-q, q_1)|, |\delta(q_{\#}, q_1)|, |\delta(-q_{\#}, q_1)|) \leq \varepsilon_c\}$$

Because  $\delta$  is a distance over  $\mathbb{Q}$ ,  $\Delta_\varepsilon$  is a compact set. By construction, it has no intersection with  $E_0$ . Therefore there exists  $\ell_1$  such that for all  $q \in \Delta_\varepsilon$ ,

$$|\nabla T(q)^T (\mathbf{p}(b_0) \otimes q)| \geq \ell_1 > 0$$

For the considered  $\varepsilon_c$ , Proposition 3 gives two positive constants  $\varepsilon_1, \varepsilon_2$ .

From (5.2.10), one has that, if  $\|\sigma(0)\| < \varepsilon_1/\kappa \triangleq \varepsilon_a$  then

$$(5.7.11) \quad \forall t \geq 0, \quad \|\sigma(t)\| < \varepsilon_1$$

Let us choose  $|T(q(0)) - T(\bar{q}(0))| < b < \varepsilon_2$  and  $k_c \geq k'_c > \frac{4B_{max}}{lb^2}$ . we know from (5.7.5) that if for some  $t$  we have  $|T(q(t)) - T(\bar{q}(t))| = \varepsilon_2$  then  $\dot{V}_2(t) < 0$ .

If the set  $\{t, |T(q(t)) - T(\bar{q}(t))| \geq \varepsilon_2\}$  was not empty, using the continuity of the function  $t \mapsto |T(q(t)) - T(\bar{q}(t))|$ , there would exist  $t_c$  such that  $|T(q(t_c)) - T(\bar{q}(t_c))| = b$  and  $\dot{V}_2(t_c) > 0$ . We know from (5.7.5) and from the choice of  $k_c$  that  $\dot{V}_2(t_c) < 0$  giving us a contradiction.

As a consequence, we have established that there exist  $k'_c$  such that if  $k_c \geq k'_c$  and  $|T(q(0)) - T(\bar{q}(0))| < \varepsilon_2 \triangleq \varepsilon_b$  then

$$(5.7.12) \quad \forall t \geq 0, |T(q(t)) - T(\bar{q}(t))| < \varepsilon_2$$

Therefore, gathering (5.7.11) and (5.7.12), one has,  $\forall t \geq 0$ ,

$$\min (|\delta(q(t), \bar{q}(t))|, |\delta(-q(t), \bar{q}(t))|, |\delta(q_{\#}(t), \bar{q}(t))|, |\delta(-q_{\#}(t), \bar{q}(t))|) < \varepsilon_c$$

which gives the conclusion with the desired constant (using the parity of  $h$ )

$$h(\ell_1) \triangleq \ell > 0$$

□

**Proposition 7.** *With the notations of Proposition 6, if  $\|\sigma(0)\| \leq \varepsilon_a$ ,  $|T(q(0)) - T(\bar{q}(0))| < \varepsilon_b$ , then for all  $\varepsilon_d > 0$ , there exists  $k_c''$  and  $t_2 > 0$  such that, if  $k_c \geq \max(k_c', k_c'')$ ,*

$$(5.7.13) \quad \forall t \geq t_2, \quad V_2(t) \leq \varepsilon_d$$

*Proof.* Under the assumptions of the statement, one has, from (5.7.5), that for all  $t \geq 0$

$$(5.7.14) \quad \dot{V}_2 \leq -\frac{k_c}{2} \ell V_2 + B(q, \hat{q}, \chi)$$

where  $|B|$  is bounded by  $B_{max}$ . Applying the differential version of Grönwall's inequality gives the conclusion. □

**Proposition 8.** *With the notations of Proposition 6, if  $\|\sigma(0)\| \leq \varepsilon_a$ ,  $|T(q(0)) - T(\bar{q}(0))| < \varepsilon_b$ , then for all  $\varepsilon > 0$ , there exists  $t_3$  such that*

$$\forall t \geq t_3, \quad \min (|\delta(q, \bar{q})|, |\delta(-q, \bar{q})|, |\delta(q_{\#}, \bar{q})|, |\delta(-q_{\#}, \bar{q})|) < \varepsilon$$

*Proof.* For any  $\varepsilon > 0$ , Proposition 3 defines  $\varepsilon_1 > 0$  and  $\varepsilon_2 > 0$ . Proposition 7 defines  $t_2$  for  $\varepsilon_d = \varepsilon_2$ . Using (5.2.10), the result is obtained with

$$t_3 \triangleq \max \left( t_2, \frac{1}{\mu} (\log(\kappa \varepsilon_a) - \log \varepsilon_1) \right) > 0$$

□

Proposition 8 describes the asymptotic behavior of the observer. As  $t \rightarrow +\infty$ ,  $\bar{q}$  approaches one of the distinct elements  $q$ ,  $-q$ ,  $q_{\#}$  or  $-q_{\#}$ . To characterize the convergence we now consider two exclusive cases defined by Proposition 9 below.

**Proposition 9.** *For  $\varepsilon > 0$  small enough, with the notations of Proposition 8, one (and only one) of the following statements hold:*

1. for all  $t \geq t_3$ ,  $\min (|\delta(q_{\#}(t), \bar{q}(t))|, |\delta(-q_{\#}(t), \bar{q}(t))|) > \varepsilon$

2. for all  $t \geq t_3$ ,  $\min(|\delta(q_{\#}(t), \bar{q}(t))|, |\delta(-q_{\#}(t), \bar{q}(t))|) \leq \varepsilon$

*Proof.* For  $\varepsilon$  small enough, for any  $t \geq 0$ , the  $\varepsilon$ -neighborhoods w.r.t. the  $\delta$  distance of  $q(t)$ ,  $-q(t)$ ,  $q_{\#}(t)$  or  $-q_{\#}(t)$  are four disjoint compact sets. Therefore, Proposition 9 is a direct consequence of Proposition 8. Alternatively, this means that with the notation of Proposition 8, after time  $t_3$  the estimate  $\bar{q}$  either stays within  $\varepsilon$  of  $\pm q$  or within  $\varepsilon$  of  $\pm q_{\#}$  w.r.t.  $\delta$ .  $\square$

Next, the proof is organized around two exclusive alternatives. Either the following assumption holds or not.

**Assumption 3.** *With the notation of Proposition 8, there exists  $\varepsilon > 0$  such that Item 1 above is true.*

### 5.7.2 First case: Assumption 3 holds

Let us start with a preliminary property.

**Proposition 10.** *There exist  $\varepsilon'_a > 0$  and  $l_2 > 0$  such that if  $\|\sigma(0)\| < \varepsilon'_a$ , one has*

$$\forall t \geq 0, |\nabla T(q)^T(\mathbf{p}(u(q, \bar{q})) \otimes q)| \geq l_2$$

*Proof.* From Assumption 1, we know that there exist  $l_2 > 0$  such that  $|\nabla T(q)^T(\mathbf{p}(b_0) \otimes q)| > 2l_2$  for all time  $t \geq 0$  (if that was not the case,  $E_0$  would obviously have an intersection with the closure of the trajectory of  $q$ , contradicting Assumption 1).

From (5.2.14) and the continuity of the function

$$v \mapsto \nabla T(q)^T(\mathbf{p}(v) \otimes q)$$

there exist  $\varepsilon'_a > 0$  such that if  $\|\sigma(0)\| < \varepsilon'_a$ , then one has, for all time  $t \geq 0$ ,

$$|\nabla T(q)^T(\mathbf{p}(u(q, \bar{q})) \otimes q) - \nabla T(q)^T(\mathbf{p}(b_0) \otimes q)| < l_2$$

This implies  $|\nabla T(q)^T(\mathbf{p}(u(q, \bar{q})) \otimes q)| \geq l_2$  which concludes the proof  $\square$

We now pursue the analysis of (5.7.5). Let us focus on the first term in (5.7.8). Using

$$\begin{aligned} \nabla T(q)^T(q \otimes \mathbf{p}(\omega)) &= \begin{pmatrix} q_3 & -q_4 & q_1 & -q_2 \end{pmatrix} \begin{pmatrix} -q_2\omega_1 - q_3\omega_2 - q_4\omega_3 \\ q_1\omega_1 + q_3\omega_3 - q_4\omega_2 \\ q_2\omega_2 - q_2\omega_3 + q_4\omega_1 \\ q_3\omega_3 + q_2\omega_2 - q_3\omega_1 \end{pmatrix} \\ &= \omega_2 T_3(q) - 2\omega_3 T_2(q) \end{aligned}$$

and (5.3.1), we get

(5.7.15)

$$B_1(q, \hat{q}, \chi) = \frac{\omega_2}{2}(T_5(q) - T_5(\bar{q}))(T(q) - T(\bar{q})) - \omega_3(T_4(q) - T_4(\bar{q}))(T(q) - T(\bar{q}))$$

It is useful to establish that the  $T_i(q) - T_i(\bar{q})$ ,  $i \in \{4, 5\}$  vary in a similar fashion as  $T(q) - T(\bar{q})$ , by considering the following expansions :

$$\begin{cases} T(q) - T(\bar{q}) = \frac{\delta(\bar{q}, q)}{2} \nabla T(q)^T(\mathbf{p}(u(q, \bar{q})) \otimes q) + O(\delta(q, \bar{q})^2) \\ T_i(q) - T_i(\bar{q}) = \frac{\delta(\bar{q}, q)}{2} \nabla T_i(q)^T(\mathbf{p}(u(q, \bar{q})) \otimes q) + O(\delta(q, \bar{q})^2), i \in \{4, 5\} \end{cases}$$

**Proposition 11.** *Under Assumption 3, if  $\|\sigma(0)\| < \varepsilon'_a$ , there exist  $C_4 > 0$ ,  $C_5 > 0$  such that for all  $t \geq t_3$ , one has*

$$(5.7.16) \quad \begin{cases} -C_4(T(q) - T(\bar{q})) < T_4(q) - T_4(\bar{q}) < C_4(T(q) - T(\bar{q})) \\ -C_5(T(q) - T(\bar{q})) < T_5(q) - T_5(\bar{q}) < C_5(T(q) - T(\bar{q})) \end{cases}$$

*Proof.* If  $\|\sigma(0)\| < \varepsilon'_a$  we have  $\nabla T(q)^T(\mathbf{p}(u(q, \bar{q})) \otimes q) > l_2$ .

Let us denote  $C_{\varepsilon, l_2}$  the following set

$\{(q_1, q_2), q_1 \in D_{flight} \text{ and } q_2 \in \mathbb{Q} \text{ s.t.}$

$$\min(|\delta(q_1, q_2)|, |\delta(-q_1, q_2)|) \geq \varepsilon \text{ and } |\nabla T(q_1)^T(\mathbf{p}(u(q_1, q_2)) \otimes q_1)| \geq l_2\}$$

From Proposition 10, under Assumption 3, we know that if  $\|\sigma(0)\| < \varepsilon'_a$ , then for any  $t \geq t_3$ ,  $(q(t), \bar{q}(t))$  lies in  $C_{\varepsilon, l_2}$  which is a compact set.

Let us consider, for  $i \in \{4, 5\}$  the function  $r_i : (q_1, q_2) \mapsto \frac{T_i(q_1) - T_i(q_2)}{T(q_1) - T(q_2)}$ . We will show that this function can be continuously defined on the compact set  $C_{\varepsilon, l_2}$ .

For a fixed  $q_1 \in D_{flight}$ , the only potential singularities of  $r_i$  on  $C_{\varepsilon, l_2}$  are to  $q_2 = \pm q_1$ .

Let us focus on the extension of our ratio function  $r_i$  for  $q_1 = q_2$ . We know that we have :

(5.7.17)

$$\begin{cases} T(q_1) - T(q_2) = \frac{\delta(q_1, q_2)}{2} \nabla T(q_1)^T(\mathbf{p}(u(q_1, q_2)) \otimes q_1) + O(\delta(q_1, q_2)^2) \\ T_i(q_1) - T_i(q_2) = \frac{\delta(q_1, q_2)}{2} \nabla T_i(q_1)^T(\mathbf{p}(u(q_1, q_2)) \otimes q_1) + O(\delta(q_1, q_2)^2) \end{cases}$$

Knowing that  $\nabla T(q_1)^T(\mathbf{p}(u(q_1, q_2)) \otimes q_1)$  is non zero for  $(q_1, q_2) \in C_{\varepsilon, l_2}$ , the extension of the ratio function  $r_i$  on the whole compact set  $C_{\varepsilon, l_2}$  is trivial, using the following :

$$(5.7.18) \quad \tilde{r}_i(q_1, q_1) = \frac{\nabla T_i(q_1)^T(\mathbf{p}(b_0) \otimes q_1)}{\nabla T(q_1)^T(\mathbf{p}(b_0) \otimes q_1)}$$

The other singularities ( $q_2 = -q_1$ ) are treated in a similar way.

Thus  $\tilde{r}_i$  is defined on the compact set  $C_{\varepsilon, l_2}$  and continuous, so it is bounded. The same applies to  $r_i$ , concluding the proof.  $\square$

**Proposition 12** (Quadratic bound on  $B_1$ ). *Let us define  $\omega_M > 0$  such that for all  $t$ ,  $\max(\omega_2(t), \omega_3(t)) \leq \omega_M$ . Under Assumption 3, if  $\|\sigma(0)\| < \varepsilon'_a$ , for all  $t \geq t_3$ , one has*

$$(5.7.19) \quad |B_1(q, \hat{q}, \chi)| < \omega_M \left( \frac{C_5}{2} + C_4 \right) (T(q) - T(\bar{q}))^2$$

*Proof.* Under Assumption 3, Proposition 11 holds. Then we get, for all  $t \geq t_3$  the following

$$\begin{aligned} |\omega_3(T_4(q) - T_4(\bar{q}))(T(q) - T(\bar{q}))| &< \omega_M C_4 (T(q) - T(\bar{q}))^2 \\ |\omega_2(T_5(q) - T_5(\bar{q}))(T(q) - T(\bar{q}))| &< \omega_M C_5 (T(q) - T(\bar{q}))^2 \end{aligned}$$

Then, one concludes the proof using these inequalities into (5.7.15).  $\square$

We will now focus on the second term in (5.7.8) which we recall for convenience

$$B_2(q, \hat{q}, \chi) \triangleq -\frac{1}{2} \left( \nabla T(\bar{q})^T (\bar{q} \otimes \mathbf{p}(\sigma)) \right) (T(q) - T(\bar{q}))$$

From (5.2.9),  $\sigma$  converges exponentially to zero. Additionally, using

$$\begin{aligned} \nabla T(\bar{q})^T (\bar{q} \otimes \mathbf{p}(\sigma)) &= \frac{\sigma_2}{2} T_3(\bar{q}) - \sigma_3 T_2(\bar{q}) \\ |T_2(\bar{q})| &\leq 1 \\ |T_3(\bar{q})| &\leq 1 \end{aligned}$$

we get

$$|\nabla T(\bar{q})^T (\bar{q} \otimes \mathbf{p}(\sigma))| \leq \frac{3}{2} \|\sigma\|$$

Adding  $|T(q) - T(\bar{q})| < 1$  (the image of  $T$  is included in  $[-\frac{1}{2}, \frac{1}{2}]$ ), the expression of  $B_2$  naturally leads to

$$(5.7.20) \quad |B_2(q, \hat{q}, \chi)| \leq \frac{3}{4} \|\sigma\|$$

**Proposition 13** (Local exponential convergence of the pitch error). *If  $k_c^* > \frac{\omega_M}{\ell} \left( \frac{C_5}{2} + C_4 \right)$ , and under Assumption 3, then  $V_2$  is exponentially converging to zero.*

*Proof.* Gathering eqs. (5.7.19) and (5.7.20) and (5.7.14), one has for all  $t \geq t_3$

$$(5.7.21) \quad \dot{V}_2 < - \left( k_c^* \ell - \omega_M \left( \frac{C_5}{2} + C_4 \right) \right) V_2 + \frac{3}{4} \|\sigma\|$$

directly yielding

$$(5.7.22) \quad \dot{V}_2 < -\lambda V_2 + K \exp^{-\mu t}$$

with  $\lambda \triangleq k_c \ell - \omega_M \left( \frac{C_5}{2} + C_4 \right) > 0$ ,  $K > 0$ .

Applying the classical differential version of Grönwall's inequality, one obtains

$$V_2(t) \leq \exp(-\lambda t) V_2(t_3) + \frac{K}{\lambda - \mu} (\exp(-\mu t) - \exp(-\lambda t))$$

which gives the conclusion.  $\square$

**Proposition 14** (Local exponential convergence of  $\delta$ ). *If  $k_c^* > \frac{\omega_M}{\ell} \left( \frac{C_5}{2} + C_4 \right)$ , and under Assumption 3, there exists  $K_1 > 0$  and  $\lambda > 0$  such that*

$$\forall t \geq t_3, \min(\delta(q, \bar{q}), \delta(-q, \bar{q})) < K_1 \exp^{-\lambda(t-t_3)}$$

*Proof.* With the notations of Proposition 10, there exists  $l_2 > 0$  such that if  $\|\sigma(0)\| < \varepsilon'_a$ , one has

$$\forall t \geq 0, |\nabla T(q)^T(\mathbf{p}(u(q, \bar{q})) \otimes q)| \geq l_2$$

Using the expansions about  $q$  and  $-q$  (only the one about  $q$  is given below)

$$T(q) - T(\bar{q}) = \frac{\delta(\bar{q}, q)}{2} \nabla T(q)^T(\mathbf{p}(u(q, \bar{q})) \otimes q) + O(\delta(q, \bar{q})^2)$$

and noting<sup>3</sup> that

$$|\nabla T(\pm q)^T(\mathbf{p}(u(\pm q, \bar{q})) \otimes \pm q)| > l_2$$

one deduces that there exists  $0 < c < \varepsilon$  such that, if

$$\min(\delta(q, \bar{q}), \delta(-q, \bar{q})) < c$$

---

<sup>3</sup>more generally, one has

$$|\nabla T(\pm q)^T(\mathbf{p}(u(\pm q, \bar{q})) \otimes \pm q)| = |\nabla T(\pm q_\#)^T(\mathbf{p}(u(\pm q_\#, \bar{q})) \otimes \pm q_\#)| > l_2$$

then

$$(5.7.23) \quad \min(\delta(q, \bar{q}), \delta(-q, \bar{q})) < \frac{3|T(q) - T(\bar{q})|}{l_2}$$

From Proposition 13, there exist  $K' > 0$  and  $\lambda > 0$  such that

$$(5.7.24) \quad |T(q) - T(\bar{q})| < K' \exp^{-\lambda(t-t_3)}, \quad t \geq t_3$$

From Proposition 3 and (5.2.10), there exist  $t_4 > 0$  such that if  $t \geq t_4$ , then, using Assumption 3,

$$\min(\delta(q, \bar{q}), \delta(-q, \bar{q})) = \min(\delta(q, \bar{q}), \delta(-q, \bar{q}), \delta(q_{\#}, \bar{q}), \delta(-q_{\#}, \bar{q})) < c$$

Then, using Equation (5.7.23) and Equation (5.7.24), one has, for  $t \geq t_4$ ,

$$\min(\delta(q, \bar{q}), \delta(-q, \bar{q})) < K'' \exp(-\lambda(t - t_4))$$

with  $K'' = \frac{3K' \exp(-\lambda(t_4 - t_3))}{l_2}$ .

Invoking the continuous existence of the proposed observer over the bounded interval  $[t_3, t_4]$ , one can define an exponential bound  $K e^{-\lambda(t-t_3)}$  starting at  $t = t_3$ , by choosing  $K_1 > K'' \exp^{\lambda(t_4 - t_3)}$  such that

$$\forall t \geq t_3, \min(\delta(q, \bar{q}), \delta(-q, \bar{q})) < K_1 \exp^{-\lambda(t-t_3)}$$

This concludes the proof. □

### 5.7.3 Second case: Assumption 3 does not hold

In this case, from Proposition 9, one has directly that for all  $t \geq t_3$ ,

$$\min(\delta(q_{\#}, \bar{q}), \delta(-q_{\#}, \bar{q})) < \varepsilon$$

### 5.7.4 Conclusion of the proof

To summarize, we proved in the previous sections the following results :

Let us choose  $\varepsilon > 0$  such that for any  $t \geq 0$ , the  $\varepsilon$ -neighborhoods w.r.t. the  $\delta$  distance of  $q(t)$ ,  $-q(t)$ ,  $q_{\#}(t)$  or  $-q_{\#}(t)$  are four disjoint compact sets. There exists, thanks to Proposition 9 and Proposition 13,  $t_3 \geq 0$  and  $k_c^* > 0$  such that, if  $k_c > k_c^*$ , either

1. Assumption 3 is verified, and then, from Proposition 14, there exist  $K_1 > 0$  and  $\lambda > 0$  such that

$$\forall t \geq t_3, \min(\delta(q, \bar{q}), \delta(-q, \bar{q})) < K_1 \exp^{-\lambda(t-t_3)}$$

2. Assumption 3 is false, and then from Proposition 9,

$$\forall t \geq t_3, \min(\delta(q_{\#}, \bar{q}), \delta(-q_{\#}, \bar{q})) < \varepsilon$$

Invoking the continuous existence of the proposed observer over the bounded interval  $[0, t_3]$ , one can define an exponential bound  $Ke^{-\lambda t}$  starting at  $t = 0$ , by choosing  $K > K_1 \exp^{\lambda t_3}$  such that

$$\forall 0 \leq t \leq t_3, \min(\delta(q, \bar{q}), \delta(-q, \bar{q}), \delta(q_{\#}, \bar{q}), \delta(-q_{\#}, \bar{q})) < K \exp^{-\lambda t}$$

In the end, there exists  $\eta_2 = \varepsilon_b$  (as defined by Proposition 6), such that for  $\varepsilon > 0$  small enough, there exist  $\eta_1 = \min(\varepsilon_a, \varepsilon'_a)$  (as defined by Propositions 6 and 10) and  $k_{c*} > 0$ , such that, if  $\|\sigma(0)\| < \eta_1$ ,  $|T(q(0)) - T(\bar{q}(0))| < \eta_2$  and  $k_c > k_{c*}$ , then there exist  $K, \lambda > 0$  such that

$$\forall t \geq 0, \min(|\delta(q, q')|, |\delta(-q, q')|, |\delta(q_{\#}, q')|, |\delta(-q_{\#}, q')|) < \varepsilon + K \exp^{-\lambda t}.$$

This concludes the proof of Theorem 3.

## 5.8 Practical use of the main result

### 5.8.1 Observed asymptotic behavior

In Figure 5.8.1, we report the asymptotic behavior of the proposed observer for two typical initial conditions. It can be observed, as stated in Theorem 3, that the observer can converge to  $q$  or  $q_{\#}$ , almost as often. Indeed, if  $\sigma(0)$  is not small, it is not always true that  $\bar{q}$  remains for all times on one side of  $E_0$  (however, it quickly becomes true as  $\sigma$  decreases exponentially to zero independently of the other variables, see Proposition 6). Then, the destination point of the asymptotic behavior is difficult to predict.

### 5.8.2 Interpretation of the solution $q_{\#}$

Although  $q_{\#}$  yields the same pitch angle and magnetometer measurements as the actual attitude  $q$ , it does not correspond to the same rotation matrix. Fortunately, it is easy to discriminate if the output of the observer is the actual attitude  $q$  or the alternate solution  $q_{\#}$ , as the latter yields values of yaw angles that are commonly inconsistent with *a priori* knowledge of ballistics (e.g. corresponding to the projectile drifting to the opposite side of the expected Magnus effect induced by the rifled barrel, or flying backwards).

In details, this inconsistency depends on the orientation of  $b_0$  w.r.t. the shooting « plane ». Compared to  $q$ ,  $q_{\#}$  corresponds to a mirror attitude w.r.t.  $b_0$  having the same pitch angle. Then, a difficult to distinguish situation occurs when the angle between  $b_0$  and the shooting direction is small

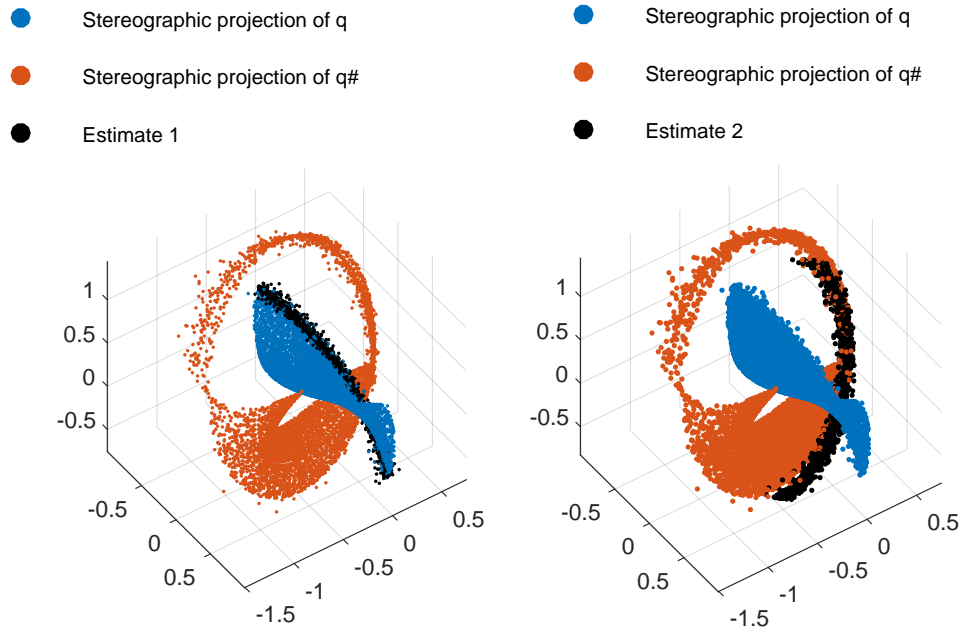


Figure 5.8.1: Stereographic representation of  $q$ ,  $q_{\#}$  and estimates  $\bar{q}$  from various initial conditions during the flight (only a short time horizon for the estimate is reported for clarity). Simulation results for a typical 155 mm flight.

(corresponding to a shot strictly towards the magnetic North), because the difference between the actual yaw angle and its symmetric associated with  $q_{\#}$  is small in such circumstances<sup>4</sup>.

For illustration, yaw angles associated with a typical reference attitude  $q$  and its counterpart  $q_{\#}$  are depicted in Figure 5.8.2, showing the latter can easily be discarded in practice because yaw angles in the  $-140$  deg range are clearly impossible.

### 5.8.3 Practical initialization to ensure convergence towards actual attitude

Proposition 6 informs us that for  $\sigma$  small enough, having  $\bar{q}(0) \in E_+$  is practically enough to ensure  $\bar{q}$  will remain in  $E_+$ . In practice, this suggests the following procedure: one just has to know whether  $q$  lies in  $E_+$  or  $E_-$  beforehand<sup>5</sup>, use the complementary filter (first two lines of the proposed

<sup>4</sup>one might argue that in this case the error has a limited impact on the attitude determination.

<sup>5</sup>for sake of simplicity, it has been assumed earlier that  $q$  lies in  $E_+$ , the converse case being treated in the same way.

observer) alone until  $\sigma$  is satisfyingly small, and then choose  $\chi(0)$  so that  $\bar{q}(0)$  obtained from  $\hat{q}(0)$  lies within the right set. In practice, belonging to  $E_+$  or  $E_-$  is easily verified, by determining the sign of (5.3.10). Figure 5.8.2 and Figure 5.8.3 show the yaw and pitch angles of several estimates initialized at  $\sigma = 0$  and various  $\chi(0)$ , compared to the yaw and pitch angles of the attitudes  $q$  and  $q_\#$ .

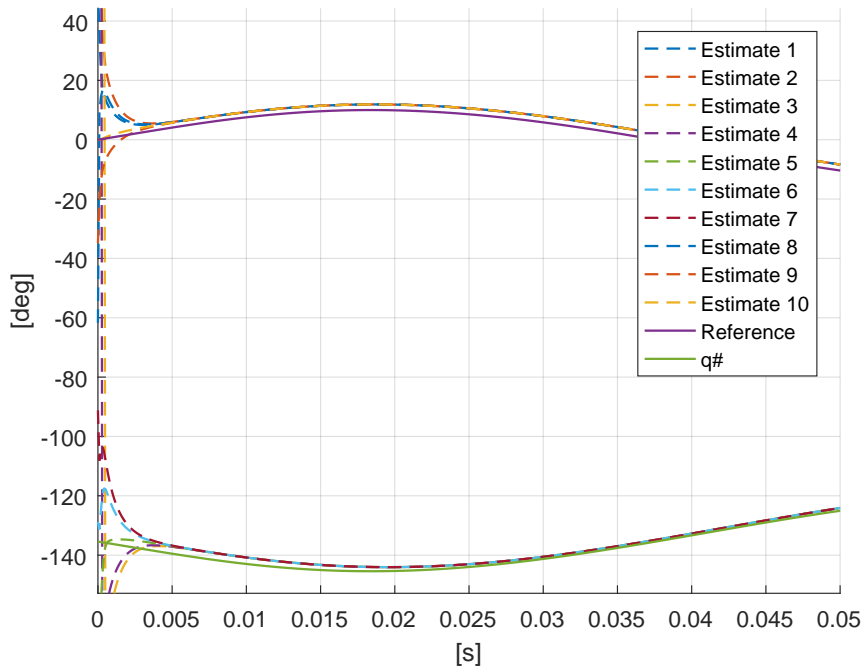


Figure 5.8.2: Yaw angle estimates from various (10) initializations during the early stage of the flight. Simulation results for a typical 155 mm shell.

Alternatively, if the observer has converged to  $q_\#$ , it is still possible to recover  $q$  from  $q_\#$  by applying the operator  $\cdot_\#$  (which is involutive) on the output. The result is not completely equivalent to an adequate initialization, since the asymptotic studies near  $q$  and  $q_\#$  differ, as made clear by Proposition 13 and 14 granting exponential stability outside of a neighborhood of  $q_\#$ .

## 5.9 Estimation results

To illustrate the merits of the proposed observer (5.4.1), we use data from simulation or experimental flights, with the additional pitch angle information provided using the simulator or the ground based position radar,

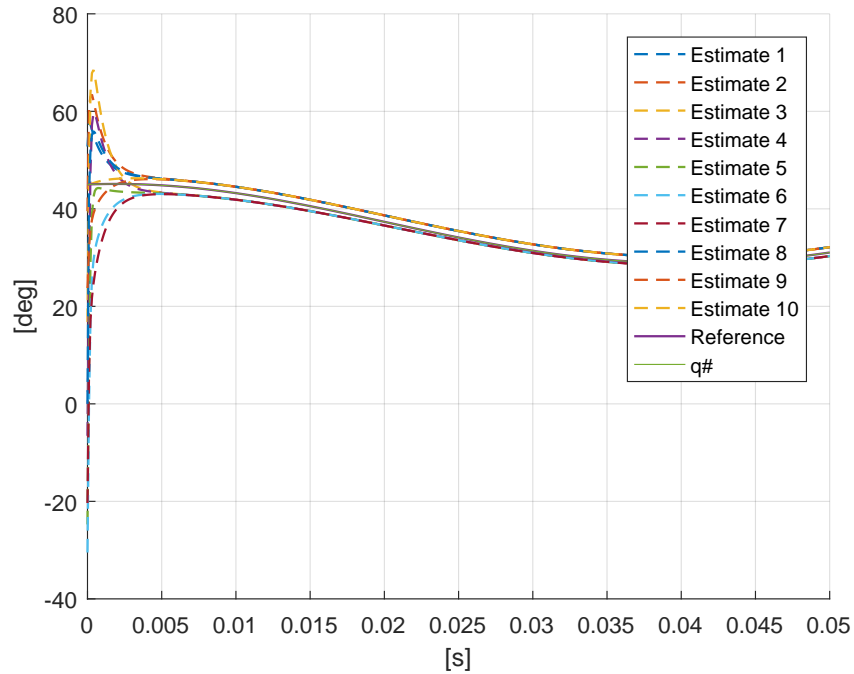


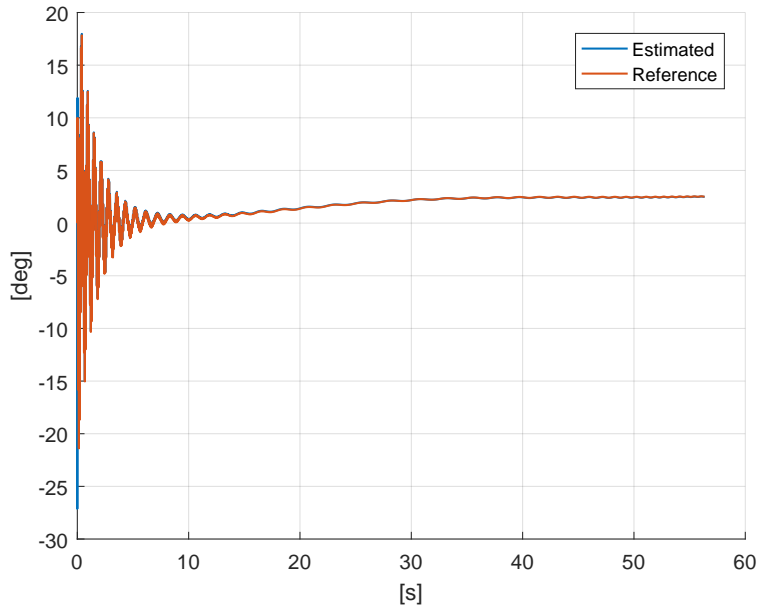
Figure 5.8.3: Pitch angles estimates from various (10) initializations during the early stage of the flight. Simulation results for a typical 155 mm shell.

respectively. The goal of this section is simply to illustrate the theoretical convergence of the proposed observer established in Theorem 3.

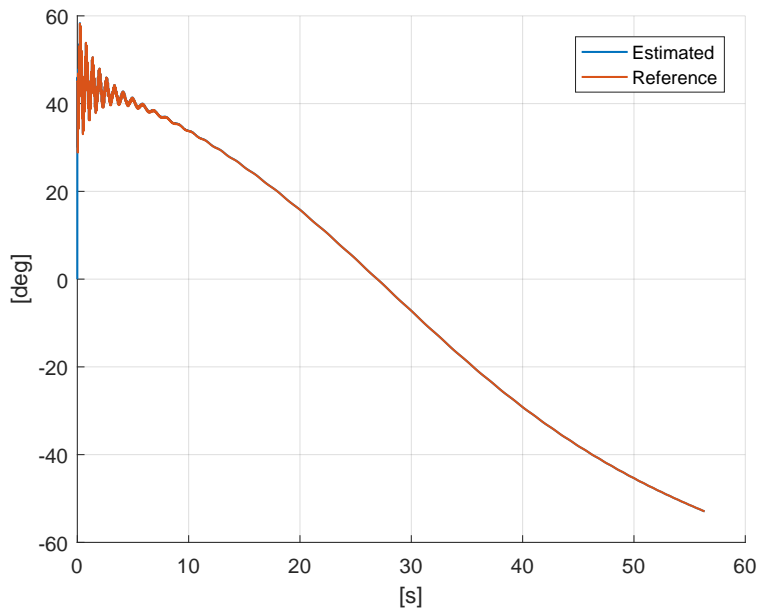
### 5.9.1 Simulation results

#### On 155 mm shell

We applied the observer of this chapter to the simulation data set 1 (see Table 2.8.1), using simulated pitch angle and simulated magnetometer and simulated angular velocity as inputs. As seen in Figures 5.9.1a and 5.9.1b, the estimated attitude yields satisfying estimation of the yaw and pitch angles. The roll angle is also well reconstructed, see Figure 5.9.2a. Additionally Figure 5.9.2b stresses that the estimated attitude is consistent with the magnetometer feedback, showing the convergence of the innovation of our observer to zero.



(a) Estimation of the yaw angle.



(b) Estimation of the pitch angle.

Figure 5.9.1: Estimation of attitude angles [155 mm shell simulation results].

### On Basic Finner

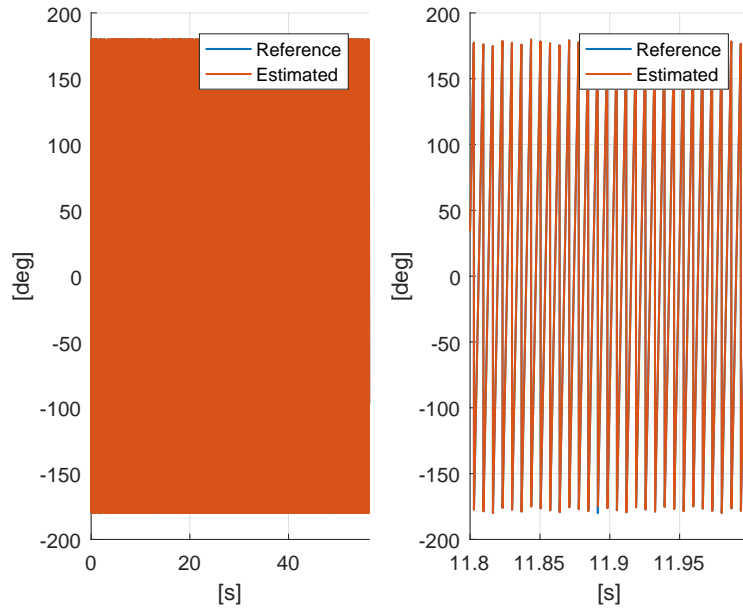
Similarly, we applied the proposed observer to the simulation data set 3, using simulated pitch angle and simulated magnetometer and simulated an-

gular velocity as inputs. The duration of the flight is much shorter than it is for a 155 mm shell. As illustrated in Figures 5.9.3a and 5.9.3b, the estimated attitude yields converging estimation of the yaw and pitch angles. The roll angle is also well reconstructed, see Figure 5.9.4a. Finally, Figure 5.9.4b shows that the estimated attitude is consistent with the magnetometer feedback.

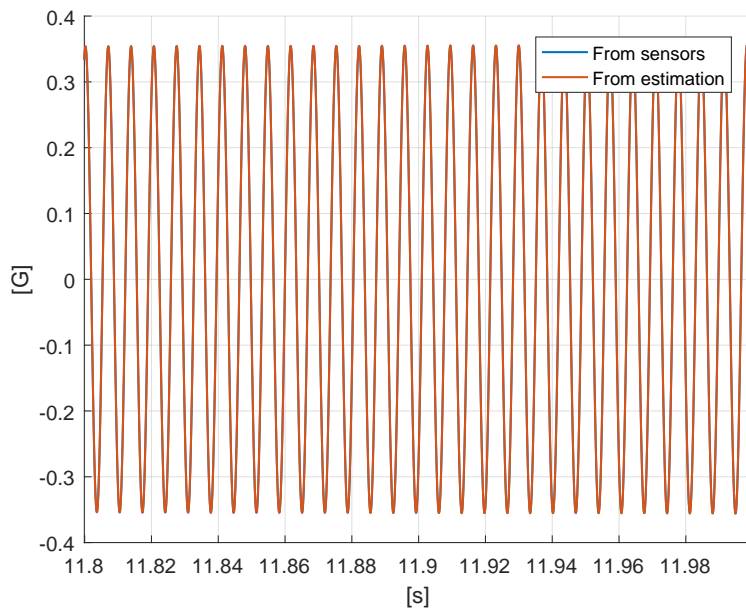
## 5.9.2 Experimental results

We applied the proposed observer to the experimental data set 2 (see Table 2.8.1), using as inputs a pitch angle estimator determined from the slope reference angle computed from the ground based position radar trajectory, a corrected magnetometer feedback (using the procedure procuding the results exposed in Figure 2.5.3), and an estimation of the spin rate (using the estimation results exposed in Figure 2.6.1b).

Figures 5.9.5a, 5.9.5b and 5.9.6a report the estimated attitude angles. Quite satisfying estimations of the yaw, pitch and roll angles are obtained. Additionally, Figure 5.9.6b shows that the estimated attitude is consistent with the magnetometer feedback.

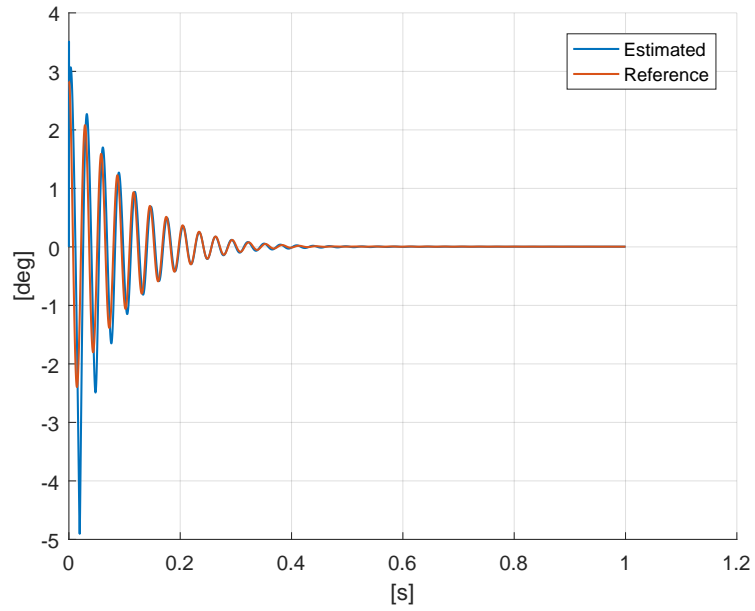


(a) Estimation of the roll angle (left: over the whole flight, right: zoom-in view). The spin rate and sampling rate are such that each sample is approximately 5 deg apart, hence the aliasing effect on the edges.

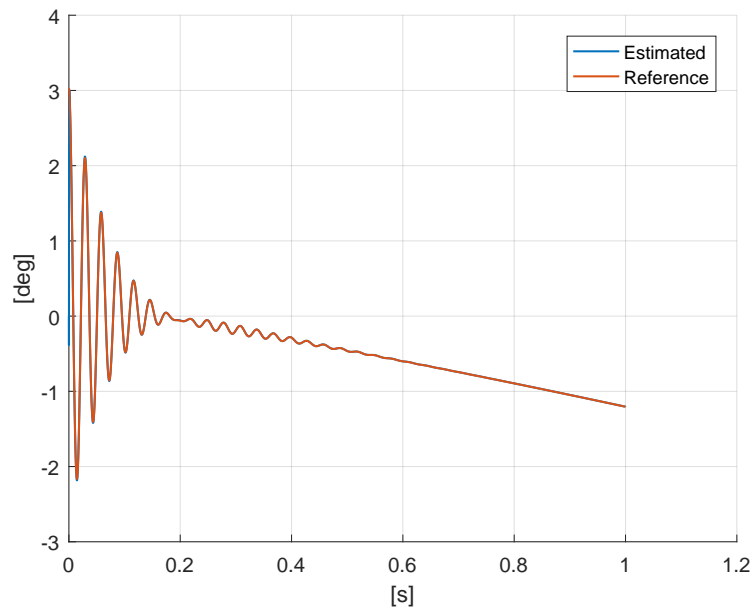


(b) Reconstitution of one magnetometer feedback from estimated attitude.

Figure 5.9.2: Estimation of roll angle and innovation [155 mm simulation results].

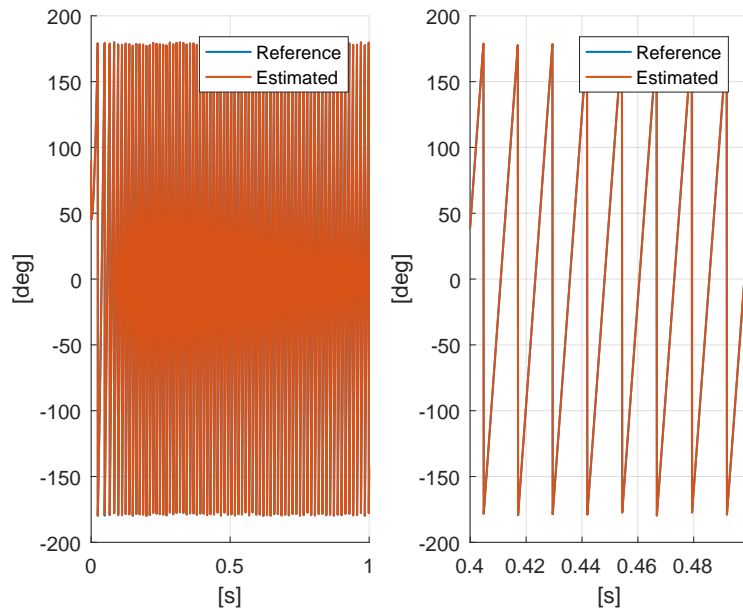


(a) Estimation of the yaw angle.

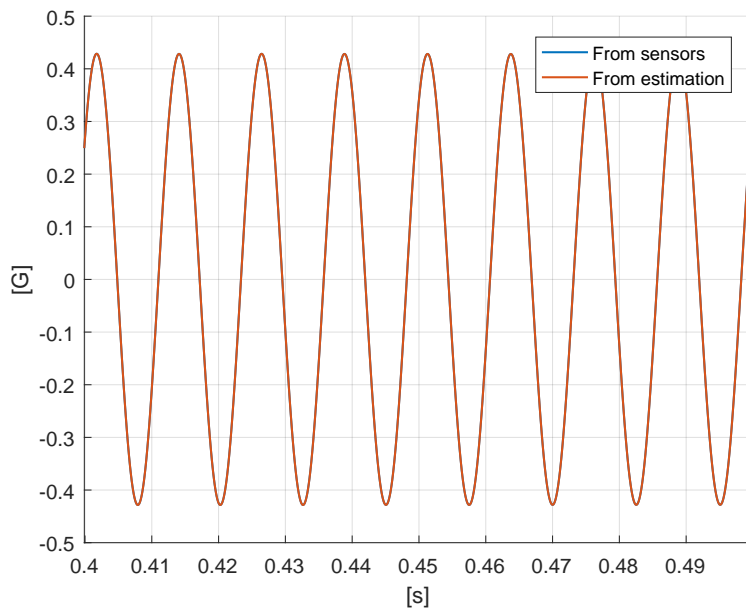


(b) Estimation of the pitch angle.

Figure 5.9.3: Estimation of attitude angles [Basic Finner simulation results].

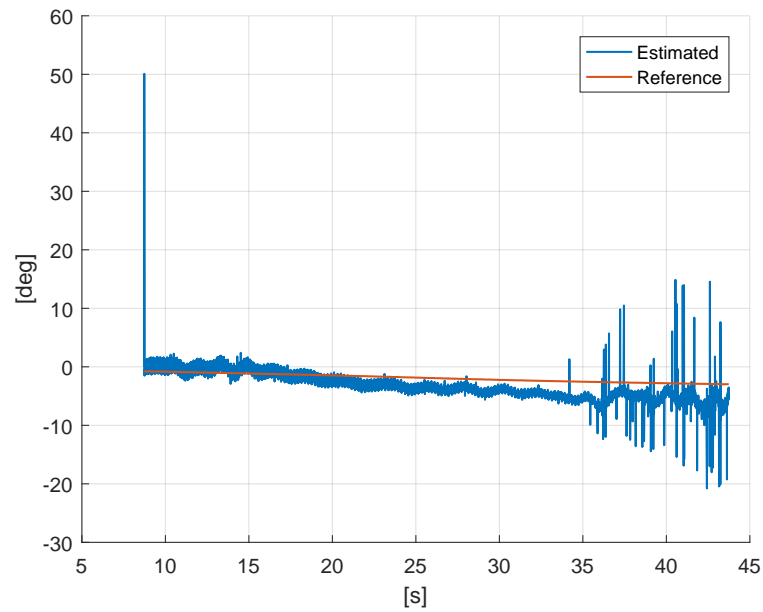


(a) Estimation of the roll angle (left: over the whole flight, right: zoom-in view).

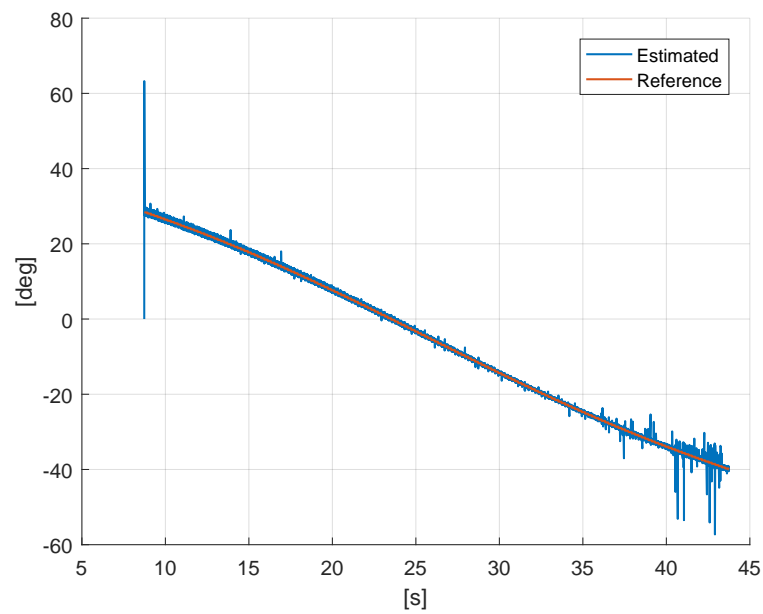


(b) Reconstitution of one magnetometer feedback from estimated attitude.

Figure 5.9.4: Estimation of roll angle and innovation [Basic Finner simulation results].

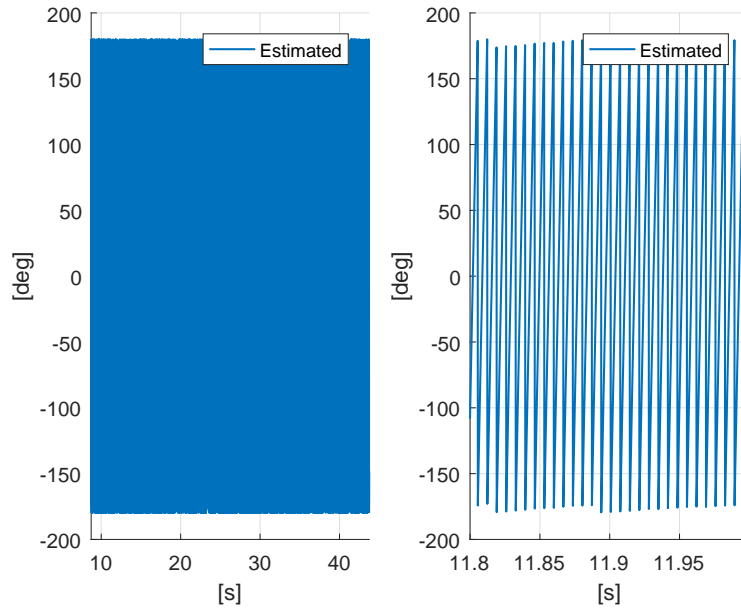


(a) Estimation of the yaw angle.

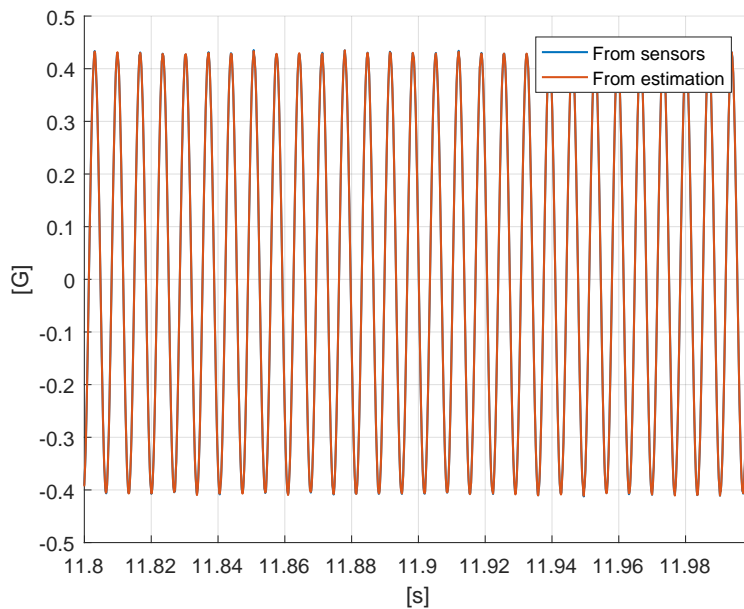


(b) Estimation of the pitch angle.

Figure 5.9.5: Estimation of attitude angles [experimental results on 155 mm, data set 2].



(a) Estimation of the roll angle (left: over the whole flight, right: zoom-in view)  
 The spin rate and sampling rate are such that each sample is approximately 5 deg apart, hence the aliasing effect on the edges.



(b) Reconstitution of one magnetometer feedback from estimated attitude.

Figure 5.9.6: Estimation of roll angle and innovation [experimental results on 155 mm, data set 2].



## Chapitre 6 - Résumé

Dans cet ultime chapitre, les différents estimateurs des chapitre 3, 4 et 5 sont rassemblés pour proposer une solution complète au problème posé, reposant exclusivement sur les mesures de capteurs embarqués. Plusieurs questions pratiques sont évoquées, les résultats des différents estimateurs constituant des mesures de moindre qualité que les mesures idéales utilisées dans les chapitres précédents. Plusieurs lissages intermédiaires sont ainsi présentés, dans le but de limiter la dégradation de performance logiquement attendue, et des résultats expérimentaux sont présentés.



## Chapter 6

# Experimental results of the proposed attitude observer using only on-board sensors

In this chapter, we present results obtained by exploiting data from on-board sensors only. We combine observers from Chapters 3, 4 and 5, following the process recalled in Figure 6.1.1. This approaches in in contrast to previous chapters in which each component of the complete observer was tested separately, using external reference signal such as ground based position radar. Velocity observer from Chapter 3 is used with one 1-axis transverse accelerometer feedback, which is used in the slope angle observer described in Chapter 4. This gives a pitch estimate, under the previously discussed zero incidence assumption. This information is then treated along with the 3-axis Magnetometer feedback through the attitude observer developed in Chapter 5.

### 6.1 Multirate Kalman filtering of frequency estimators

The estimators described in Section 3.3 are fused using a Kalman filter specifically implemented to account for this context of largely corrupted or incomplete measurements. According to observed noised on the estimates, the Kalman filter, which implements a simple  $f^{(3)} = 0$  dynamics, is tuned. When outliers are detected, they are discarded following the methodology exposed in [23] and exposed early in [50] where outliers are treated under the form of a change of the observation vector dimension.

On the 155 mm dataset 2 (real flight data), MUSIC turns out to be non

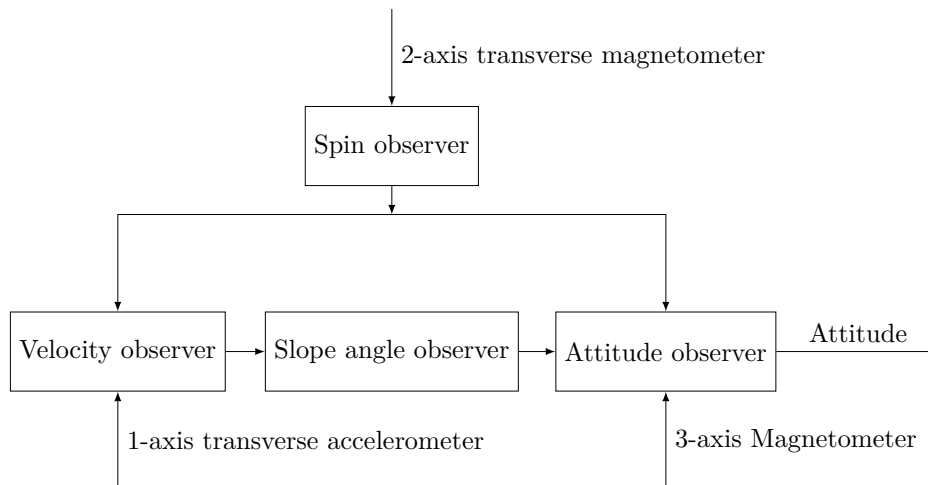


Figure 6.1.1: Attitude Estimation Algorithm from on-board sensors.

sufficiently robust. A possible explanation is the vast level of corruption of the measurements by the fictitious forces discussed in subsection 2.5.2. To illustrate this point, we report the signal-to-noise ratio of the 1-axis transverse accelerometer, as estimated from filtering, in Figure 6.1.2b. It is defined classically as

$$\text{SNR} = \frac{\text{mean}(s^2)}{\text{mean}(n^2)}$$

The estimate provided by MUSIC is of good quality up to some (relatively early) time when the algorithm fails to return a valid frequency estimate. The estimates are reported in Figure 6.1.2a. Compared to the quality of the other estimates discussed in Chapter 3, MUSIC seems not to add any useful information and is simply left out of the analysis. More details about the sensitivity of MUSIC w.r.t. SNR are given in Appendix B.3. This leaves us with 2 meaningful estimates to be fused.

The outcome of the fusion procedure is reported in Figure 6.1.3a, before and after a debiasing procedure we will detail in the next subsection.

## 6.2 Debiasing of the frequency estimate

The frequency estimate is then de-biased as follows. There is a one-to-one mapping (referred to as « velocity model » below) between the frequency and the shell velocity with respect to the air, as discussed in Chapter 4. The instant when the shell reaches Mach 1 is easily detected on the longitudinal accelerometer, under the form of a sudden jump of the signal. We now recall elements from § 3.5.1. Comparing the value of 317.8 m/s obtained from the

frequency estimate through the velocity model with Mach 1 (332 m/s)<sup>1</sup>, we deduce that our velocity estimate is biased (at this particular instant) by  $\approx 13.2$  m/s. Applying the inverse of the velocity model, we deduce our frequency estimate is biased by  $\approx 2$  Hz, and decide to apply a constant bias correction over the whole time interval. The result of this bias correction is reported in Figure 6.1.3a. Then, the de-biased frequency estimate is used through the velocity model to produce a velocity estimate  $v_e$ .

### 6.3 Smoothing under convexity constraints

As can be observed in Figure 6.1.3b, the estimate  $v_e$  has values close to the reference measurements provided by the ground based position radar (within the confidence interval of  $\pm 15$  m/s close to observed wind velocity at Mach 1). However, this estimate lacks a desirable property in view of estimating the slope angle: its derivative is not smooth enough.

To address this problem,  $v_e$  is filtered once again using a moving horizon constrained optimization procedure, following the constrained estimation methodology presented in [79] (among others). This discrete-time approach aims at combining the  $v^{(3)} = 0$  model with the extra assumption that  $v^{(2)} \geq 0$ , which is a known property of the flight (the velocity w.r.t the local frame being a convex function of time). The details of the implementation are given in Appendix B.2. This produces an estimate  $v_m$  which is reported in Figure 6.1.3b. The estimate is significantly smoother, at the expense of a bias, which has no real impact on the slope estimation.

### 6.4 Slope and pitch estimation experimental results

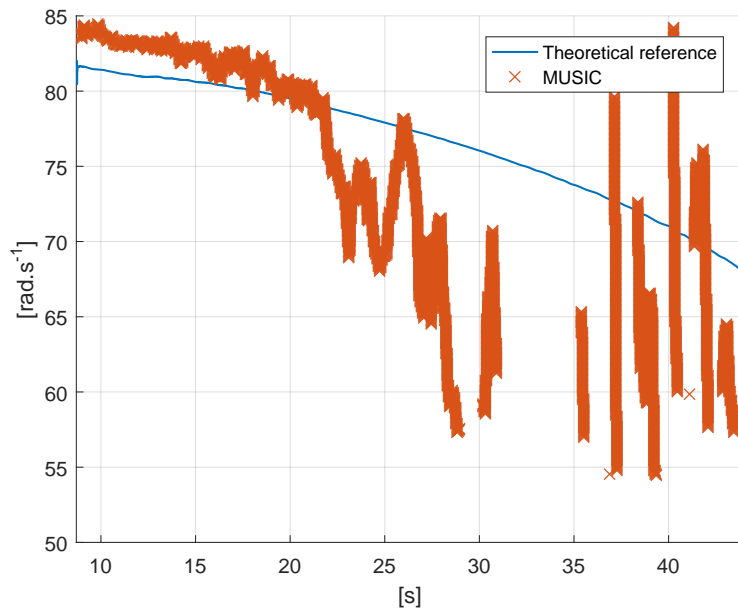
The implementation of the slope and pitch estimation are reported in Figure 6.4.1. The kind accordance with the reference obtained from the ground based position radar can be observed in Figure 6.4.1, although some final errors can be noted, most likely due to difficulties in obtaining reliable frequency estimates during the final stages of the flight.

---

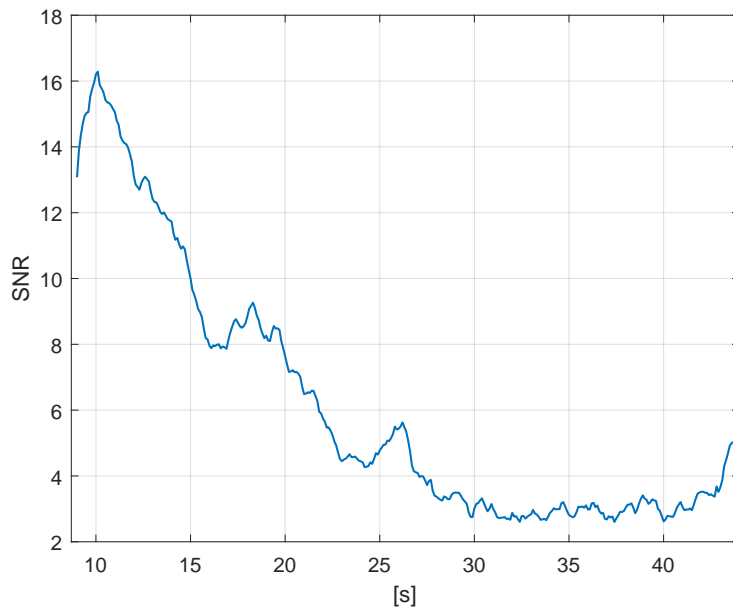
<sup>1</sup>assuming the altitude is equal to the reference altitude for such a 155 mm fired at nominal speed, which is corroborated by the ground based position radar measurements for sake of completeness.

## 6.5 Attitude observer results

The attitude observer from Chapter 5 is used with the previously reported pitch estimate and the measurements of the 3-axis Magnetometer. The results are reported in Figures 6.5.1a, 6.5.1b and 6.5.2a. The estimates are converging. Some level of noise and outliers can be seen propagating in the estimates. At the the very end of the time interval the error observed in Figure 4.1.5 corrupts the Yaw estimate (see Figure 5.9.5a). For completeness, Figure 6.5.2b reports that the innovation of the attitude observer converges to zero, the attitude estimation yielding a magnetic field measurement matching the real magnetometer output.

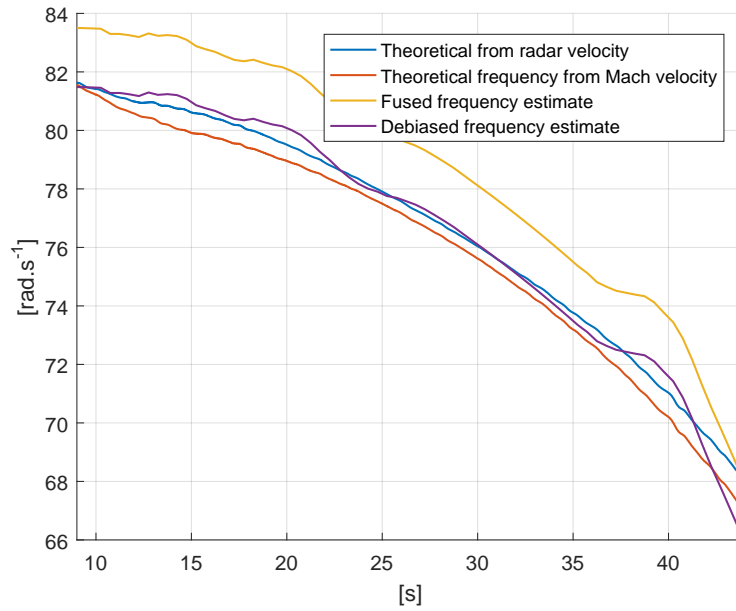


(a) Frequency identification against theoretical frequencies.

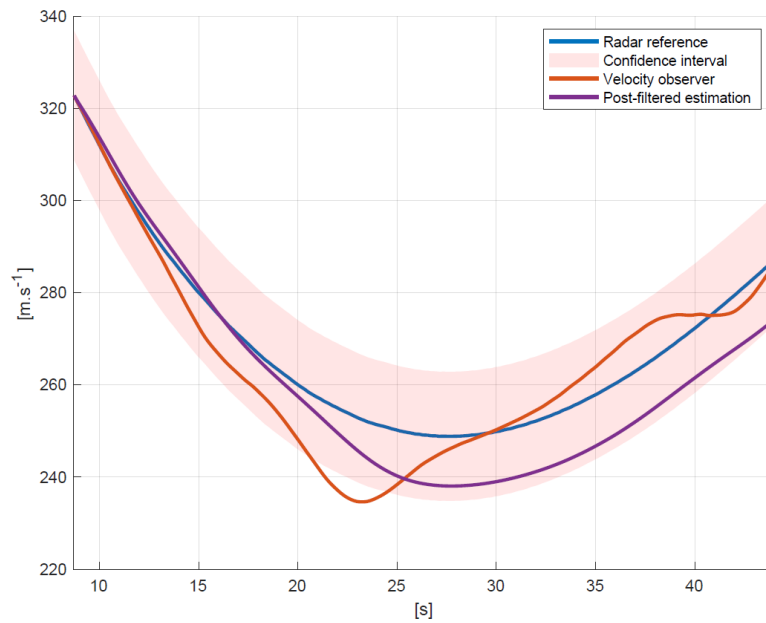


(b) Signal/noise ratio.  $10 \cdot \log_{10}$  SNR is reported.

Figure 6.1.2: Experiments with MUSIC on dataset 2 [experimental results].



(a) Frequency Estimation [experimental results].



(b) Velocity Estimation [experimental results].

Figure 6.1.3: Frequency and velocity estimates [experimental results].

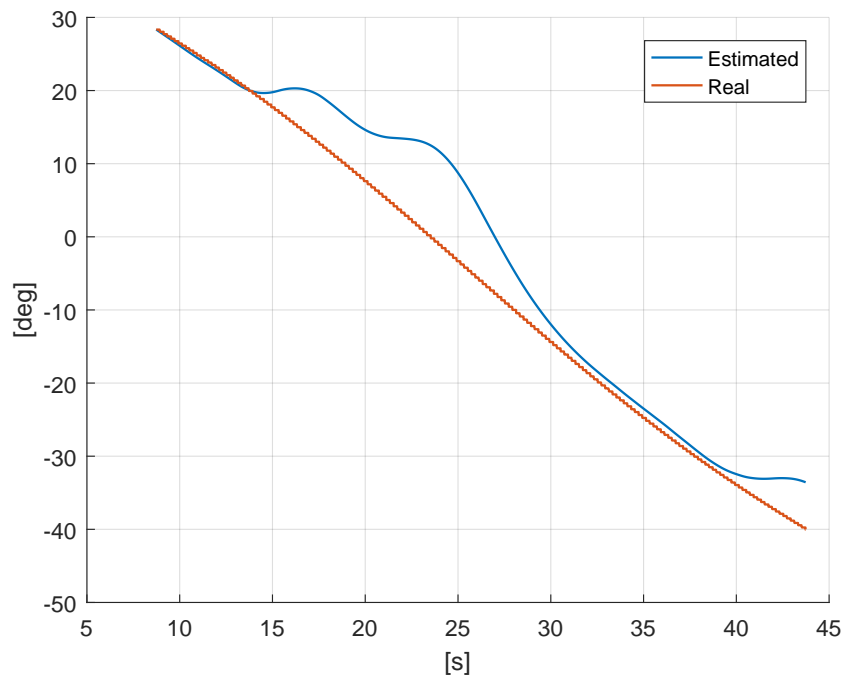
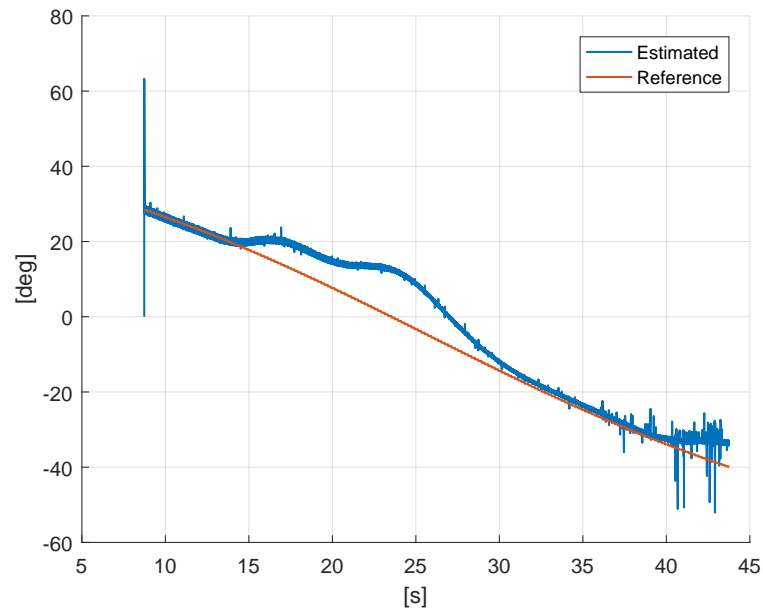
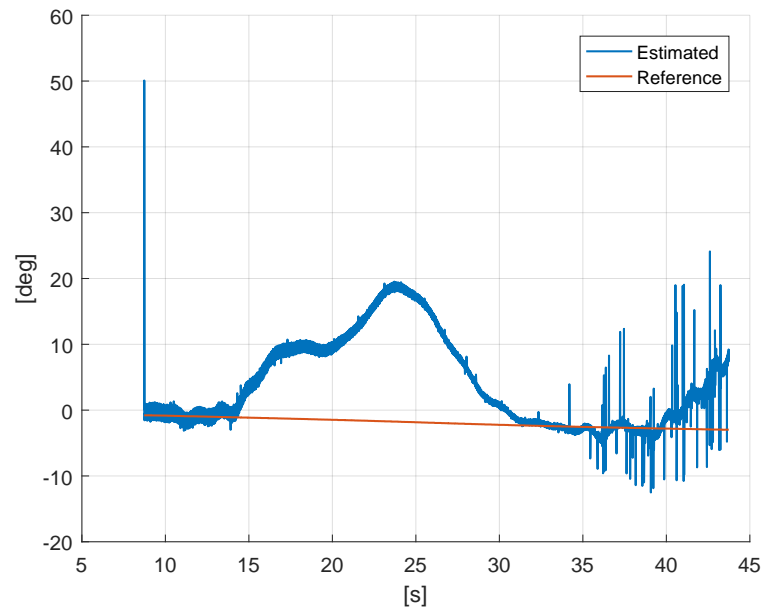


Figure 6.4.1: Estimation of the slope angle [experimental results].

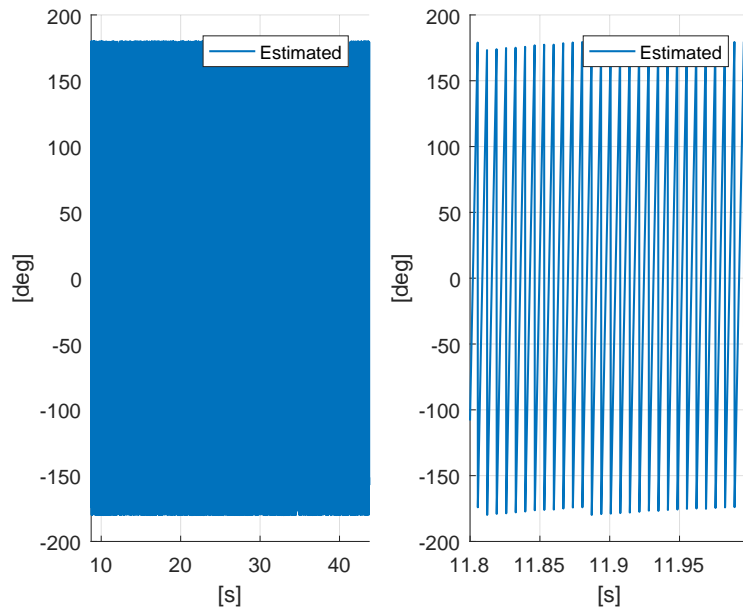


(a) Estimation of the pitch angle [experimental results].

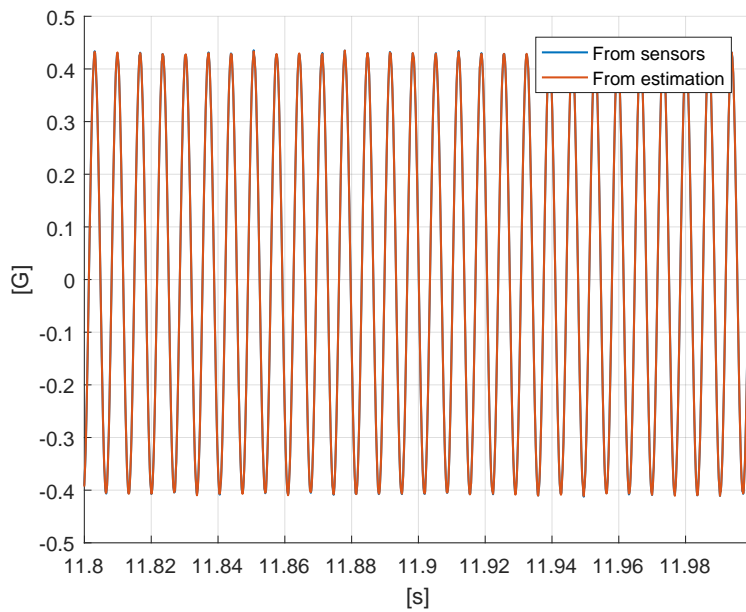


(b) Estimation of the yaw angle [experimental results].

Figure 6.5.1: Attitude angle estimates [experimental results].



(a) Estimation of the roll angle [experimental results].



(b) Reconstitution of one magnetometer feedback from estimated attitude [experimental results].

Figure 6.5.2: Roll estimate and innovation [experimental results].



## Chapitre 7 - Résumé

On conclut ici notre étude en présentant quelques perspectives et pistes de recherches futures. La possible exploitation du magnétomètre pour la détection des fréquences de précession et nutation peut laisser entrevoir une méthode sans accéléromètres. L'extraction fréquentielle à proprement parler est également une des améliorations les plus prometteuses, sa précision ayant un impact considérable sur celle de l'estimation d'attitude finale. On rappelle également les bons résultats des différents estimateurs pris indépendamment, et leurs applications possibles, complétés par d'autres capteurs ou des mesures externes transmises par télémétrie. Enfin, on évoque les autres utilisations possibles de l'approche fréquentielle : accompagnée *a posteriori* de mesures radars, elle peut en effet permettre d'estimer certains des paramètres du modèle aérodynamique utilisé dans cette thèse.



## Chapter 7

# Conclusion and perspectives

As claimed in the introduction of this thesis, we have offered an efficient method to estimate the attitude of an artillery shell in free-flight, using solely a 3-axis Magnetometer and one transverse 1-axis accelerometer. Simulation and experimental results have been presented, and comparisons with high-fidelity measurements from a ground based position radar are provided. The particularly challenging case of gyrostabilized shells has been covered.

On the hardware side, it is worth noting that the transverse accelerometer is solely used to extract the frequency corresponding to the epicyclic modes of its oscillating motion. Theory teaches us that these frequencies should also be present in the 3-axis Magnetometer feedback. This has not been exploited in practice, since the high level of noise in this signal made it more difficult to deal with than the transverse accelerometer. However, this could be a valuable alternative as it would allow one to reduce the number of on-board sensors, performing attitude estimation from a 3-axis Magnetometer only. To tamper this, it should be considered that other flight analysis tasks such as incidence estimation, carried out when using aerodynamic coefficients with greater accuracy, and useful to provide a better angular rate estimation, would still require 2-axis of transverse accelerometer (the results we have shown in this thesis do not include incidence estimation).

Concerning main leads of improvement on the algorithm side, one can note that the frequency extraction techniques presented in the thesis are mostly « off-the-shelve ». Improving them or using custom-designs ones would certainly have a great impact on the accuracy of the attitude estimation (by improving velocity and slope angle estimation).

Concerning other applications, Chapter 3, 4 and 5 can still be used independently, with very promising results. By adding radar measurement with telemetry, many applications may be possible, not necessarily « on-board only ». As examples, the knowledge of the velocity from radar measure-

ments transmitted on board would make it possible to carry out slope angle estimation and attitude estimation using only, without the difficulty of frequency measurement. Velocity estimation with frequency analysis has a lot of applications (incidence estimation, using aerodynamics with better accuracy, among others), and so on. One should keep in mind that even though telemetry from a ground station is feasible, its operational use would be costly and difficult to implement, and on-board solutions are still the safest bet when it comes to future perspectives.

Finally, the frequency detection approach is used as a way to estimate the velocity, both as a requirement to make full use of the aerodynamic model of the shell and a prerequisite to the slope angle estimation. But the frequency analysis holds more information (even more so as soon as one is able to measure the precession and nutation amplitudes as well). The frequency analysis could be used *a posteriori* with a radar measurement of the velocity and the best-known aerodynamic coefficients (namely, the Drag and the Lift coefficient), to refine the models which are known to suffer from a great level of uncertainty, namely look-up tables concerning the Magnus moment, the overturning moment and the pitch-damping moment, using (3.2.1) and (3.2.2).

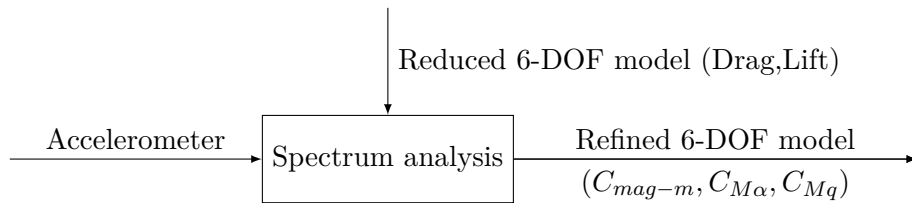


Figure 7.0.1: Toward a reduced aerodynamic model through low frequency analysis.

### Achieved and upcoming publications

The velocity estimation method described in Chapter 3 has led to two conference papers, a practical one presented at the American Institute of Aeronautics and Astronautics’s SciTech Forum in 2018 [36], and a theoretical one presented at the 2018 edition of the Conference on Decision and Control [37]. As a side result, an article has also been written on gyroless attitude estimation, using vector measurements to estimate angular velocity and replacing gyrometer measurements with this estimation in classical complementary filtering. This article has been presented at the European Conference on Control in 2019 [38].

Finally, we believe the content of Chapter 5 could provide for a theoretical article on attitude estimation from one vector measurement and one

angle input. The practical method described in Chapter 6 could be adapted into a more « application-oriented » article referring to past publications describing the various estimation method used. The redaction of those two articles is currently well underway, to conclude the work conducted during this thesis.



# Appendix A

## Supplementary material

### A.1 Transition matrices

The attitude matrix  $R$  from the body frame to the local frame can be decomposed as follows :

$$(A.1.1) \quad R = \begin{pmatrix} \cos \Psi & -\sin \Psi & 0 \\ \sin \Psi & \cos \Psi & 0 \\ 0 & 0 & 1 \end{pmatrix} \begin{pmatrix} \cos \Theta & 0 & \sin \Theta \\ 0 & 1 & 0 \\ -\sin \Theta & 0 & \cos \Theta \end{pmatrix} \begin{pmatrix} 1 & 0 & 0 \\ 0 & \cos \Phi & -\sin \Phi \\ 0 & \sin \Phi & \cos \Phi \end{pmatrix}$$

which yields

$$(A.1.2) \quad R = \begin{pmatrix} \cos \Psi \cos \Theta & \cos \Psi \sin \Theta \sin \Phi - \sin \Psi \cos \Phi & \cos \Psi \sin \Theta \cos \Phi + \sin \Psi \sin \Theta \\ \sin \Psi \cos \Theta & \sin \Psi \sin \Theta \sin \Phi + \cos \Psi \cos \Phi & \sin \Psi \sin \Theta \cos \Phi - \cos \Psi \sin \Theta \\ -\sin \Theta & \cos \Theta \sin \Phi & \cos \Theta \cos \Phi \end{pmatrix}$$

The attack angle  $\alpha$  and the sideslip angle  $\beta$  are defined by the relation :

$$(A.1.3) \quad [T]^{BW} = [T(-\alpha)][T(\beta)]$$

with

$$(A.1.4) \quad [T(\alpha)] = \begin{pmatrix} \cos \alpha & 0 & \sin \alpha \\ 0 & 1 & 0 \\ -\sin \alpha & 0 & \cos \alpha \end{pmatrix}$$

$$(A.1.5) \quad [T(\beta)] = \begin{pmatrix} \cos \beta & -\sin \beta & 0 \\ \sin \beta & \cos \beta & 0 \\ 0 & 0 & 1 \end{pmatrix}$$

which yields

$$(A.1.6) \quad [T]^{BW} = \begin{pmatrix} \cos \alpha \cos \beta & -\cos \alpha \sin \beta & -\sin \alpha \\ \sin \beta & \cos \beta & 0 \\ \sin \alpha \cos \beta & -\sin \alpha \sin \beta & \cos \alpha \end{pmatrix}$$

## A.2 Alternative angles

$\eta$	Slope angle
$\theta$	Azimuth angle
$\alpha_2$	Attack angle
$\beta_2$	Sideslip angle
$\phi_2$	Roll angle
$\alpha_t$	Total angle of attack of the shell (angle between vectors $1^B$ and $V$ )

Table A.2.1: Nomenclature.

In addition to the local (inertial) frame  $L$  and the body  $B$  frame, a third frame is considered and referred to as the « wind velocity frame », denoted  $W$ . It is defined from the body frame with the velocity of the shell with respect to the airflow, denoted  $v_B^A$ .

The angles are defined by (A.2.2).

$$(A.2.1) \quad [T]^{LW} = R_{\eta, e_3} R_{\theta, e_2}$$

$$(A.2.2) \quad [T]^{WB} = R_{\beta_2, e_3} R_{\alpha_2, e_2} R_{\phi_2, e_1}$$

Noting that the velocity w.r.t. the airflow in the body frame both satisfies

$$(A.2.3) \quad [v_B^A]^B = V \begin{pmatrix} \cos \alpha \cos \beta \\ \sin \beta \\ \sin \alpha \cos \beta \end{pmatrix}$$

and

$$(A.2.4) \quad [v_B^A]^B = V \begin{pmatrix} 1 & 0 & 0 \\ 0 & \cos \phi_2 & \sin \phi_2 \\ 0 & -\sin \phi_2 & \cos \phi_2 \end{pmatrix} \begin{pmatrix} \cos \alpha_2 \cos \beta_2 \\ -\sin \alpha_2 \cos \beta_2 \\ -\sin \beta_2 \end{pmatrix}$$

we get, under the assumption that the total angle of attack is small, the following relation between both sets of incidence angles :

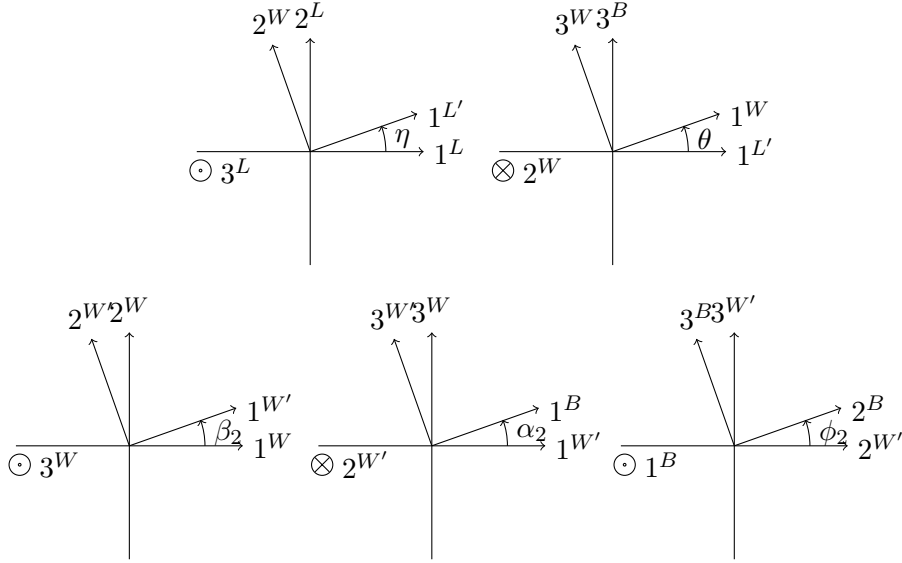


Figure A.2.1: Definition of Tait-Bryan and incidence angles

$$(A.2.5) \quad \begin{cases} \alpha \simeq \sin(pt) \alpha_2 - \cos(pt) \beta_2 \\ \beta \simeq -\cos(pt) \alpha_2 - \sin(pt) \beta_2 \end{cases}$$

The angles between the frames  $L$ ,  $B$  and  $W$  are illustrated in Figure A.2.1.

### A.3 Approximation on the shell velocity

In this section, we will detail the various approximations leading to (2.4.1).

$$(A.3.1) \quad \begin{cases} \dot{v} = -\frac{\rho S \tilde{C}_D v^2}{2M} - g \sin \theta \\ \dot{h} = v \sin \theta \end{cases}$$

We start by applying Newton's second law in the local frame, thus considering the velocity w.r.t. the local frame  $v_B^L$ ; we will show under which approximations this lead to a simpler equation on  $v$ , the velocity of the shell w.r.t. the airflow.

In the following, the notation  $\frac{\partial^L}{\partial t}$  will refer to the derivative with respect to time of a vector expressed in the local frame  $L$ . We define in an analogous manner  $\frac{\partial^B}{\partial t}$  if said vector is expressed in the body frame  $B$ .

Newton's second law in the local frame gives

$$(A.3.2) \quad M \frac{\partial^L v_B^L}{\partial t} = \sum F_{\text{ext}} - 2M[\omega_L^I]v_b^L$$

yielding

$$(A.3.3) \quad \frac{\partial^B v_B^L}{\partial t} = \frac{1}{M} \sum F_{\text{ext}} - 2[\omega_L^I]v_B^L - [\omega_B^L]v_B^L$$

The angular velocity of the shell w.r.t. the inertial frame  $\omega_B^I$  appears

$$(A.3.4) \quad \frac{\partial^B v_B^L}{\partial t} = \frac{1}{M} \sum F_{\text{ext}} - [\omega_L^I]v_B^L - [\omega_B^I]v_B^L$$

Most forces being function of the velocity of the shell w.r.t. the wind  $v_B^A$ , (A.3.4) can be rewritten as such :

$$(A.3.5) \quad \frac{\partial^B v_B^A}{\partial t} = \frac{1}{M} \sum F_{\text{ext}} - [\omega_L^I]v_B^A - [\omega_B^I]v_B^A + \mathbf{c}$$

with a corrective term coming from the wind velocity :

$$(A.3.6) \quad \mathbf{c} = - \left[ \frac{\partial^B (v_A^L + [\omega_A^L]p_B^A)}{\partial t} \right] - [\omega_B^I] (v_A^L + [\omega_A^L]p_B^A) - [\omega_L^I] (v_A^L + [\omega_A^L]p_B^A)$$

In the case of zero wind,  $\mathbf{c}$  is obviously zero.

Neglecting Coriolis force and the impact of the wind, one still has to express the gravity vector in the body frame :

$$(A.3.7) \quad [\vec{g}]^B = g \begin{pmatrix} -\sin \theta & \cos \theta \sin \Phi & \cos \theta \cos \Phi \end{pmatrix}^T$$

The velocity w.r.t. the wind can be expressed with the incidence angles as such, on the first order regarding those :

$$(A.3.8) \quad [v_B^A]^B = \begin{pmatrix} v \cos \alpha \cos \beta \\ v \sin \beta \\ v \sin \alpha \cos \beta \end{pmatrix} \simeq \begin{pmatrix} v \\ v\beta \\ v\alpha \end{pmatrix}$$

This yields, keeping only order 1 terms in  $\alpha, \beta$  :

$$(A.3.9) \quad \dot{v} = -\frac{\rho S \tilde{C}_D v^2}{2M} - g \sin \theta + g (\beta \cos \theta \sin \Phi + \alpha \cos \theta \cos \Phi)$$

Neglecting the total angle of attack finally leads to (2.4.1) considered in the thesis.

## A.4 Material for Chapter 3

Figure A.4.1 and Figure A.4.2 illustrate the impact of the temperature model w.r.t. the altitude on the velocity estimation conducted in Chapter 3.

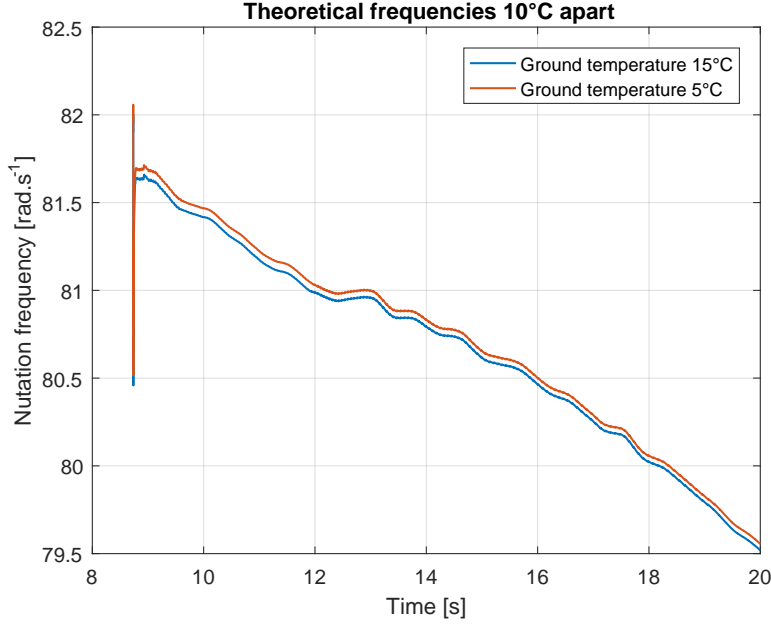


Figure A.4.1: Theoretical frequencies for two ground temperature [experimental results]; initial apparent outliers come from the spin rate estimation which does not converge immediately.

## A.5 Calculations leading to $q_{\#}$ expression in Chapter 5

As discussed in Chapter 5, an immediate solution of (5.3.4) is  $q_f = q$ ; what are the others? The parametrization (5.3.6) gives the answer to this question. Given that

$$(A.5.1) \quad \begin{cases} b_0 \triangleq [a \ b \ c]^T \\ q_t = (\cos t) q + (\sin t) (\mathbf{p}(b_0) \otimes q) \end{cases}$$

One has, using

$$q_t = \begin{pmatrix} q_1 \cos t + (-aq_2 - bq_3 - cq_4) \sin t \\ q_2 \cos t + (aq_1 - cq_3 + bq_4) \sin t \\ q_3 \cos t + (bq_1 + cq_2 - aq_4) \sin t \\ q_4 \cos t + (cq_1 - bq_2 + aq_3) \sin t \end{pmatrix}$$

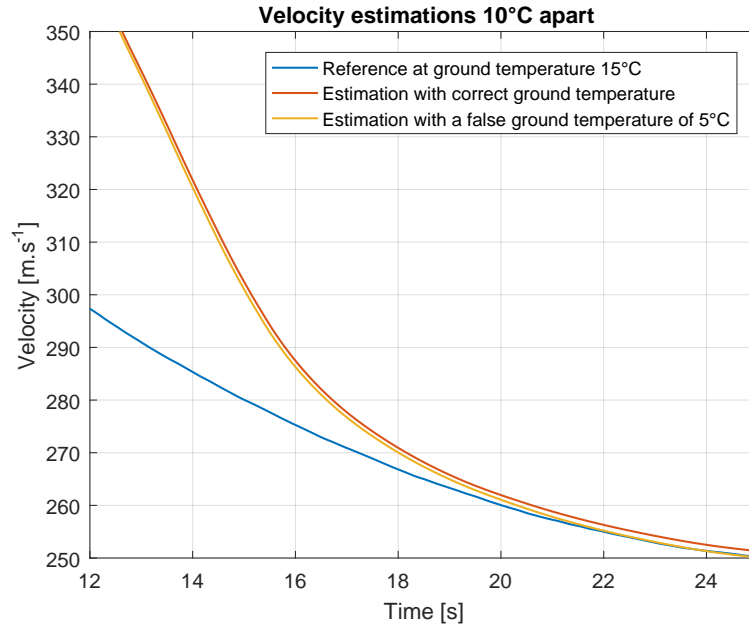


Figure A.4.2: Velocity Estimations with a temperature error [experimental results].

and

$$T(q) = q_1 q_3 - q_2 q_4$$

the following :

$$\begin{aligned}
 (A.5.2) \quad T(q_t) = & (\cos t)^2 q_1 q_3 \\
 & + (\cos t \sin t) \left( b q_1^2 + c q_1 q_2 - a q_1 q_4 - a q_2 q_3 - b q_3^2 - c q_3 q_4 \right) \\
 & + (\sin t)^2 \left( -a b q_1 q_2 - a c q_2^2 + a^2 q_2 q_4 - b^2 q_1 q_3 - b c q_2 q_3 \right. \\
 & \left. + a b q_3 q_4 - b c q_1 q_4 - c^2 q_2 q_4 + a c q_4^2 \right) \\
 & - (\cos t)^2 q_2 q_4 \\
 & - (\cos t \sin t) \left( c q_1 q_2 - b q_2^2 + a q_2 q_3 + a q_1 q_4 - c q_3 q_4 + b q_4^2 \right) \\
 & - (\sin t)^2 \left( a c q_1^2 - a b q_1 q_2 + a^2 q_1 q_3 - c^2 q_1 q_3 + b c q_2 q_3 \right. \\
 & \left. - a c q_3^2 + b c q_1 q_4 - b^2 q_2 q_4 + a b q_3 q_4 \right)
 \end{aligned}$$

This simplifies into

$$(A.5.3) \quad T(q_t) = (\cos^2 t)T(q) + (\cos t \sin t) \left( b(1 - 2(q_3^2 + q_4^2)) - 2a(q_1q_4 + q_2q_3) \right) + (\sin^2 t)(-ac(1 - 2(q_3^2 + q_4^2)) - 2bc(q_1q_4 + q_2q_3)) + (\sin^2 t)(c^2 - a^2 - b^2)T(q)$$

and finally

$$T(q_t) = (\cos^2 t)T(q) + (\cos t \sin t)(bT_3(q) - 2aT_2(q)) + (\sin^2 t)(-acT_3(q) - 2bcT_2(q)) + (\sin^2 t)(c^2 - a^2 - b^2)T(q)$$

We would like to solve, for  $t \in [0, 2\pi[$  the equation

$$(A.5.4) \quad T(q) = T(q_t)$$

If we discard the obvious solutions  $t = 0$  and  $t = \pi$  corresponding to  $q_t = q$  and  $q_t = -q$ , one has, using  $1 - \cos^2 t = \sin^2 t$  and simplifying per  $\sin t \neq 0$ , the following equality :

$$(A.5.5) \quad \cos t(-bT_3(q) + 2aT_2(q)) = \sin t \left( (1 - c^2 + a^2 + b^2)T(q) + acT_3(q) + 2bcT_2(q) \right)$$

yielding a unique solution in  $] -\pi/2\pi/2[$  :

$$(A.5.6) \quad t_{\#} = \arctan \left( \frac{bT_3(q) - 2aT_2(q)}{2(a^2 + b^2)T(q) + acT_3(q) + 2bcT_2(q)} \right)$$

yielding  $q_t \triangleq q_{\#}$ , and another  $(t_{\#} \pm \pi)$  corresponding to  $q_t = -q_{\#}$ .

## A.6 An equivalence property for Chapter 5

Section 5.3.2 made it clear that a neighborhood regarding  $\sigma$  and  $T$  corresponds to some neighborhoods regarding the distance  $\delta$ . To ensure our observer converges exponentially, one need to quantitatively relate the sizes of those neighborhoods. This will be the focus of the following properties. In the following  $\mathcal{B}(\cdot)$  refer to Euclidean balls.

**Proposition 15.** *Consider  $f : \mathbb{R}^4 \rightarrow \mathbb{R}^4, x \mapsto (f_1(x), f_2(x)) \triangleq \|x\| - 1$  where  $f_1$  is a smooth function and  $f$  having a finite number  $n_z$  of zeros noted  $x_0^i, f(x_0^i) = 0, i = 1, \dots, n_z$ . Assume that  $D_f(x_0^i)$  is full rank for  $i = 1, \dots, n_z$ . Then, for  $c > 0$  small enough the level set  $\mathcal{L}_c \triangleq \{x \text{ s.t. } \|f_1(x)\| = c, f_2(x) = 0\}$  is a subset of*

$$\bigcup_{i=1, \dots, n_z} \mathcal{B}(x_0^i, 2c/\rho_{min})$$

where  $\rho_{min} \neq 0$  is the smallest singular value of all the  $D_f(x_0^i), i = 1, \dots, n_z$ .

*Proof.* Consider  $x_0$  any of the zeros  $x_0^i$ ,  $i = 1, \dots, n_z$ . A Taylor expansion of  $f$  gives

$$f(x) = 0 + D_f(x_0)(x - x_0) + \mathcal{O}(\|x - x_0\|^2)$$

so that

$$\|f(x)\|^2 = (x - x_0)^T D_f^T(x_0) D_f(x_0)(x - x_0) + \mathcal{O}(\|x - x_0\|^3)$$

Then, with  $\rho_{min} > 0$  given in the statement, there exist  $M > 0$ , such that, for all  $\|x - x_0\| \leq M$ ,

$$(A.6.1) \quad \frac{2}{3}\rho_{min} \|x - x_0\| \leq \|f(x)\|$$

Consider the closed set  $E = \{\|x\| = 1\} \setminus \bigcup_{i=1, \dots, n_z} \text{int } \mathcal{B}(x_0^i, M)$  and  $c_1 = \min_E \|f_1\| > 0$ . By construction, for  $c < c_1$ , the level set satisfies

$$\mathcal{L}_c \subset \bigcup_{i=1, \dots, n_z} \text{int } \mathcal{B}(x_0^i, M)$$

We now prove the main statement of the proposition. By contradiction, for  $0 < c < \min\{c_1, \frac{M\rho_{min}}{2}\}$ , assume there exists  $x$  in  $\mathcal{L}_c$ , such that for every zero  $x_0$  one has  $2c/\rho_{min} \leq \|x - x_0\|$  with  $\|f_1(x)\| = c$ ,  $f_2(x) = 0$ . Then, one has for every  $x_0$ ,  $\|x - x_0\| \leq M$  and so, using (A.6.1),

$$c = \|f(x)\| \geq \frac{4}{3}c$$

which concludes the proof.  $\square$

Let us choose, for any given  $q \in \mathbb{Q}$ ,  $f$  defined as

$$(A.6.2) \quad f = (f_1, f_2)$$

$$(A.6.3) \quad f_1(q') \triangleq \left( T(q) - T(q') \quad \sigma(q, q')^T \right)^T$$

$$(A.6.4) \quad f_2(q') \triangleq \|q'\| - 1$$

**Proposition 16.** *With  $f$  as defined in (A.6.4), let  $q \in \mathbb{Q}$  be such that the rank of  $D_f(\pm q)$  and  $D_f(\pm q_{\#})$  is equal to 4. Then, there exists  $\rho_{min} \neq 0$  such that, for  $c > 0$  small enough the level set  $\mathcal{L}_c \triangleq \{\bar{q} \text{ s.t. } \|f_1(q')\| = c, f_2(q') = 0\}$  is a subset of*

$$\bigcup_{q_0 \in \{\pm q, \pm q_{\#}\}} \mathcal{B}(q_0, 2c/\rho_{min})$$

*Proof.* The zeros of  $f_1$  are  $\{\pm q, \pm q_{\#}\}$ , as established in Proposition 1. The proof of Proposition 15 can be adapted knowing that the rank of  $D_f(\pm q)$  and  $D_f(\pm q_{\#})$  is equal to 4, therefore having a non zero smaller singular value ;  $\rho_{min} \neq 0$  is the smallest singular value of all the  $D_f(q_0)$  for  $q_0 \in \{\pm q, \pm q_{\#}\}$ .  $\square$

## Appendix B

# Various useful estimation methods

### B.1 Complex argument method for single-axis rotation rate estimation

The following method follows from Theorem 3.1. in [61] :

**Theorem 4.** *[Estimation of the phase of a single axis rotation from samples [61]] Consider measurements of the form*

$$y[k] = f(\psi[k]) + n[k] \in \mathbb{C}, \quad 1 \leq k \leq N$$

where

- $f$  is a  $2\pi$ -periodic function valued in  $\mathbb{C}$  parameterizing a Jordan curve  $C$
- $\psi[k] = \psi(k\Delta t)$
- $n[k]$  is a measurement noise

Assume that  $f$  is such that its Fourier expansion  $\{c_n\}_{n \in \mathbb{Z}}$  satisfies

$$|c_1| > |c_0 - z_0| + \sum_{n \neq 0,1} |c_n|$$

Assume that the interior region  $I$  defined by the boundary  $C$  is strictly convex. Assume that the noise  $n$  is uniformly bounded by  $\rho$  and that  $|\psi[k+1] - \psi[k]|$  is uniformly bounded by  $\Delta < \pi$ . Then consider

$$A_{\rho, \Delta} = I \cap \bigcap_{\psi=0}^{2\pi} \{z \in \mathbb{C}, \Re v^*(\psi)(z - f(\psi)) > \rho\}$$

where  $v(\psi) = e^{i\pi/2} \frac{f(\psi+\Delta) - f(\psi)}{|f(\psi+\Delta) - f(\psi)|}$ . If  $A_{\rho,\Delta}$  is not empty, then the following sequence

$$(B.1.1) \quad \hat{\psi}_{z_0}[k] = \sum_{j=1}^{k-1} \arg_{-\pi} \frac{y[j+1] - z_0}{y[j] - z_0}$$

where  $z_0 \in A_{\rho,\Delta}$  provides an estimate of  $\psi[k]$  with an error that is bounded by

$$|e_{z_0}|_{\infty} \leq 2 \arcsin \left| \frac{|c_0 - z_0| + \sum_{n \neq 0,1} |c_n|}{|c_1|} \right| + 2 \arcsin \frac{\rho}{\delta(z_0)}$$

where  $\delta(z_0) = \min_{\zeta} |f(\zeta) - z_0|$ . In practice, a recommendation is to select  $z_0$  as one of the following : i) the Chebyshev center of measurements, ii) the polygon centroid.

In our case, we want to estimate the « phase » of the complex transverse magnetometer measurements defined by

$$(B.1.2) \quad Z_{mag} = Y_{mag2} + iY_{mag3}$$

The derivative of said phase w.r.t. provide an estimation of the spin rate.

The complex signal  $Z_{mag}$  defines a closed curve whose center is close to the origin, defining a strictly convex interior region. Additionally,  $|Z_{mag}[k+1] - Z_{mag}[k]|$  is uniformly bounded by  $\Delta < \pi$  as long as  $|Z_{mag}| < 1$  (which is always true) and the sampling rate is larger than half the spin rate (meaning there are more than two measurements available during one rotation at the spin rate frequency).

The assumption on  $A_{\rho,\Delta}$  boils down to the fact that the noise can be uniformly bounded by  $\rho$  such that all measurements are at a strictly positive distance from some subset of the interior of the curve  $C$ . In our case, since the norm of  $Z_{mag}$  is slowly varying compared to the sampling rate,  $C$  is almost a circle. The signal-noise ratio of our magnetometers is small (less than  $10^{-2}$ ), so  $\rho$  can be chosen such that  $A_{\rho,\Delta}$  contains at least  $z_0 = 0$ . Figure B.1.1 shows approximately one spin rate period of  $Z_{mag}$  measurements from data set 2, illustrating said claims.

As a consequence, the phase estimation exposed in [61] yields satisfying results on  $Z_{mag}$ , by choosing  $z_0 = 0$ . Differentiating this estimate provide an estimation of the spin rate of the shell.

## B.2 Linear constrained estimation

This appendix details the linear constrained estimation carried out in Chapter 6 to filter the velocity obtained with frequency measurements, before





$N \rightarrow \infty$ ) estimates. In real applications, one has to deal with finite-sample bias of MUSIC.

MUSIC determines the frequency estimates from the sample covariances

$$R_k = \frac{1}{N} \sum_{i=1}^{N-k} y(t+k)y^*(t), \quad k = 0, 1, \dots, m$$

which are used to fill a symmetric Toeplitz  $m \times m$  covariance matrix  $R$ . The parameter  $m$  should be chosen (by the user) such that  $m \geq 2n$ .

In details, the implementations of MUSIC use the eigenelements of  $R$ . The eigenvalues are sorted in decreasing order, and a finite number of them are kept. From this, a function to be minimized is defined and the frequencies estimates are determined as the locations the  $n$  deepest minima of this function.

Despite being asymptotically unbiased, MUSIC can not attain the Cramér-Rao bound [93].

Under a zero-mean Gaussian assumption for the noise  $e$ , [92] establishes that, for large  $N$ , the MUSIC estimation errors are asymptotically jointly Gaussian distributed with zero means. Further, the variance-covariances are analytically given in [92], using a finite expansion of the function to be minimized, yielding an estimate of the shift of its minima. It is shown that the variances are proportional to two factors:  $d$  that is large if the frequencies are closely spaced, and a second one which is the *the inverse of the square of SNR*<sup>2</sup>. One shall also note the role of the number of data  $N$ . In summary, the variances are proportional to

$$\frac{d}{\text{SNR}^2 N}$$

For the particular cases of two frequencies, [93] shows that the variance of the estimates depend on the difference between the frequencies and not their value. The interplay between the (to be chosen) parameter  $m$  and the frequency separation for which reasonably accurate results can be obtained is known as a point worth particular care in the tuning of MUSIC.

MUSIC can be seen as a generalization of the eigenanalysis-based method (a.k.a. subspaces method) for frequency estimation, which started with Pisarenko method [77]. Conversely, the Pisarenko Harmonic Decomposition is a special case of MUSIC, dealing with a single-frequency. Originally, the Pisarenko Harmonic Decomposition was studied in [29] which contains reliable estimates for the variance of the estimator. We refer to this article which contains a tutorial presentation of the calculus yielding the variance calculation and approximations, and stresses the negative effect of finite-sample. A simple implementation can be deduced from the formulation of [87].



# Bibliography

- [1] M. Albisser. *Identification of aerodynamic coefficients from free flight data*. PhD thesis, Université de Lorraine, 2015.
- [2] A. Alessandri and P. Coletta. Switching observers for continuous-time and discrete-time linear systems. In *American Control Conference, 2001. Proceedings of the 2001*, volume 3, pages 2516–2521. IEEE, 2001.
- [3] Atlantic Inertial Systems, UTC Aerospace Systems. *SiIMU02 MEMS Inertial Measurement Unit (IMU)*, 2017.
- [4] I. Y. Bar-Itzhack. REQUEST - a new recursive algorithm for attitude determination. *Proceedings of the National Technical Meeting of The Institute of Navigation*, pages 699–706, 1996.
- [5] J. K. Bekkeng and M. Psiaki. Attitude estimation for sounding rockets using microelectromechanical system gyros. *Journal of Guidance, Control, and Dynamics*, 31(3):533–542, 2008.
- [6] L. Benziane, A. El Hadri, A. Seba, A. Benallegue, and Y. Chitour. Attitude estimation and control using linearlike complementary filters: theory and experiment. *IEEE Transactions on Control Systems Technology*, 24(6):2133–2140, 2016.
- [7] E. Bergamini, G. Ligorio, A. Summa, G. Vannozzi, A. Cappozzo, and A. M. Sabatini. Estimating orientation using magnetic and inertial sensors and different sensor fusion approaches: Accuracy assessment in manual and locomotion tasks. *Sensors*, 14(10), 2014.
- [8] A. Berkane, S. Abdessameud and A. Tayebi. Global exponential angular velocity observer for rigid body systems. In *Proc. of the 55th IEEE Conference on Decision and Control*, 2016.
- [9] S. Berkane, A. Abdessameud, and A. Tayebi. A globally exponentially stable hybrid attitude and gyro-bias observer. In *Decision and Control (CDC), 2016 IEEE 55th Conference on*, pages 308–313. IEEE, 2016.

- [10] S. Bertrand, N. Guénard, T. Hamel, H. Piet-Lahanier, and L. Eck. A hierarchical controller for miniature VTOL UAVs: Design and stability analysis using singular perturbation theory. *Control Engineering Practice*, 19(10):1099–1108, 2011.
- [11] S. Bertrand, T. Hamel, H. Piet-Lahanier, and R. Mahony. Attitude tracking of rigid bodies on the special orthogonal group with bounded partial state feedback. In *Proceedings of the 48th IEEE Conference on Decision and Control (CDC) held jointly with 2009 28th Chinese Control Conference*, pages 2972–2977. IEEE, 2009.
- [12] M. R. Brady and P. Goethals. A comparative analysis of contemporary 155 mm artillery projectiles. *Journal of Defense Analytics and Logistics*, 2019.
- [13] P. Cardou and J. Angeles. Estimating the angular velocity of a rigid body moving in the plane from tangential and centripetal acceleration measurements. *Multibody System Dynamics*, 19(4):383–406, 2008.
- [14] D. Carnevale, D. Karagiannis, and A. Astolfi. Reduced-order observer design for systems with non-monotonic nonlinearities. In *Decision and Control, 2006 45th IEEE Conference on*, pages 5269–5274. IEEE, 2006.
- [15] A. Carrière and L.-R. Oudin. Applications du calcul formel à la balistique. *Theoretical Computer Science*, 187(1):263 – 284, 1997.
- [16] A. Cavallo, A. Cirillo, P. Cirillo, G. De Maria, P. Falco, C. Natale, and S. Pirozzi. Experimental comparison of sensor fusion algorithms for attitude estimation. *IFAC Proceedings Volumes*, 47(3):7585–7591, 2014.
- [17] S. Changey. *Modélisation et estimation par filtrage non linéaire, de l’attitude d’un projectile à partir de magnétomètres*. PhD thesis, Sup-elec, 2005.
- [18] S. Changey, E. Pecheur, and T. Brunner. Attitude estimation of a projectile using magnetometers and accelerometers, experimental validation. In *Position, Location and Navigation Symposium - PLANS 2014, 2014 IEEE/ION*, pages 1168–1173, 2014.
- [19] S. Changey, E. Pecheur, and P. Wey. Real time estimation of supersonic projectile roll angle using magnetometers: In-lab experimental validation. *IFAC Proceedings Volumes*, 42(5):123–127, 2009.
- [20] S. Changey, E. Pecheur, P. Wey, and E. Sommer. Real-time estimation of projectile roll angle using magnetometers: in-lab experimental validation. *EUCASS Proceedings Series*, 6:35–44, December 2013.

- [21] D. Choukroun. *Novel methods for attitude determination using vector observations*. PhD thesis, Technion, 2003.
- [22] A. A. Chunodkar and M. R. Akella. Switching angular velocity observer for rigid-body attitude stabilization and tracking control. *Journal of Guidance, Control, and Dynamics*, 37(3):869–878, 2014.
- [23] T. Cipra and R. Romera. Kalman filter with outliers and missing observations. *Sociedad de Estadística e Investigación Operativa*, 6(2):379–395, 1997.
- [24] C. Combettes, S. Changey, R. Adam, and E. Pecheur. Attitude and velocity estimation of a projectile using low cost magnetometers and accelerometers. In *2018 IEEE/ION Position, Location and Navigation Symposium (PLANS)*, pages 650–657. IEEE, 2018.
- [25] M. Costello and T. Jitpraphai. Determining angular velocity and angular acceleration of projectiles using triaxial acceleration measurements. *Journal of spacecraft and rockets*, 39(1):73–80, 2002.
- [26] J. L. Crassidis, F. L. Markley, and Y. Cheng. Survey of nonlinear attitude estimation methods. *Journal of Guidance, Control and Dynamics*, 2007.
- [27] J. L. Crassidis, F. L. Markley, and Y. Cheng. Survey of nonlinear attitude estimation methods. *Journal of Guidance, Control, and Dynamics*, 30(1):12–28, 2007.
- [28] A. D. Dupuis and W. Hathaway. Aeroballistic range tests of the basic finner reference projectile at supersonic velocities. Technical report, Defence Research Establishment Valcartier (Québec), 1997.
- [29] A. Eriksson and P. Stoica. On statistical analysis of Pisarenko tone frequency estimator. *Signal Processing*, 31(3):349–353, 1993.
- [30] L. D. Fairfax and F. E. Fresconi. Position estimation for projectiles using low-cost sensors and flight dynamics. *Journal of Aerospace Engineering*, 27(3):611–620, 2012.
- [31] P. Faure. *Navigation inertielle et filtrage stochastique*. Méthodes mathématiques de l’informatique. Dunod, 1971.
- [32] K. Feng, J. Li, X. Zhang, C. Shen, Y. Bi, T. Zheng, and J. Liu. A new quaternion-based kalman filter for real-time attitude estimation using the two-step geometrically-intuitive correction algorithm. *Sensors*, 17(9):2146, 2017.

- [33] C. Fernandez-Granda and E. J. Candès. Towards a mathematical theory of super-resolution. *Communications on Pure and Applied Mathematics*, 67(6):906–956, 2014.
- [34] C. Fernandez-Granda, G. Tang, X. Wang, and L. Zheng. Demixing sines and spikes : Robust spectral super-resolution in the presence of outliers. *Information and Inference*, sep 2017.
- [35] A. Filippeschi, N. Schmitz, M. Miezal, G. Bleser, E. Ruffaldi, and D. Stricker. Survey of motion tracking methods based on inertial sensors: a focus on upper limb human motion. *Sensors*, 17(6):1257, 2017.
- [36] A. Fiot, S. Changey, C. Combettes, and N. Petit. Estimation of air velocity for a high velocity spinning projectile using transverse accelerometers. In *Proc. of the AIAA Guidance, Navigation, and Control Conference, AIAA Science and Technology Forum and Exposition*, 2018.
- [37] A. Fiot, S. Changey, C. Combettes, and N. Petit. A velocity observer for exterior ballistics using an embedded frequency detection of pitch and yaw aerodynamics. In *CDC18*, 2018.
- [38] A. Fiot, S. Changey, C. Combettes, and N. Petit. A gyroless adaptation of attitude complementary filtering. In *Proc. of the European Control Conference (ECC)*, 2019.
- [39] V. Fleck. Introduction à la balistique extérieure avec exercices. *Cours de balistique extérieure, Coëtquidan*, 2005.
- [40] H. Fourati and D. E. C. Belkhiat. *Multisensor Attitude Estimation: Fundamental Concepts and Applications*. CRC Press, 2016.
- [41] E. Fousson and C. Berner. Guidance of medium-caliber ammunition using a single pyrotechnic impulse thruster. *Journal of Spacecraft and Rockets*, 54(1):299–305, 2017.
- [42] R. H. Fowler, E. G. Gallop, C. N. H. Lock, and H. W. Richmond. The aerodynamics of a spinning shell. *Proceedings of the Royal Society of London. Series A, Containing Papers of a Mathematical and Physical Character*, 98(690):199–205, 1920.
- [43] T. Hamel and R. Mahony. Attitude estimation on SO[3] based on direct inertial measurements. In *Proceedings 2006 IEEE International Conference on Robotics and Automation, 2006. ICRA 2006.*, pages 2170–2175, May 2006.
- [44] M. H. Hayes. *Statistical Digital Signal Processing and Modeling*. John Wiley & Sons, 1996.

- [45] P. Horowitz and W. Hill. *The art of electronics*. Cambridge Univ. Press, 1989.
- [46] M.-D. Hua. Attitude estimation for accelerated vehicles using gps/ins measurements. *Control Engineering Practice*, 18(7):723–732, 2010.
- [47] M.-D. Hua, G. Ducard, T. Hamel, R. Mahony, and K. Rudin. Implementation of a nonlinear attitude estimator for aerial robotic vehicles. *IEEE Transactions on Control Systems Technology*, 22(1):201–213, 2014.
- [48] M.-D. Hua, T. Hamel, P. Morin, and C. Samson. A control approach for thrust-propelled underactuated vehicles and its application to vtol drones. *IEEE Transactions on Automatic Control*, 54(8):1837–1853, 2009.
- [49] M.-D. Hua, T. Hamel, P. Morin, and C. Samson. Introduction to feedback control of underactuated VTOL vehicles: A review of basic control design ideas and principles. *IEEE Control systems magazine*, 33(1):61–75, 2013.
- [50] A. H. Jazwinski. *Stochastic processes and filtering theory*. New York: Academic Press, 1970.
- [51] D. Jung and P. Tsiotras. Inertial attitude and position reference system development for a small UAV. In *AIAA Infotech at Aerospace*, 2007.
- [52] J. L. Kelley and E. J. McShane. On the motion of a projectile with small or slowly changing yaw. *Ballistics Research Laboratories Rep. No. 446, Dec. 1944*, 1944.
- [53] R. H. Kent. Notes on a theory of spinning shell. Technical report, Ballistics Research Laboratories Rep. No. 898. 1954, 1954.
- [54] K. Kitani, K. Horita, and H. Koike. Ballcam! dynamic view synthesis from spinning cameras. In *Adjunct proceedings of the 25th annual ACM symposium on User interface software and technology*, pages 87–88. ACM, 2012.
- [55] F. Königseder, W. Kemmetmüller, and A. Kugi. Attitude estimation using redundant inertial measurement units for the control of a camera stabilization platform. *IEEE Transactions on Control Systems Technology*, 24(5):1837–1844, 2016.
- [56] R. Kottath, P. Narkhede, V. Kumar, V. Karar, and S. Poddar. Multiple model adaptive complementary filter for attitude estimation. *Aerospace Science and Technology*, 69:574–581, 2017.

- [57] N. N. Krasovskii. *Problems of the theory of Stability of Motion*. MIR, translated by Stanford University Press, 1963.
- [58] L. Landau and E. Lifchitz. *Mechanics*. MIR Moscou, fourth edition, 1982.
- [59] H. Lee, Y-H.. Choi, H.-C. Bang, and J.-O. Park. Kalman filtering for spacecraft attitude estimation by low-cost sensors. *KSAS International Journal*, 9(1):147–161, 2008.
- [60] R. D. Lorenz. *Spinning Flight*. Springer, 2006.
- [61] L. Magnis. *Estimation of angular rate from direction sensors*. PhD thesis, MINES ParisTech, 2016.
- [62] L. Magnis and N. Petit. Rotation estimation for a satellite from sun sensors. In *Control Conference (ECC), 2013 European*, pages 852–859. IEEE, 2013.
- [63] L. Magnis and N. Petit. Angular velocity nonlinear observer from single vector measurements. *Automatic Control, IEEE Transactions on*, 61(9):2473–2483, 2016.
- [64] L. Magnis and N. Petit. Angular velocity and torque observer from vector measurements. *Proceedings of the 20th World Congress of IFAC*, pages 9330–9337, 2017.
- [65] L. Magnis and N. Petit. Angular velocity nonlinear observer from vector measurements. *Automatica*, 75:46–53, 2017.
- [66] R. Mahony, T. Hamel, P. Morin, and E. Malis. Nonlinear complementary filters on the special linear group. *International Journal of Control*, 85(10):1557–1573, 2012.
- [67] R. Mahony, T. Hamel, and J.-M. Pfimlin. Complementary filter design on the special orthogonal group  $SO(3)$ . In *44th IEEE Conference on Decision and Control, and the European Control Conference 2005*, 2005.
- [68] R. Mahony, T. Hamel, and J.-M. Pfimlin. Nonlinear complementary filters on the special orthogonal group. *IEEE Transactions on Automatic Control*, 53(5):1203–1218, June 2008.
- [69] S. Mallat. *A wavelet tour of signal processing: the sparse way*. Academic Press, 2008.
- [70] P. Martin and I. Sarras. A global observer for attitude and gyro biases from vector measurements. *IFAC-PapersOnLine*, 50(1):15409–15415, 2017.

- [71] C. G. Mayhew, R. G. Sanfelice, and A. R. Teel. Quaternion-based hybrid control for robust global attitude tracking. *IEEE Transactions on Automatic Control*, 56(11):2555–2566, 2011.
- [72] R. L. McCoy. *Modern exterior ballistics*. Schiffer, 2nd edition, 1998.
- [73] N. Metni, J.-M. Pflimlin, T. Hamel, and Ph. Souères. Attitude and gyro bias estimation for a VTOL UAV. *Control Engineering Practice*, 14(12):1511 – 1520, 2006.
- [74] T. Michel, P. Genevès, H. Fourati, and N. Layaïda. On attitude estimation with smartphones. In *Pervasive Computing and Communications (PerCom), 2017 IEEE International Conference on*, pages 267–275. IEEE, 2017.
- [75] P. Morin, C. Samson, J.-B. Pomet, and Z.-P. Jiang. Time-varying feedback stabilization of the attitude of a rigid spacecraft with two controls. In *Proceedings of 1994 33rd IEEE Conference on Decision and Control*, volume 1, pages 914–915. IEEE, 1994.
- [76] C. H. Murphy. Free flight motion of symmetric missiles. Technical report, Army Ballistic Research Lab Aberdeen Proving Ground MD, 1963.
- [77] V. F. Pisarenko. The retrieval of harmonics from a covariance function. *Geophysical Journal International*, 33(3):347–366, 1973.
- [78] S. Podjawerschek, E. Spahn, J. Horn, M. Brodmann, and R. Himmelsbach. Distance and velocity estimation of projectiles based on doppler radar signals using a nonlinear discrete-time observer. In *Signal and Data Processing of Small Targets 2010*, volume 7698. International Society for Optics and Photonics, 2010.
- [79] C. V. Rao, J. B. Rawlings, and J. H. Lee. Constrained linear state estimation using a moving horizon approach. *Automatica*, 37(10):1619–1628, 2001.
- [80] T. Recchia, W. Toledo, J. Cahayla, and E. Scheper. Onboard sensor suite for determining projectile velocity, April 30 2013. US Patent 8,433,460.
- [81] J. Rogers, M. Costello, T. Harkins, and M. Hamaoui. Effective use of magnetometer feedback for smart projectile applications. *Navigation*, 58(3):203–219, 2011.
- [82] W.J. Rugh. *Linear System Theory*. Prentice-Hall, second edition, 1996.

- [83] J. Shang, Z. Deng, M. Fu, and S. Wang. A high-spin rate measurement method for projectiles using a magnetoresistive sensor based on time-frequency domain analysis. *Sensors*, 16(6):894, 2016.
- [84] M. D. Shuster. Approximate algorithms for fast optimal attitude computation. *Proceedings of the AIAA Guidance and Control Conference*, pages 88–95, 1978.
- [85] M. D. Shuster. Kalman filtering of spacecraft attitude and the QUEST model. *The Journal of the Astronautical Sciences*, 38(3):377–393, 1990.
- [86] I. Skog and P. Handel. In-car positioning and navigation technologies – a survey. *IEEE Transactions on Intelligent Transportation Systems*, 10(1):4–21, 2009.
- [87] H.-C. So and K. W. Chan. Reformulation of Pisarenko harmonic decomposition method for single-tone frequency estimation. *IEEE Transactions on signal processing*, 52(4):1128–1135, 2004.
- [88] J. C. Springmann and J. W. Cutler. Flight results of a low-cost attitude determination system. *Acta Astronautica*, 99:201–214, 2014.
- [89] J. C. Springmann and J. W. Cutler. Optimization of directional sensor orientation with application to photodiodes for spacecraft attitude determination. *Journal of Guidance, Control, and Dynamics*, 37:828–837, 2014.
- [90] J. C. Springmann, A. J. Sloboda, A. T. Klesh, M. W. Bennett, and J. W. Cutler. The attitude determination system of the rax satellite. *Acta Astronautica*, 75:120–135, 2012.
- [91] P. Stoica, P. Händel, and T. Söderström. Approximate maximum likelihood frequency estimation. *Automatica*, 30(1):131–145, 1994.
- [92] P. Stoica and A. Nehorai. MUSIC, maximum likelihood, and Cramer-Rao bound. *IEEE Transactions on Acoustics, speech, and signal processing*, 37(5):720–741, 1989.
- [93] P. Stoica and T. Söderström. Statistical analysis of MUSIC and subspace rotation estimates of sinusoidal frequencies. *IEEE Transactions on Signal Processing*, 39(8):1836–1847, 1991.
- [94] B. O. Sunde. Sensor modelling and attitude determination for micro-satellites. Master’s thesis, NTNU, 2005.
- [95] A. Tayebi, S. McGilvray, A. Roberts, and M. Moallem. Attitude estimation and stabilization of a rigid body using low-cost sensors. In

- Decision and Control, 2007 46th IEEE Conference on*, pages 6424–6429. IEEE, 2007.
- [96] A. Tayebi, A. Roberts, and A. Benallegue. Inertial vector measurements based velocity-free attitude stabilization. *IEEE Transactions on Automatic Control*, 58(11):2893–2898, 2013.
  - [97] D. Thakur, F. Mazenc, and M. R. Akella. Partial Lyapunov strictification: smooth angular velocity observers for attitude tracking control. In *AIAA/AAS Astrodynamics Specialist Conference*, page 4420, 2014.
  - [98] D. H. Titterton and J. L. Weston. *Strapdown Inertial Navigation Technology*. The American Institute of Aeronautics and Astronautics, Reston, USA, 2 edition, 2004.
  - [99] R. G. Valenti, I. Dryanovski, and J. Xiao. Keeping a good attitude: A quaternion-based orientation filter for IMUs and MARGs. *Sensors*, 15(8):19302–19330, 2015.
  - [100] R. Vitek. Influence of camera calibration technique on projectile velocity estimation. In *Military Technologies (ICMT), 2017 International Conference on*, pages 78–86. IEEE, 2017.
  - [101] G. Wahba. Problem 65-1: a least squares estimate of spacecraft attitude. *SIAM Review*, 7(3):409, 1965.
  - [102] S. Weiss, K.-F. Doherr, and H. Schilling. Analytical solution and parameter estimation of projectile dynamics. *Journal of spacecraft and rockets*, 32(1):67–74, 1995.
  - [103] J. Yu, X. Bu, C. Xiang, and B. Yang. Spinning projectile’s attitude measurement using intersection ratio of magnetic sensors. *Proceedings of the Institution of Mechanical Engineers, Part G: Journal of Aerospace Engineering*, 2016.
  - [104] P. Zarchan. *Tactical and Strategic Missile Guidance*. The American Institute of Aeronautics and Astronautics, 2007.
  - [105] Z. Zhao, G. Wen, X. Zhang, and D. Li. Model-based estimation for pose, velocity of projectile from stereo linear array image. *Measurement Science Review*, 12(3):104–110, 2012.





## RÉSUMÉ

---

Cette thèse présente une méthode pour estimer l'attitude d'un projectile en vol à partir de mesures de directions. L'estimation d'attitude est une étape essentielle pour le développement de « munitions intelligentes », rendant possible le changement de cible en vol et l'optimisation de la portée. La méthode que nous proposons repose exclusivement sur un accéléromètre et un magnétomètre embarqués. En particulier, elle ne requiert pas de gyroscope, capteur coûteux et trop fragile pour survivre aux conditions de tir, quand il n'est pas soumis à des restrictions d'importation. Pour la détermination de l'attitude du projectile, nous contournons l'incapacité des accéléromètres à donner une mesure de direction de la gravité en vol ballistique, en les utilisant pour estimer la vitesse du projectile par rapport à l'air. Ceci est réalisé grâce à une méthode de détection de fréquence appliquée aux oscillations de précession et de nutation du projectile induites par les moments aérodynamiques qu'il subit. Par la suite, les variations de la vitesse du projectile nous donnent une information d'orientation partielle qui complète la direction donnée par le magnétomètre 3-axes. Les deux informations sont traitées par un observateur d'attitude adapté du filtre complémentaire ; cette adaptation n'est pas triviale et on réalise une étude détaillée de la convergence de l'observateur proposé. L'efficacité de la méthode est illustrée par des résultats sur des données de simulation et des données de vol réel.

## MOTS CLÉS

---

Observateurs non linéaires, estimation d'attitude, ballistique extérieure, traitement du signal

## ABSTRACT

---

The thesis addresses the estimation of the attitude of an artillery shell in free flight, during the flight phase called exterior ballistics. Attitude estimation is an essential step for the development of « smart-shells » a.k.a. « guided-ammunition » which are capable of achieving various guidance tasks such as in-flight re-targeting and optimization of range. The method developed here uses strapdown accelerometers and magnetometers only. In particular, it does not use any rate gyro, a pricey component that is too fragile to survive the stress of gunshot when it is not subjected to import restrictions. For attitude determination, we circumvent the intrinsic inability of accelerometers to provide direction information in free flight, by employing them not to measure the direction of gravity but to estimate the velocity w.r.t. the air. This is achieved through a frequency detection method applied to the pitching and yawing rotational dynamics generated by aerodynamics moments. In turn, the variation of the velocity gives us an orientation information that complements the direction given by the 3-axis Magnetometer. The two information are treated by an attitude observer adapted from the well-known complementary filter. This adaptation requires special care and an analysis of the convergence of the resulting observer is provided. The applicability of the method is shown on simulations and real-flight experiments.

## KEYWORDS

---

Nonlinear observers, attitude estimation, exteriors ballistics, signal processing